Easy-to-implement *hp*-adaptivity for non-elliptic goal-oriented problems

Felipe Vinicio Caro Gutiérrez

Supervised by *David Pardo* and *Elisabete Alberdi*

December 2023

eman ta zabal zazu

Universidad del País Vasco

Euskal Herriko Unibertsitatea

Easy-to-implement *hp*-adaptivity for non-elliptic goal-oriented problems

Felipe Vinicio Caro Gutiérrez

Supervised by *David Pardo* and *Elisabete Alberdi*

December 2023

This dissertation has been possible with the support of the University of the Basque Country (UPV/EHU) grant No. PRE2018-084258; the BCAM "Severo Ochoa" accreditation of excellence (SEV-2017-0718); the Basque Government through the BERC 2018-2021 program; and the Consolidated Research Group MATHMODE (IT1294-19; IT1456-22) given by the Department of Education.

Acknowledgements

I am grateful for the past four years, my life's most remarkable and transformative period. Following two challenging years pursuing a master's degree in physics applied to the ocean, fate guided me back to the enchanting realm of mathematics.

First, I want to express my sincere gratitude to my supervisor, David Pardo, for graciously accepting me as his student. Joining David's group has been incredible, and I am profoundly grateful for the opportunity. With his guidance and support, I am writing my PhD Dissertation. I aspire to emulate David's many professional and personal qualities. He exemplifies the ideal supervisor, and I am privileged to have him as my mentor.

I want to express my deep gratitude to Elisabete Alberdi, my co-supervisor, for her endless patience and persistent support throughout my journey. Our enlightening discussions in her office, where she introduced me to the intriguing realm of Finite Element Methods, will forever be embedded in my memory. I appreciate her tenacious confidence in my capabilities and unwavering trust in my work.

I want to express my deepest gratitude to Vincent Darrigrand for his invaluable contributions throughout these years and during my stay in Toulouse. His unwavering support in assisting me with code-related challenges has been truly remarkable. Vincent's guidance and endless advice on "doing things in the right way" have been instrumental in shaping my personal and professional growth. He has provided technical expertise and imparted invaluable knowledge on discerning the distinctions between the correct and incorrect approaches. Thanks to his guidance, I have developed my own set of principles and criteria in my personal and professional initiatives.

I want to express my genuine gratitude to Julen Alvarez-Aramberri for his invaluable contributions to enriching my research activities. Julen has shared his profound professional skills throughout our three years as colleagues, impacting my academic journey indelibly. More importantly, he has imparted one of the most vital life lessons: the importance of being honest with oneself. Julen's guidance has not only shaped me into a better scientist but also a better individual. I am genuinely grateful for his support and mentorship.

I want to express my fervent appreciation to my wonderful colleagues at BCAM, including Jon Ander, Oscar, Carlos, and Ana. I am also grateful for the professional connections I have developed with them. In particular, I owe a debt of

gratitude to Judit, with whom I shared my first scientific congress. That experience was truly unforgettable, and I will always treasure the memories. I look forward to meeting any of them, whether at BCAM or elsewhere, as it will always be a joyful occasion.

I want to thank Prof. Maciej Paszyński for his warm and invaluable support in welcoming me to the Institute of Computer Science at AGH University in Krakow. My time in Krakow was genuinely enriching, and the professional experiences I gained were immeasurable. I am deeply grateful for the guidance and mentorship provided by Prof. Paszyński during my stay. Additionally, I would like to express my sincere appreciation to Albert Oliver-Serra, Michał Jungiewicz, Maciej Woźniak, Eirik Valseth, and Maciej Smołka. Our shared professional experiences at AGH were precious, and I am grateful for the collaboration and insights we exchanged. Their contributions have undoubtedly played a significant role in shaping my academic and professional development.

I sincerely tribute Dariel Hernández, who transcends the definition of a mere colleague at BCAM. Dariel's tenacious dedication to his craft and infectious passion for dancing has enriched our professional relationship and fostered a genuine friendship. Words alone are insufficient to express the depth of my gratitude towards him. I am profoundly thankful for his constant support, camaraderie, and the joy he brings to our shared experiences. I am honored to call you both a colleague and a dear friend.

Lastly, I would like to express my sincere appreciation to Cambré Dancing School and all those associated with it. You have given me unforgettable moments, travels, and shared dancing congresses that I will cherish forever. I want to give a special mention to Sergio and Andrea, whose guidance and support were instrumental in helping me discover my passion for dance. They provided me with the knowledge and encouragement to push beyond my limits and embrace the joy of dancing. Dancing has become an integral part of my life, thanks to the countless hours we spent honing our skills and creating unforgettable memories. I am forever grateful to Sergio, Andrea, and everyone at Cambré for enriching my life through the art of dance.

Abstract

The Finite Element Method (FEM) has become a foundational numerical technique in computational mechanics and civil engineering since its inception by Courant in 1943 [56]. Originating from the Ritz method and variational calculus, the FEM was primarily employed to derive solutions for vibrational systems. A distinctive strength of the FEM is its capability to represent mathematical models through the weak variational formulation of Partial Differential Equations (PDEs), facilitating computational feasibility even in intricate geometries. However, the search for accuracy often imposes a significant computational task.

In the FEM, adaptive methods have emerged to balance the accuracy of solutions with computational costs. The h-adaptive FEM designs more efficient meshes by reducing the mesh size h locally while keeping the polynomial order of approximation p fixed (usually $p = 1, 2$). An alternative approach to the h-adaptive FEM is the p-adaptive FEM, which locally enriches the polynomial space p while keeping the mesh size h constant. By dynamically adapting h and p, the hp-adaptive FEM achieves exponential convergence rates.

Adaptivity is crucial for obtaining accurate solutions. However, the traditional focus on global norms, such as L^2 or H^1, might only sometimes serve the requirements of specific applications. In engineering, controlling errors in specific domains related to a particular Quantity of Interest (QoI) is often more critical than focusing on the overall solution. That motivated the development of Goal-Oriented Adaptive (GOA) strategies.

In this dissertation, we develop automatic Goal-Oriented (GO) hp-adaptive algorithms tailored for non-elliptic problems. These algorithms shine in terms of robustness and simplicity in their implementation, attributes that make them especially suitable for industrial applications. A key advantage of our methodologies is that they do not require computing reference solutions on globally refined grids. Nevertheless, our approach is limited to anisotropic p and isotropic h refinements.

We conduct multiple tests to validate our algorithms. We probe the convergence behavior of our GO h- and p-adaptive algorithms using Helmholtz and convection-diffusion equations in one-dimensional scenarios. We test our GO hp-adaptive algorithms on Poisson, Helmholtz, and convection-diffusion equations in two dimensions. We use a Helmholtz-like scenario for three-dimensional cases to highlight the adaptability of our GO algorithms.

Abstract

We also create efficient ways to build large databases ideal for training Deep Neural Networks (DNNs) using *hp* Multi-Adaptive Goal-Oriented (MAGO) FEM. As a result, we efficiently generate large databases, possibly containing hundreds of thousands of synthetic datasets or measurements.

Resumen

El método de elementos finitos (MEF) aproxima soluciones a ecuaciones diferenciales parciales (EDPs). Basándose en el método de Ritz y el cálculo variacional, Courant desarrolló el MEF en 1943 [56]. Desde entonces se ha convertido en una técnica fundamental en la mecánica computacional y la ingeniería civil que se ha utilizado para resolver una amplia gama de problemas, incluyendo análisis estructural, mecánica de fluidos y sistemas vibratorios.

Una fortaleza distintiva del MEF es su capacidad para representar modelos matemáticos a través de la formulación variacional débil de las EDPs, facilitando la viabilidad computacional incluso en geometrías intrincadas. Sin embargo, la búsqueda de precisión a menudo impone una tarea computacional significativa.

Debido a los altos costos computacionales de ciertos problemas, han surgido métodos adaptativos para equilibrar la precisión de las soluciones con los costos computacionales. El MEF adaptativo es un método numérico que permite aproximar soluciones de forma más precisa con menor costo computacional. El MEF adaptativo h diseña mallas más eficientes reduciendo el tamaño de malla localmente mientras mantiene el orden del polinomio de aproximación p fijo (generalmente $p = 1, 2$). Una alternativa al MEF adaptativo h es el MEF adaptativo p, que enriquece localmente el espacio de polinomios p manteniendo constante el tamaño de malla h. Al combinar dinámicamente ambos métodos, el MEF adaptativo hp logra tasas de convergencia exponenciales.

El enfoque tradicional de la adaptatividad en normas globales (L^2 o H^1) sólo sirve para ciertas aplicaciones. En ingeniería, controlar errores en dominios específicos relacionados con una cantidad de interés es a menudo más crítico que controlar errores globales. Debido a esta necesidad, surge la adaptatividad orientada a un objetivo específico.

En este trabajo, desarrollamos algoritmos automáticos orientados a un objetivo hp diseñados para problemas no elípticos. Estos algoritmos se destacan en términos de robustez y simplicidad en su implementación, atributos que los hacen especialmente adecuados para aplicaciones industriales. Una ventaja clave de nuestras metodologías es que no requieren calcular soluciones de referencia en mallas globalmente refinadas. Sin embargo, nuestro enfoque se limita a refinamientos anisotrópicos p e isotrópicos h.

Los resultados numéricos 1D muestran la convergencia de nuestros algoritmos orientados a un objetivo, tanto h como p, usando las ecuaciones de Helmholtz y

convección-difusión. Además, los resultados numéricos en 2D muestran la convergencia de los algoritmos *hp* usando las ecuaciones de Poisson, Helmholtz y convección-difusión. También, probamos estos algoritmos *hp* en casos 3D con la ecuación de Helmholtz para demostrar la versatilidad de nuestros algoritmos.

Finalmente, extendemos nuestros algoritmos orientados a un objetivo *hp* para generar grandes bases de datos confiables e ideales para entrenar redes neuronales. Como resultado, mostramos la generación eficiente de grandes bases de datos potencialmente con cientos de miles de datos sintéticos.

Contents

Acknowledgements ii

Abstract iv

Resumen vi

Contents viii

Acronyms xi

List of Figures xii

List of Tables xv

1. Introduction 1
- 1.1. Motivation . . . 1
- 1.2. Literature review . . . 2
  - 1.2.1. Advances in *hp*-adaptivity . . . 2
  - 1.2.2. Advances in Goal-Oriented adaptivity . . . 5
- 1.3. Main contributions of the dissertation . . . 7
- 1.4. Outline . . . 8

I. Goal-Oriented *hp*-adaptivity for non-parametric PDEs 10

2. Multi-level *hp*-meshes 11
- 2.1. Data structures . . . 11
  - 2.1.1. Removable basis functions in a multi-level *hp*-mesh . . . 12

3. Goal-Oriented coarsening strategy 13
- 3.1. Unrefinement policy . . . 13
- 3.2. Projectors . . . 15
- 3.3. Error indicators . . . 16
  - 3.3.1. Energy-norm based elliptic problems . . . 17

3.3.2. Extension to energy-based non-elliptic problems 17
3.3.3. Extension to Goal-Oriented adaptivity 18
3.3.4. Error indicators using a pseudo-dual operator 20

4. 1D Numerical results for Goal-Oriented h- and p-adaptivity 22
4.1. Helmholtz Goal-Oriented problem 23
4.2. Convection-diffusion Goal-Oriented problem 26

5. 2D Numerical results for hp-adaptivity 29
5.1. Singular Poisson example 30
5.2. Wave propagation problem 33
5.2.1. Energy-norm adaptivity 33
5.2.2. Goal-Oriented adaptivity 37
5.3. Convection-dominated diffusion problem 39
5.3.1. Convection-dominated diffusion: example 1 39
5.3.1.1. Energy-norm adaptivity 39
5.3.2. Convection-dominated diffusion: example 2 40
5.3.2.1. Energy-norm adaptivity 43
5.3.2.2. Goal-Oriented adaptivity 45

6. 3D Numerical results for hp-adaptivity 50
6.1. Wave propagation problem 50
6.1.1. Energy-norm adaptivity 51
6.1.2. Goal-Oriented adaptivity 51

II. Goal-Oriented hp-adaptivity for parametric PDEs. 56

7. Database generation for DL inversion 57
7.1. A Goal-Oriented strategy for parametric PDEs 59
7.1.1. Variational abstract formulations 59
7.1.2. Element-wise indicators 60
7.1.3. A Multi-Adaptive Goal-Oriented strategy 61
7.2. Generation of databases 64
7.2.1. Computational costs of MAGO 64
7.2.2. Precomputations of the global matrices 67
7.3. Numerical results 70
7.3.1. Definitions 70
7.3.1.1. Convergence of the MAGO adaptivity 70
7.3.1.2. Computational costs of generating the database . 71
7.3.1.3. Generating model parameter samples 71

7.3.2. Wave propagation example 72
7.3.2.1. Example: wave propagation problem 72
7.3.2.2. Wave propagation: convergence 73
7.3.2.3. Wave propagation: accuracy 79
7.3.2.4. Wave propagation: computational costs 79
7.3.3. Poisson example 81
7.3.3.1. Example: cross-shaped domain Poisson problem . 81
7.3.3.2. Cross-shaped domain Poisson: convergence 83
7.3.3.3. Cross-shaped domain Poisson: accuracy 89
7.3.3.4. Cross-shaped domain Poisson: computational costs 89
7.3.3.5. Example: grid-based domain Poisson problem . . 90
7.3.3.6. Grid-based domain Poisson: convergence 90
7.3.3.7. Grid-based domain Poisson: accuracy 97
7.3.3.8. Grid-based domain Poisson: computational costs 97

III. Main achievements, conclusions and future work 99

8. Main Achievements 100
8.1. Peer-reviewed Publications 100
8.2. International Conferences 100
8.3. Seminars 101
8.4. Research Stays 102
8.5. Implemented software 102

9. Conclusions and Future Work 103
9.1. Conclusions 103
9.2. Future Work 104

Bibliography 105

Acronyms

FEM Finite Element Method

PDE Partial Differential Equation

PBI Projection-Based Interpolation

DG Discontinuous Galerkin

GOA Goal-Oriented Adaptive

GO Goal-Oriented

QoI Quantity of Interest

QoIs Quantities of Interest

DoF Degrees of Freedom

nDoF number of Degrees of Freedom

MAGO Multi-Adaptive Goal-Oriented

SAGO Single-Adaptive Goal-Oriented

DL Deep Learning

ML Machine Learning

NN Neural Network

DNN Deep Neural Network

IP Inverse Problem

IGA Isogeometric Analysis

FLOP Floating Point Operation

List of Figures

2.1. Illustration of a 1D multi-level *hp*-grid with hierarchical basis functions and Dirichlet nodes. *Removable* basis functions are indicated in red. 12

3.1. Adaptive process illustrated over a square domain with a hole in the middle (marked in gray). 14

4.1. Evolution of $e_{\text{rel}}^{\text{QoI}}$ using h-adaptivity. Initial mesh size $h = \frac{1}{30}$ and uniform $p = 1$. 24
4.2. Evolution of $e_{\text{rel}}^{\text{QoI}}$ using p-adaptivity. Uniform mesh size $h = \frac{1}{30}$. . 24
4.3. Solutions with $k = 7 \cdot 2\pi$ problem after the h-adaptive process. . . 25
4.4. Evolution of $e_{\text{rel}}^{\text{QoI}}$ using h-adaptivity. Initial mesh size $h = \frac{1}{30}$ and uniform $p = 1$. 26
4.5. Evolution of $e_{\text{rel}}^{\text{QoI}}$ using p-adaptivity. Uniform mesh size $h = \frac{1}{30}$. . 27
4.6. Solutions with $\varepsilon = 10^{-3}$ problem after the h-adaptive process. . . 27

5.1. Our singular Poisson example is defined over the domain Ω. The Dirichlet boundary is denoted by Γ_D. The source function is supported on Ω_f, and the QoI $l(\phi)$ is supported on Ω_l. 31
5.2. Direct and adjoint solutions of our singular Poisson example. . . . 31
5.3. Final h- and hp-adapted meshes for our singular Poisson example. 32
5.4. Our wave propagation example is defined over the domain Ω with a hole in the middle (marked in gray). The Dirichlet boundary is denoted by Γ_D, while the Neumann boundary condition is denoted by Γ_N. The source function is supported on Ω_f, and the QoI $l(\phi)$ is supported on Ω_l. 33
5.5. Absolute value of the direct and adjoint solutions of our wave propagation example in a lossy medium. 34
5.6. Final h- and hp-adapted meshes for our wave propagation example in a lossy medium. 35
5.7. Energy-norm adaptivity. Evolution of $\tilde{e}_{\text{rel}}^{\text{energy}}$ and $e_{\text{rel}}^{\text{QoI}}$ in our wave propagation example in a lossy medium. 36
5.8. Convergence history of $e_{\text{rel}}^{\text{QoI}}$ and $\tilde{e}_{\text{rel}}^{\text{energy}}$ for the energy-norm and GO hp-adaptive strategies. 36

5.9. Final h- and hp-adapted meshes for our singular GO wave propagation example in a lossy medium and the evolution of $e_{\text{rel}}^{\text{QoI}}$. . . . 38
5.10. Solution of the convection-dominated diffusion example 1. 40
5.11. Final h- and hp-adapted meshes for our first convection-dominated diffusion example and the evolution of $e_{\text{rel}}^{\text{energy}}$. 41
5.12. Problem description for our second convection-dominated diffusion with advection skew to the mesh. 42
5.13. Numerical solution of the convection-dominated diffusion example 2 for energy-norm adaptivity. 43
5.14. Final h- and hp-adapted meshes for our second convection-dominated diffusion example and the evolution of $\tilde{e}_{\text{rel}}^{\text{energy}}$. 44
5.15. Numerical solutions and hp-adapted meshes (polynomial orders in the x-direction) at iterations 7 and 10. 46
5.16. Numerical solutions and hp-adapted meshes (polynomial orders in the x-direction) at iterations 17 and 21. 47
5.17. Direct and adjoint numerical solutions of the convection-dominated diffusion problem for GO adaptivity. 48
5.18. Final h- and hp-adapted meshes for our second convection-dominated diffusion example and the evolution of $e_{\text{rel}}^{\text{QoI}}$. 49

6.1. Diffusive coefficient values for the different materials in the domain. 51
6.2. Absolute value of the direct and adjoint solutions of our 3D wave propagation example in a lossy medium. 52
6.3. Energy-norm adaptivity. Final hp-adapted meshes for our 3D wave propagation example in a lossy medium. 53
6.4. Convergence history of $e_{\text{rel}}^{\text{QoI}}$ and $\tilde{e}_{\text{rel}}^{\text{energy}}$ for the energy-norm and GO hp-adaptive strategies. 54
6.5. GO adaptivity. Final hp-adapted meshes for our 3D wave propagation example in a lossy medium. 55

7.1. Representation of S different samples. 59
7.2. Our grid-based domain example is defined over the domain Ω. The Dirichlet boundary condition is denoted by $\partial\Omega$. The source function is supported on Ω_f, and the QoI $l(\phi)$ is supported on Ω_l. . . 72
7.3. Absolute value of the solutions of our wave propagation example. 73
7.4. hp-adapted meshes for our 1-sample wave propagation. 74
7.5. hp-adapted meshes for our 5-sample wave propagation. 75
7.6. hp-adapted meshes for our 10-sample wave propagation. 76
7.7. hp-adapted meshes for our 100-sample wave propagation. 77
7.8. hp-adapted meshes for our 1000-sample wave propagation. 78

7.9. Box plots for **different adaptive grids** with a threshold maximum relative error set at 10^{-5}. 79
7.10. Computational domain Ω, where homogeneous Dirichlet boundary conditions are imposed on $\partial\Omega$. Additionally, we define Ω_l as the support of the QoI $l(\phi)$, and Ω_f as the support of the source function. 81
7.11. Absolute value of the solutions of our cross-shaped domain Poisson example. 82
7.12. *hp*-adapted meshes for our 1-sample cross-shaped domain example. 84
7.13. *hp*-adapted meshes for our 5-sample cross-shaped domain example. 85
7.14. *hp*-adapted meshes for our 10-sample cross-shaped domain example. 86
7.15. *hp*-adapted meshes for our 50-sample cross-shaped domain example. 87
7.16. *hp*-adapted meshes for our 100-sample cross-shaped domain example. 88
7.17. Box plots for **different adaptive grids** with a threshold maximum relative error set at 1.0%. 89
7.18. Absolute value of the solutions of our Poisson example. 91
7.19. *hp*-adapted meshes for our 1-sample grid-based domain example. . 92
7.20. *hp*-adapted meshes for our 5-sample grid-based domain example. . 93
7.21. *hp*-adapted meshes for our 10-sample grid-based domain example. 94
7.22. *hp*-adapted meshes for our 50-sample grid-based domain example. 95
7.23. *hp*-adapted meshes for our 100-sample grid-based domain example. 96
7.24. Box plots for **different adaptive grids** with a threshold maximum relative error set at 1.0% 97

List of Tables

7.1. The computational cost based on the factorization cost of generating the database using the SAGO strategy. 80
7.2. The computational cost based on the factorization cost of generating the database using the MAGO strategy. 80
7.3. The computational cost based on the factorization cost of generating the database using the SAGO strategy. 90
7.4. The computational cost based on the factorization cost of generating the database using the MAGO strategy. 90
7.5. The computational cost based on the factorization cost of generating the database using the SAGO strategy. 98
7.6. The computational cost based on the factorization cost of generating the database using the MAGO strategy. 98

1. Introduction

1.1. Motivation

In recent years, the Finite Element Method (FEM) has gained significant popularity as one of the most extensively utilized numerical techniques in computational mechanics and civil engineering. The beginnings of the FEM can be traced back to Courant's pioneering work in 1943 [56], where he employed the Ritz method of numerical analysis and the minimization of variational calculus to derive approximate solutions for vibration systems. However, the computational success and widespread of the FEM can be attributed to the contributions of Turner et al. in 1956 [187] and Clough in 1960 [49].

The FEM has revolutionized various knowledge areas, driven by its primary application in structural mechanics [25, 27, 94, 165, 211]. Its significant impact extends to disciplines such as earthquake engineering, transforming the understanding and practices in these fields [48, 51]. Furthermore, through continuous research, the FEM application has expanded beyond structural mechanics. It has applications in various disciplines, including fluid mechanics, thermal analysis, and electrical engineering.

The popularity of the FEM can be attributed to its capability to represent mathematical models through the weak variational formulation of Partial Differential Equations (PDEs). This formulation enables decomposing the problem domain into finite elements, with a corresponding number of unknowns called Degrees of Freedom (DoF). This decomposition makes it computationally feasible to obtain accurate solutions even in complex geometries (see, e.g., [69, 98, 109, 212, 213, 214] among others). We refer to the interested reader seeking a comprehensive mathematical foundation of the FEM to [33, 47, 127, 164].

Despite the significant advancements made in FEM over the past century [125], the computational cost of achieving highly accurate solutions remains a challenge. As the desired level of solution accuracy increases, the number of unknowns and computational resources required also escalate, potentially resulting in computationally expensive calculations that may be prohibitive in practice.

The h-adaptive FEM addresses the computational costs of increasing solution accuracy. The method designs more efficient meshes by locally reducing the mesh size h while keeping the polynomial order of approximation p fixed (typically

$p = 1, 2$). This dynamic adjustment of the mesh resolution through h-adaptivity facilitates the acquisition of accurate solutions while mitigating computational costs.

The classical h-adaptive FEM involves locally refining elements by reducing their size h [18]. It has successfully achieved convergence rates regarding DoF through mesh adaptation [133]. Pioneering works by Babuška and Rheinboldt [15, 16, 17] have laid the foundation for this approach. However, it is essential to note that this method has limitations in overcoming algebraic convergence rates, resulting in slow convergence. Furthermore, the practical implementation of this method may be constrained by limited computer resources, as the computational demands can present significant challenges.

An alternative approach to the h-adaptive FEM is the p-adaptive FEM [19, 42, 71, 183], which locally enriches the polynomial space p while keeping the mesh size h constant. This method proves to be more practical for problems with smooth solutions, as it can achieve the same level of accuracy with a slightly refined mesh. One of the key advantages of the p-adaptive FEM is that by increasing the polynomial order of approximation p, it attains exponential convergence rates while simultaneously reducing the number of Degrees of Freedom (nDoF) required to achieve a desired level of accuracy.

Non-smooth problems are prevalent in computational mechanics, especially in regions characterized by e.g. re-entrant corners and material interfaces, demanding precise simulations for accurate results. To address this, a combined approach of both adaptive techniques, namely the hp-adaptive FEM [87, 88], has emerged as an efficient alternative. This approach enables a more precise mesh refinement by adjusting the element size h near singularities and the polynomial approximation order p in regions with smooth solutions. By dynamically adapting both h and p, the hp-adaptive FEM achieves exponential convergence rates, even in the presence of singularities [14], thereby offering higher accuracy for the same nDoF. To gain insight into the historical development of the FEM, it is valuable to refer to the works of Babuška [13] and Oden [126].

1.2. Literature review

1.2.1. Advances in hp-adaptivity

Adaptivity entails the selective modification of specific subdomains approximations within the computational domain rather than uniformly altering the approximation over the entire domain. By focusing on relevant subdomains, adaptivity aims to optimize the accuracy and efficiency of the solution while minimizing computational costs. This iterative process concentrates computational resources

on regions where accuracy improvements are most crucial, resulting in improved overall efficiency and accuracy of the solution.

Adaptivity is critical in optimizing computational resources, particularly when they are limited. The primary objective is to achieve the highest level of accuracy while minimizing the nDoF required. The critical components for successful mesh adaptation include *a posteriori* error estimates [2, 3, 4] based on the computed solution, local error indicators, and a strategy that utilizes these indicators to adapt the mesh automatically [22]. Clough's work [50] stands out as a pioneering contribution to developing a fully automated computer program for FEM analysis. Additionally, we shall mention Bank et al. [24] for their pioneering work in developing a global mesh adaptive algorithm.

A wide range of h-adaptive algorithms are available, and here are a few notable examples. Deuflhard et al. [67] introduced the KASKADE code [75, 167], which utilizes hierarchical finite element bases as proposed by Yserentant [204]. In addition to KASKADE, other notable codes for addressing nonlinear problems include PLTMG, developed by Bank [23], and NFEARS [115, 116], developed by Mesztenyi and collaborators, among them. We also encounter, the work of Karniadakis et al. [101, 202, 206] in spectral/hp elements applied to incompressible and compressible flow problems. This approach combines the h-adaptive FEM with the desirable numerical properties of spectral methods. One of the complexities of this method is the requirement of two compatible meshes, which adds a challenge to the computational process.

In addition to h-adaptive algorithms, B. A. Szabó et al. [1, 73, 181, 182] employed a p-adaptive process and rely on *a priori* assumptions to design a mesh that is adequately adapted to the exact solution. Moreover, in hp-adaptive algorithms, G. W. Zumbusch [215] introduced an hp-adaptive algorithm based on the adaptive multilevel code, KASKADE. Additionally, J. Schöberl [173] developed a mesh generator capable of generating new meshes (re-meshing) to support the hp-adaptive process.

The work of Demkowicz et al. [62, 64, 66], and its applications [7, 8, 37, 80, 81, 84, 139, 140, 141, 145, 147, 149], proposed a method that produces optimal hp-meshes by minimizing the local projection error based on a reference solution. However, this approach requires implementing a Projection-Based Interpolation (PBI) and involves computationally expensive computations on a globally refined $(\frac{h}{2}, p+1)$-grid. In addition, ensuring continuity—via the 1-irregularity rule—leads to complex implementations.

Other hp strategies in the field include the Texas three-step approach [128], which involves alternating between h- and p-refinements. However, this method often produces suboptimal results. Another strategy, proposed in [5], is based on the local regularity of the exact solution. Its suitability for industrial applica-

tions remains uncertain, and it shares this limitation with specific Discontinuous Galerkin (DG) methods [10, 38, 39, 54, 63, 82, 83, 93, 154]. For a comprehensive review and comparison of existing *hp*-adaptive strategies up to 2014, please refer to [118].

Implementing high-order *hp*-meshes presents several challenges, particularly regarding the occurrence of *hanging nodes* during local *h*-refinements [68, 179]. These nodes must be constrained to ensure solution continuity. However, managing the data structures necessary to handle *hanging nodes* is complex and involves numerous technical difficulties. To simplify implementation, especially in higher dimensions, researchers [62, 184], among others, limit their algorithms to the *1-irregularity* rule, which allows for a maximum of one level of *hanging nodes*.

To address these challenges and reduce implementation complexity, Zander et al. introduced a novel data structure in their work [207, 208, 210] that supports *hp*-discretizations and inherently eliminates *hanging nodes*. Their approach utilizes hierarchical basis functions in h and p on a multi-level grid, employing uniform refinements with many Dirichlet nodes to ensure continuity and enable local refinements. Replacing global uniform refinements with isotropic refinements over selected elements eliminates *hanging nodes* while simplifying existing data structures for *hp*-refinements. Kopp et al. [104, 105] have extended these data structures to arbitrary dimensions [105] and space-time discretizations [104], expanding the approach's applicability.

In 2020, Darrigrand et al. [59] proposed a new automatic *hp*-adaptive mesh-refinement strategy for elliptic problems that build upon Zander's data structures [207, 208, 210]. Their approach not only eliminates mesh irregularities caused by *hanging nodes* but also avoids implementations of local projections (e.g., PBI [66]) that require the maintenance of multiple grids in the data structures. This easy-to-implement *hp*-strategy consists of a general (user-defined) refinement step followed by a specific mesh coarsening step. The method uses quadrilateral elements and alternates between global h- or p-refinements with local and quasi-optimal *hp*-unrefinements (similarly to [29, 40]). In particular, the method eliminates basis functions with the lowest contributions to the solution energy at each *hp*-unrefinement step.

The coarsening-based strategy described earlier provides a significant benefit. It can address and rectify inevitable "mistakes" that may have occurred due to undesired basis functions introduced during global refinements or in the pre-asymptotic regime. Moreover, subsequent unrefinement iterations can further enhance the results, improving upon any potential non-optimal results that may have arisen due to the approximate quasi-orthogonality assumption of the basis functions.

Due to the inherent complexity of the *hp*-adaptive algorithms, both convergence

[59, 62, 161], and optimality are desirable properties. Optimality is obtaining the best solution using limited DoF. Canuto et al. [40] have provided proof of optimality in 1D and 2D problems, demonstrating the ability to achieve optimal solutions within the given DoF constraints. On the other hand, convergence measures how closely the computed solution approaches the exact solution of the problem. For a comprehensive understanding of convergence theory in the context of FEM, Ciarlet [46, 47] provides a valuable reference. We shall mention specific algorithms that have provided convergence proofs [30, 36, 41, 58].

1.2.2. Advances in Goal-Oriented adaptivity

Adaptivity aims to maximize the efficiency of computational resources while achieving the desired level of accuracy in the solution. The conventional approach to adaptivity, which estimates the error in a global norm (e.g., L^2 or H^1), may sometimes fail to align with the specific requirements of applications. The need to control errors in specific Quantities of Interest (QoIs), rather than the overall energy of the solution, is common in many engineering applications. These requirements have driven the development of Goal-Oriented Adaptive (GOA) strategies.

The development of Goal-Oriented (GO) adaptivity, aimed at efficiently approximating specific Quantity of Interest (QoI) with reduced computational cost, can be attributed to the pioneering works of Rannacher et al. [26, 162, 163]. Peraire and Patera [114, 137, 138, 152, 153, 172] further expanded upon these foundational studies. These researchers focused on deriving *a posteriori* error estimates that explicitly target the error in the QoIs.

Traditional approaches for representing the error in the QoI involve utilizing the direct and adjoint solutions and the global bilinear form of the problem. This representation is then partitioned into local and computable quantities, which are used to guide local refinements (see, for example, [134]). In the context of goal-oriented error estimation, Prudhomme and Oden [129, 130, 156, 157] developed a procedure that employs global functions defined over the entire computational domain to represent the error in the QoI. They also proposed a method to estimate lower and upper bounds on the QoI error using global energy error estimates, with the bounds determined by the sum of local indicators.

The convergence analysis of adaptive algorithms can be attributed to the early works of Dörfler and Morin [70, 121]. Before 2006, most goal-oriented methods were not proven to converge, although there were two exceptions [57, 120]. However, significant progress has been made since then, with the development of algorithms that exhibit exponential convergence rates for specific solution properties. For instance, Mommer [119] proposed an adaptive finite element method for approximating functionals of the solution of symmetric elliptic second-order

boundary value problems. In 2012, Pollock's dissertation [155] presented a convergence theory for a class of goal-oriented adaptive finite element algorithms, including works on second-order non-symmetric [92] and semilinear [91] elliptic equations. Moreover, Feischl [76] performed an abstract analysis of optimal GO adaptivity. Numerical results demonstrating convergence have been provided by Darrigrand et al. [60, 61] and Valseth et al. [189], offering insightful examples.

GO adaptivity has gained significant importance in various engineering applications, such as electromagnetics [142, 143, 144]. A noteworthy example is the work in [178], where the authors devised a GOA strategy that eschews explicit error estimates for guiding *hp*-refinements. Instead, they employ a suitable reference solution to recover an approximate error function, which provides a substantially more accurate approximation than the one obtained on the coarse mesh. In a related study [148], the authors further investigated the effectiveness of the GO *hp*-adaptive strategy by employing analytical techniques such as the Fourier transform and Bessel functions. Specifically, they focused on a problem involving the radiation of a loop antenna wrapped around a metallic cylinder into a conductive medium.

The application of GO adaptivity in structural problems has its roots in the seminal works by Oden et al. [132] and Vemaganti et al. [197]. These pioneering studies laid the foundation for the theory and methodologies of GO adaptivity in modeling heterogeneous materials. Subsequent advancements in the field were made by Oden et al. [131], who explored GO adaptivity in discrete lattice models, and Romkes et al. [169], who investigated elastostatic problems of heterogeneous materials with material properties expressed as functions of random variables. In 2012, Jhurani et al. [96, 97] introduced a framework for numerical homogenization and GO adaptivity for non-linear lattice elasticity problems based on the Moore-Penrose pseudo-inverse of element stiffness matrices. Furthermore, Panetier et al. [135], Verdugo et al. [198], and Waeytens et al. [200] made notable contributions to the application of GO adaptivity in the field of viscoelasticity. In the context of linear viscoelasticity, the works of Chamoin et al. [45] and Ladevèze et al. [107, 108] are worth mentioning, as they developed error bounds for outputs of interest.

The application of GO adaptivity in the context of fluid-structure interactions can be traced back to the pioneering research of Th. Dune [72]. Dune's work introduced an innovative Eulerian framework for modeling fluid-structure interactions, which incorporated *a posteriori* GO error estimation as a fundamental component of the methodology. In [86], authors developed a nonlinear GO error estimation procedure tailored explicitly to analyze Navier-Stokes incompressible fluid flows with structural interactions. During his Ph.D. dissertation, K. G. van der Zee made significant contributions to fluid-structure interactions [190], fur-

ther extending the understanding and application of GO adaptivity in this area. One example of his contributions can be seen in [193], where authors developed a GO error estimator tailored for finite-element discretizations of fluid-structure-interaction problems. Their study focused on a model problem involving steady Stokes flow in a 2D channel with a flexible section of the channel wall.

Moreover, valuable contributions were made in free-boundary problems, as demonstrated in [194, 195]. Additionally, in [196], GO error estimation in the context of free-boundary problems, where GO error estimation was applied using isogeometric analysis, was explored. K. G. van der Zee and colleagues also made other noteworthy contributions. In [192], they presented rigorous derivations of exact linearized adjoints for a coupled fluid-structure problem. At the same time, in [191], they developed *a posteriori* estimate of errors in the QoI for the nonlinear system of evolution equations embodied in the Cahn-Hilliard model of binary phase transition.

1.3. Main contributions of the dissertation

The present dissertation summarizes the main contributions as follows. First, we extend the energy-based approach proposed by Darrigrand et al. [59] to the context of h- and p-GOA algorithms. To achieve this, we combine the energy-based approach with an alternative pseudo-dual operator for representing the error in the QoI [60]. Our proposed approach is based on defining a new representation for the residual error of the adjoint problem, which exhibits better properties than the original bilinear form (e.g., positive definiteness). This new representation has been successfully used in previous studies [61, 123] and allows us to compute the error in the QoI in a way similar to classical approaches. As a result, we obtain automatic GO h and p-adaptive algorithms for non-elliptic problems.

Second, we extend the energy-based-adaptive hp-strategy proposed by Darrigrand [59] to non-elliptic equations. To achieve this, we provide an alternative estimation of the energy contribution in terms of an inner product that depends on the bilinear form of the problem. As a result, we obtain an automatic hp-adaptive algorithm for non-elliptic problems.

Third, we extend Darrigrand's strategy [59] to GOA approaches for both elliptic and non-elliptic problems. To achieve this, we use the adjoint problem to construct an upper bound of the error representation expressed in terms of an inner product that depends on the bilinear form of the problem. As a result, we obtain an automatic GO hp-adaptive algorithm for elliptic and non-elliptic problems.

Our algorithms exhibit robustness and straightforward implementation, making them suitable for industrial applications. Notably, our approaches do not

require the computation of reference solutions on very fine grids, unlike other methods such as [66]. Our approach is limited to anisotropic p and isotropic h-refinements. However, recent work by Zander et al. [209] has extended multi-level data structures to support anisotropic h-refinements. To showcase the effectiveness of our algorithms, we demonstrate the convergence of our h and p-adaptive algorithms in 1D Helmholtz and convection-diffusion equations. Additionally, we test and analyze our hp-adaptive algorithm in three different 2D problems based on Poisson, Helmholtz, and convection-diffusion equations. Furthermore, we provide numerical results for a 3D Helmholtz-like problem.

Although it is possible to construct suitable *a posteriori* error estimators [4, 26, 163] to enhance the refinement step of the algorithm, this possibility is outside the scope of this dissertation.

Lastly, we extend Caro et al.'s [43] work to parametric PDEs. We develop an efficient way to generate reliable databases containing hundreds of thousands of synthetic data or measurements while minimizing computational costs for training Deep Neural Networks (DNNs). Due to the limited capabilities of Deep Learning (DL) techniques in solving PDEs, we approximate the forward operator. We adopt a modified version of the GO hp-adaptive FEM strategy [43, 44], unlike Hashemian et al.'s [90] study, which used a refined Isogeometric Analysis (IGA) approach to create databases of up to 100,000 Earth models.

1.4. Outline

In this dissertation, we discuss the data structures presented by Zander et al. [207, 208, 210] in Section 2.1 of Chapter 2. We also introduce the concept of *removable* basis functions in Section 2.1.1, an essential idea in this dissertation. In Chapter 3, we present the adaptive strategy and element-wise error indicators. Our coarsening policy is introduced in Section 3.1, and we define the concept of *projectors* in Section 3.2, which applies to a single finite element mesh. We derive error indicators in Section 3.3, which guide the adaptivity for energy-norm and GO adaptivity. The methodology is applied to both elliptic and non-elliptic problems. Chapter 4 provides numerical results for 1D problems using the h- and p-GOA algorithms proposed in this dissertation. We detail the proposed algorithms in Section 4.1 and outline the error indicators used in our h- and p-adaptive algorithms in Section 4.2. We present numerical results demonstrating the convergence of the proposed h- and p-GOA algorithms for 1D Helmholtz and convection-diffusion equations in Section 4.3. Finally, Section 4.4 summarizes the numerical results presented in this chapter. Chapter 5 illustrates the performance of our hp-adaptive algorithm numerically. We demonstrate the exponential convergence behavior of the approach for various 2D problems. Specifically, Section

5.1 showcases the numerical results for the 2D Poisson equation, while Section 5.2 displays the results for the 2D Helmholtz equation. Additionally, we provide numerical results for the 2D convection-diffusion equation in Section 5.3. Finally, Section 5.4 summarizes the numerical results presented in this chapter. In Chapter 6, we present the numerical results for 3D problems. Section 6.1 showcases a wave propagation problem and presents the energy norm and goal-oriented adaptivity results. Finally, Section 6.2 summarizes the numerical results presented in this chapter. Chapter 7 examines the performance of our Multi-Adaptive Goal-Oriented (MAGO) *hp*-strategy. Section 7.1 showcases the extension of the *hp*-strategy for non-parametric PDEs to parametric PDEs. Moreover, we describe the generation of databases in Section 7.2. Finally, Section 7.3 summarizes the numerical results presented in this chapter. We use the 2D Helmholtz equation to illustrate the effectiveness of our strategy. Chapter 8 summarizes the critical accomplishments of this dissertation, while Chapter 9 presents the dissertation's concluding remarks and future work.

Part I.

Goal-Oriented hp-adaptivity for non-parametric PDEs

2. Multi-level hp-meshes

2.1. Data structures

Classical adaptive schemes involve refining a coarse mesh to obtain finer ones, which can lead to the appearance of *hanging nodes* during local h or hp refinements. These nodes must be constrained to ensure the global continuity of the approximate solution. However, this requirement often creates significant implementation challenges (see, e.g., [160]).

In 1971, Mote proposed an alternative procedure by combining the finite element Ritz method following the idea of refining by superposition (see, e.g., [122, 124]). This approach, nowadays known as superposition techniques, maintains an initial *base* discretization unmodified and subsequently overlaps one (or several) finer *overlay* mesh(es). Accordingly, the initial coarse grid captures the large-scale characteristics of the solution while the overlaying mesh(es) reproduces the small-scale features. In 2015, Zander et al. [208] took advantage of this superposition idea and proposed a data structure that enables local hp-mesh refinements and unrefinements while efficiently handling the constrained *hanging nodes* that naturally appear during local h-refinements (see, e.g., [64, 179]).

Following the data structures introduced in [208], we impose a massive number of Dirichlet nodes throughout the overlay mesh(es), thus ensuring the continuity of the solution by construction. Basically, in the overlay meshes, we only add globally continuous *basis functions* (see Figure 2.1) rather than possibly discontinuous *shape functions* (see, e.g., [59, 208]). That leads to a relatively simple implementation where imposing the one-irregularity rule [66] is unnecessary. In addition, to guarantee the linear independence of the basis functions, high-order basis functions are only activated on those elements with no further refinements in h (see Figure 2.1). Such elements without further refinements may be encountered even in the initial level of the mesh in the case of unrefined elements. In particular, when performing an h-refinement, high-order basis functions are transferred to the children. For further details, we refer the reader to [210].

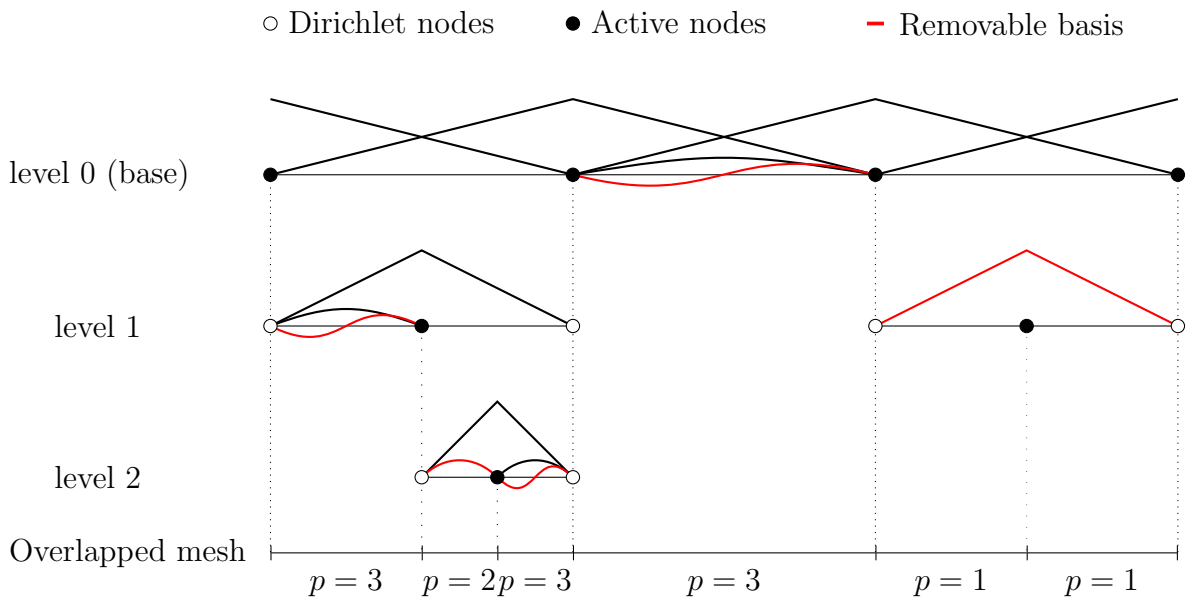

Figure 2.1.: Illustration of a 1D multi-level *hp*-grid with hierarchical basis functions and Dirichlet nodes. *Removable* basis functions are indicated in red.

2.1.1. Removable basis functions in a multi-level hp-mesh

In 2020, Darrigrand et al. [59] proposed an easy-to-implement *hp*-adaptive strategy for elliptic problems that exploited Zander's data structures [210]. The main idea of this work consists of incorporating a coarsening strategy that identifies the basis functions that can be *directly* removed. Hence, we define these *removable* basis functions as those we can eliminate from the discretization without modifying any other basis function while preserving complete polynomial spaces. Figure 2.1 shows the removable basis functions in red and the non-removable basis functions in black.

For 2D and 3D problems, our current implementation defines the basis functions as tensorial products of the 1D basis functions. Additionally, we incorporate anisotropic p and isotropic h refinements. However, according to the recent work of Zander et al. [209], it could be possible to extend these ideas to anisotropic h-refinements. To find specific details about the discretization and the properties of the genealogy tree (which are beyond the scope of this dissertation), we refer the interested reader to [59]. For further details and the specifications about the extension to 2D and 3D data structures, we refer to [210].

3. Goal-Oriented coarsening strategy

This chapter describes our adaptive strategy and the error indicators we use to guide the *hp*-unrefinement steps. We begin by outlining our mesh generation and coarsening policy algorithmically. Following that, we introduce *projectors* and their role in a single finite element mesh, enabling us to simulate a second grid's presence while working with only one. Lastly, we derive the error indicators in the coarsening steps for various strategies, including energy-norm, Goal-Oriented (GO), and elliptic and non-elliptic problems.

3.1. Unrefinement policy

Adaptive Finite Element Methods (FEMs) aim to reduce computational costs while ensuring low discretization errors. In this dissertation, we employ the adaptive algorithm introduced in [59]. This algorithm iterates through the following steps for a given *hp*-grid:

1. Perform a user-defined mesh refinement. In our implementation, we alternate between global and uniform h- and $p = p + 2$-refinements.

2. Perform a (quasi)-optimal *hp*-coarsening step.

This procedure is illustrated in Algorithm 1. We emphasize that these repeated uniform global refinements guarantee the convergence of the approach. In contrast, the coarsening step ensures nearly optimal convergence rates [29, 40].

Similarly to [59], the main ingredients of our *hp*-coarsening step (see Algorithm 2) are:

1. To compute the solution on the current mesh.

2. For each element of the mesh:
   a) To find the *removable* basis functions whose support contains the element.
   b) To calculate the contribution of the *removable* basis functions to the solution.

Algorithm 1: Adaptive process

Input: A given initial mesh
Output: A final *hp*-adapted mesh
while *error above tolerance* **do**
  Perform a global and uniform (h or p) refinement;
  Execute a (quasi)-optimal *hp*-coarsening step (Algorithm 2) to the mesh;
  Update error;
end

3. Remove the basis functions with small contributions.

The above process is repeated until no basis function is eliminated. Figure 3.1 illustrates the h-unrefinement policy. A given coarse mesh in Figure 3.1a is h-refined globally in Figure 3.1b. Then, after an unrefinement process, we obtain the adapted mesh displayed in Figure 3.1c.

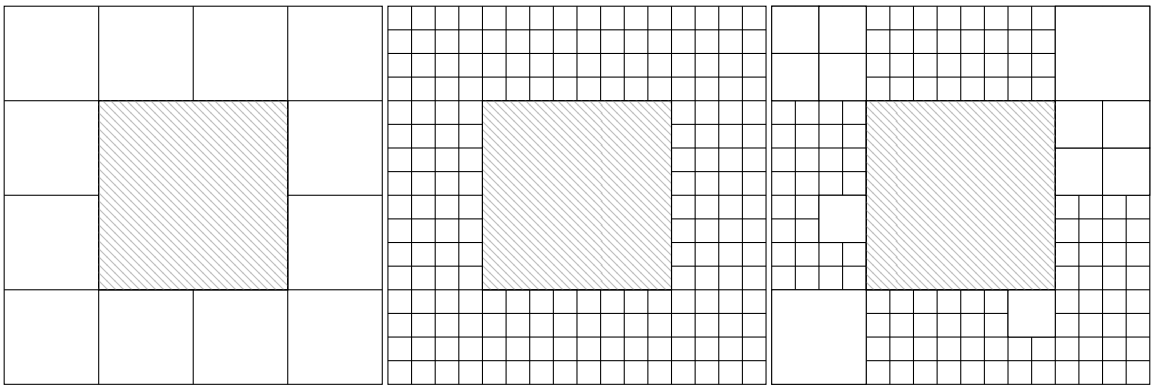

(a) A initial (given) mesh. (b) An h-refined mesh. (c) An h-adapted mesh.

Figure 3.1.: Adaptive process illustrated over a square domain with a hole in the middle (marked in gray).

The definition of the contributions of the *removable* basis functions to the solution is problem-dependent. To provide representative quantities for energy-norm-based and Goal-Oriented Adaptive (GOA) strategies over elliptic and non-elliptic problems, we first introduce our *projectors* in a single finite element grid context.

Algorithm 2: *hp*-unrefinement policy

Input: A given mesh
Output: An *hp*-unrefined mesh
do
Compute the solution on the current mesh;
Compute the element-wise error indicators;
Unrefine the mesh by eliminating the *removable* basis functions with low error indicators;
When no contributions are below a given tolerance, exit;
end ;

3.2. Projectors

For dimension $d \in \{1, 2, 3\}$, let $\Omega \subset \mathbb{R}^d$ be an open bounded domain with a Lipschitz-continuous boundary $\partial\Omega$, and let $\mathbb{H}(\Omega)$ be a Hilbert functional space on Ω (simply denoted as $\mathbb{H}$ in the following). For a given continuous bilinear form b defined on $\mathbb{H} \times \mathbb{H}$, let us define our problem with the following abstract variational formulation:

Find $u \in \mathbb{H}$ such that

$$b(u, \phi) = f(\phi), \quad \forall \phi \in \mathbb{H}, \tag{3.1}$$

where f is a linear form. The discrete counterpart of this abstract variational formulation reads as follows:

Find $u_{\mathcal{F}} \in \mathbb{H}_{\mathcal{F}}$ such that

$$b(u_{\mathcal{F}}, \phi_{\mathcal{F}}) = f(\phi_{\mathcal{F}}), \quad \forall \phi_{\mathcal{F}} \in \mathbb{H}_{\mathcal{F}}, \tag{3.2}$$

where $\mathbb{H}_{\mathcal{F}} \coloneqq \operatorname{span}\{\phi_1, \ldots, \phi_{n_{\mathcal{F}}}\}$ is a finite element discretization $\mathcal{T}$ of $\mathbb{H}$, such that $\mathbb{H}_{\mathcal{F}} \subset \mathbb{H}$, $\mathcal{F} = \{\phi_i\}_{i=1}^{n_{\mathcal{F}}}$ is a set of basis functions ϕ_i, and $n_{\mathcal{F}} = \dim(\mathbb{H}_{\mathcal{F}})$. Besides, $u_{\mathcal{F}}$ corresponds to the Galerkin approximation of u in $\mathbb{H}_{\mathcal{F}}$.

Some *hp* techniques handle a fine and a coarse mesh at the same time (see, e.g., [62, 64]). In addition to the coding difficulties derived from this fact, they typically need to define and implement projection operators (such as the Projection-Based Interpolation (PBI)) to link both grids. One of the main characteristics of our "painless" approach is continuously operating on a single mesh. While it simplifies the implementation, it requires defining a simple projector that simulates the presence of a coarse mesh without the trouble of handling one.

For a given subset of basis functions $\mathcal{S} \subset \mathcal{F}$ that generates the space $\mathbb{H}_{\mathcal{S}} \subset \mathbb{H}_{\mathcal{F}}$, we define our *projection operator* $\Pi_{\mathcal{F}}^{\mathcal{S}}$: $\mathbb{H}_{\mathcal{F}} \longrightarrow \mathbb{H}_{\mathcal{S}}$ as

$$\Pi_{\mathcal{F}}^{\mathcal{S}} u_{\mathcal{F}} \coloneqq \sum_{\phi_i \in \mathcal{S}} u_i \phi_i, \tag{3.3}$$

that is, we extract the coefficients of $u_{\mathcal{F}}$ corresponding to the basis functions in $\mathcal{S}$, and we set the others to zero.

For any element K, we denote by $\mathcal{R}_K$ the set of *removable* basis functions (see Section 2.1.1) associated to K, by $|\mathcal{R}_K|$ its cardinality, and by $\mathbb{H}_{\mathcal{R}_K}$ its associated space. Additionally, we define the subset of *essential* basis functions $\mathcal{E}_K$ as $\mathcal{E}_K \coloneqq \mathcal{F} \setminus \mathcal{R}_K$, while its associated space is denoted by $\mathbb{H}_{\mathcal{E}_K}$. These spaces satisfy that $\mathbb{H}_{\mathcal{E}_K} \subset \mathbb{H}_{\mathcal{F}}$, $\mathbb{H}_{\mathcal{R}_K} \subset \mathbb{H}_{\mathcal{F}}$, and $\mathbb{H}_{\mathcal{F}} = \mathbb{H}_{\mathcal{E}_K} \cup \mathbb{H}_{\mathcal{R}_K}$, with $\mathbb{H}_{\mathcal{E}_K} \cap \mathbb{H}_{\mathcal{R}_K} = \emptyset$. As a consequence, we can express any $u_{\mathcal{F}} \in \mathbb{H}_{\mathcal{F}}$, as:

$$u_{\mathcal{F}} = \Pi_{\mathcal{F}}^{\mathcal{E}_K} u_{\mathcal{F}} + \Pi_{\mathcal{F}}^{\mathcal{R}_K} u_{\mathcal{F}}. \tag{3.4}$$

Since we consider a single mesh at a time, the solution $u_{\mathcal{E}_K}$ in $\mathcal{E}_K$ associated to eq. (3.2) is, in fact, never computed. Instead, we employ the projection of $u_{\mathcal{F}}$ into $\mathcal{E}_K$ to approximate it when necessary.

3.3. Error indicators

Let $\|\cdot\|_e$ be the *energy norm* associated with the Hilbert space $\mathbb{H}$. For elliptic problems (given by symmetric and positive-definite bilinear forms), we define this energy from the bilinear form of the problem b, that is, $\|\cdot\|_e^2 = b(\cdot,\cdot)$. For each non-elliptic problem, we shall define an alternative operator a —not necessarily the original bilinear form— such that $|b(\phi,\psi)| \leq |a(\phi,\psi)|\ \forall \phi,\psi \in \mathbb{H}$ and $\|\cdot\|_e^2 = a(\cdot,\cdot)$ is the energy norm of the problem (i.e., a defines an inner product). We emphasize that the choice of these operators might highly influence the results of the adaptive process, which is usually an essential ingredient of adaptive strategies.

With this in mind, our objective is to provide representative element-wise error indicators that drive the *hp*-coarsening steps (see Algorithm 2). For that, we consider isotropic and anisotropic indicators that are problem-dependent. In the following subsections, we derive only the isotropic error estimators $\eta_K, \forall K \in \mathcal{T}$ for a wide range of problems (see [59], for anisotropic indicators).

To select what basis functions to unrefine, we compute the error indicators' average (per degree of freedom) for the removable basis functions. We subsequently eliminate the *removable* basis function whose contribution is smaller than a percentage of this average. For further details and implementation technicalities, see [59].

In the following, we summarize the results from Darrigrand et al. [59] for elliptic energy-norm-based adaptive problems from the energy-norm perspective. After that, we extend these results to non-elliptic equations, and finally, we consider GO adaptivity applied to elliptic and non-elliptic problems. We can obtain all the proposed results by assuming (quasi)-b-orthogonality of the basis functions. However, this assumption is strong and unneeded for the energy-based adaptivity, and, therefore, we only employ it for GO adaptivity.

To do so, let us denote by "$\lesssim$" the inequality that holds up to a constant; that is, we represent $a \leq Cb$ by $a \lesssim b$, with $a, b, C \in \mathbb{R}$, and let us define the L^2-inner product of two possible complex and possibly vector-valued functions g_1 and g_2 as:

$$\langle g_1, g_2 \rangle_{L^2(\Omega)} = \int_\Omega \left(g_1^*\right)^T g_2 \, d\Omega, \tag{3.5}$$

where g^T is the transpose of g, while g_1^* represents the complex conjugate of g_1.

3.3.1. Energy-norm based elliptic problems

For a given element $K \in \mathcal{T}$, the objective is to quantify how much energy we lose in the solution when removing a subset of basis functions of the set of *removable* basis functions $\mathcal{R}_K$. Specifically, we want to compute $\|u_\mathcal{F} - u_{\mathcal{E}_K}\|_e^2$. If this quantity is small, we guarantee that the energy of the removed set of basis functions is insignificant. Therefore, the fine and the unrefined meshes would provide comparable results.

Analogously to Cea's lemma proof, we derive:

$$\begin{aligned}
\|u_\mathcal{F} - u_{\mathcal{E}_K}\|_e^2 &= b\left(u_\mathcal{F} - u_{\mathcal{E}_K}, u_\mathcal{F} - u_{\mathcal{E}_K}\right) && (3.6)\\
&= b\left(u_\mathcal{F} - u_{\mathcal{E}_K}, u_\mathcal{F} - \Pi_\mathcal{F}^{\mathcal{E}_K} u_\mathcal{F}\right) + b\left(u_\mathcal{F} - u_{\mathcal{E}_K}, \Pi_\mathcal{F}^{\mathcal{E}_K} u_\mathcal{F} - u_{\mathcal{E}_K}\right) && (3.7)\\
&\leq \|u_\mathcal{F} - u_{\mathcal{E}_K}\|_e \left\|u_\mathcal{F} - \Pi_\mathcal{F}^{\mathcal{E}_K} u_\mathcal{F}\right\|_e, && (3.8)
\end{aligned}$$

where we have used the b-orthogonality of $u_\mathcal{F} - u_{\mathcal{E}_K}$ with $\mathbb{H}_{\mathcal{E}_K}$ and the Cauchy-Schwarz inequality. Therefore,

$$\|u_\mathcal{F} - u_{\mathcal{E}_K}\|_e \leq \left\|u_\mathcal{F} - \Pi_\mathcal{F}^{\mathcal{E}_K} u_\mathcal{F}\right\|_e = \left\|\Pi_\mathcal{F}^{\mathcal{R}_K} u_\mathcal{F}\right\|_e. \tag{3.9}$$

It is then natural to define the following element-wise error indicator:

$$\eta_K \coloneqq \left\|\Pi_\mathcal{F}^{\mathcal{R}_K} u_\mathcal{F}\right\|_e^2, \quad \forall K \in \mathcal{T}. \tag{3.10}$$

3.3.2. Extension to energy-based non-elliptic problems

Again, our purpose is to compute $\|u_\mathcal{F} - u_{\mathcal{E}_K}\|_e^2$ to eliminate the *removable* basis functions with a low contribution to the solution. For that, let us start with the

triangular inequality, which provides that

$$\|u_{\mathcal{F}} - u_{\mathcal{E}_K}\|_e \leq \left\|u_{\mathcal{F}} - \Pi_{\mathcal{F}}^{\mathcal{E}_K} u_{\mathcal{F}}\right\|_e + \left\|\Pi_{\mathcal{F}}^{\mathcal{E}_K} u_{\mathcal{F}} - u_{\mathcal{E}_K}\right\|_e . \tag{3.11}$$

Let us assume now that b satisfies the discrete inf-sup condition:

$$\exists\, \gamma > 0, \quad \inf_{\phi \in \mathbb{H}_{\mathcal{E}_K}} \sup_{\psi \in \mathbb{H}_{\mathcal{E}_K}} \frac{b(\phi, \psi)}{\|\phi\|_e \|\psi\|_e} \geq \gamma. \tag{3.12}$$

Then, using this inequality and the b-orthogonality of $u_{\mathcal{F}} - u_{\mathcal{E}_K}$ with respect to $\mathbb{H}_{\mathcal{E}_K}$, we control the second term of eq. (3.11):

$$\gamma \left\|\Pi_{\mathcal{F}}^{\mathcal{E}_K} u_{\mathcal{F}} - u_{\mathcal{E}_K}\right\|_e \leq \sup_{\psi \in \mathbb{H}_{\mathcal{E}_K}} \frac{b\left(\Pi_{\mathcal{F}}^{\mathcal{E}_K} u_{\mathcal{F}} - u_{\mathcal{E}_K}, \psi\right)}{\|\psi\|_e} \tag{3.13}$$

$$\leq \sup_{\psi \in \mathbb{H}_{\mathcal{E}_K}} \frac{b\left(\Pi_{\mathcal{F}}^{\mathcal{E}_K} u_{\mathcal{F}} - u_{\mathcal{F}}, \psi\right) + b\left(u_{\mathcal{F}} - u_{\mathcal{E}_K}, \psi\right)}{\|\psi\|_e} \tag{3.14}$$

$$\leq \sup_{\psi \in \mathbb{H}_{\mathcal{E}_K}} \frac{M_b \left\|\Pi_{\mathcal{F}}^{\mathcal{E}_K} u_{\mathcal{F}} - u_{\mathcal{F}}\right\|_e \|\psi\|_e}{\|\psi\|_e} \tag{3.15}$$

$$\leq M_b \left\|u_{\mathcal{F}} - \Pi_{\mathcal{F}}^{\mathcal{E}_K} u_{\mathcal{F}}\right\|_e , \tag{3.16}$$

where M_b is the continuity constant of b. Therefore,

$$\|u_{\mathcal{F}} - u_{\mathcal{E}_K}\|_e^2 \lesssim \left\|u_{\mathcal{F}} - \Pi_{\mathcal{F}}^{\mathcal{E}_K} u_{\mathcal{F}}\right\|_e^2 = \left\|\Pi_{\mathcal{F}}^{\mathcal{R}_K} u_{\mathcal{F}}\right\|_e^2 . \tag{3.17}$$

Accordingly, we define the element-wise indicator as follows:

$$\eta_K \coloneqq \left\|\Pi_{\mathcal{F}}^{\mathcal{R}_K} u_{\mathcal{F}}\right\|_e^2, \quad \forall K \in \mathcal{T}. \tag{3.18}$$

The coarsening step will unrefine the elements that exhibit small η_K. Therefore, eq. (3.17) ensures that the problem's energy loss will be negligible when removing these basis functions.

3.3.3. Extension to Goal-Oriented adaptivity

GOA techniques aim to approximate specific quantities of finite element solutions rather than the global energy of the problem. These quantities with particular engineering applications are often called influence functions or Quantities of Interest (QoIs). Thus, the objective is to produce a space $\mathbb{H}_{\mathcal{F}}$ with a minimum dimension such that the error in the Quantity of Interest (QoI) is below a user-prescribed tolerance. To control the error in the QoI, we introduce the following adjoint problem [130, 156] associated to eq. (3.1):

Find $v \in \mathbb{H}$ such that

$$b(\phi, v) = l(\phi), \quad \forall \phi \in \mathbb{H}, \tag{3.19}$$

where $l : \mathbb{H} \longrightarrow \mathbb{R}$ is a linear continuous form. Hence, the QoI of the solution $u_{\mathcal{F}}$ is denoted by $l(u_{\mathcal{F}})$. The discrete equivalent of this problem is given by:

Find $v_{\mathcal{F}} \in \mathbb{H}_{\mathcal{F}}$ such that

$$b(\phi_{\mathcal{F}}, v_{\mathcal{F}}) = l(\phi_{\mathcal{F}}), \quad \forall \phi_{\mathcal{F}} \in \mathbb{H}_{\mathcal{F}}, \tag{3.20}$$

where $v_{\mathcal{F}}$ stands for the Galerkin approximation of the solution v to the adjoint problem associated with the space $\mathbb{H}_{\mathcal{F}}$. For the mathematical analysis, we also consider the solution $v_{\mathcal{E}_K}$ in $\mathcal{E}_K$ associated with eq. (3.20), although we never compute it in practice.

For a given element $K \in \mathcal{T}$, we want to quantify how much the QoI changes when removing some basis functions from the set of *removable* basis functions $\mathcal{R}_K$ associated with K. That is, we need to control $|l(u_{\mathcal{F}}) - l(u_{\mathcal{E}_K})|$, $\forall K \in \mathcal{T}$.

Since $\mathbb{H}_{\mathcal{E}_K} \subset \mathbb{H}_{\mathcal{F}}$, Galerkin orthogonality ensures that

$$b(u_{\mathcal{F}} - u_{\mathcal{E}_K}, \phi) = 0, \quad \forall \phi \in \mathbb{H}_{\mathcal{E}_K}. \tag{3.21}$$

Then,

$$l(u_{\mathcal{F}}) - l(u_{\mathcal{E}_K}) = b(u_{\mathcal{F}} - u_{\mathcal{E}_K}, v_{\mathcal{F}}) = b(u_{\mathcal{F}} - u_{\mathcal{E}_K}, v_{\mathcal{F}} - v_{\mathcal{E}_K}). \tag{3.22}$$

Using eq. (3.4) on $v_{\mathcal{F}}$, we have that:

$$\begin{aligned} l(u_{\mathcal{F}}) - l(u_{\mathcal{E}_K}) &= b\left(u_{\mathcal{F}} - u_{\mathcal{E}_K}, \Pi_{\mathcal{F}}^{\mathcal{R}_K} v_{\mathcal{F}} + \Pi_{\mathcal{F}}^{\mathcal{E}_K} v_{\mathcal{F}} - v_{\mathcal{E}_K}\right) && (3.23)\\ &= b\left(u_{\mathcal{F}} - u_{\mathcal{E}_K}, \Pi_{\mathcal{F}}^{\mathcal{R}_K} v_{\mathcal{F}}\right) + b\left(u_{\mathcal{F}} - u_{\mathcal{E}_K}, \Pi_{\mathcal{F}}^{\mathcal{E}_K} v_{\mathcal{F}} - v_{\mathcal{E}_K}\right). && (3.24) \end{aligned}$$

Again, thanks to Galerkin orthogonality the second term vanishes. Then, applying eq. (3.4) on $u_{\mathcal{F}}$ to the remaining term, we have that

$$\begin{aligned} l(u_{\mathcal{F}}) - l(u_{\mathcal{E}_K}) &= b\left(\Pi_{\mathcal{F}}^{\mathcal{R}_K} u_{\mathcal{F}} + \Pi_{\mathcal{F}}^{\mathcal{E}_K} u_{\mathcal{F}} - u_{\mathcal{E}_K}, \Pi_{\mathcal{F}}^{\mathcal{R}_K} v_{\mathcal{F}}\right) && (3.25)\\ &= b\left(\Pi_{\mathcal{F}}^{\mathcal{R}_K} u_{\mathcal{F}}, \Pi_{\mathcal{F}}^{\mathcal{R}_K} v_{\mathcal{F}}\right) + b\left(\Pi_{\mathcal{F}}^{\mathcal{E}_K} u_{\mathcal{F}} - u_{\mathcal{E}_K}, \Pi_{\mathcal{F}}^{\mathcal{R}_K} v_{\mathcal{F}}\right). && (3.26) \end{aligned}$$

Additionally, if we assume that $\mathcal{E}_K$ is (quasi) b-orthogonal to $\mathcal{R}_K$ due to the (quasi)-orthogonality assumption of the basis functions, then

$$b\left(\Pi_{\mathcal{F}}^{\mathcal{E}_K} u_{\mathcal{F}} - u_{\mathcal{E}_K}, \Pi_{\mathcal{F}}^{\mathcal{R}_K} v_{\mathcal{F}}\right) \simeq 0, \tag{3.27}$$

and consequently,

$$|l(u_{\mathcal{F}}) - l(u_{\mathcal{E}_K})| \simeq \left|b\left(\Pi_{\mathcal{F}}^{\mathcal{R}_K} u_{\mathcal{F}}, \Pi_{\mathcal{F}}^{\mathcal{R}_K} v_{\mathcal{F}}\right)\right| \leq \left|a\left(\Pi_{\mathcal{F}}^{\mathcal{R}_K} u_{\mathcal{F}}, \Pi_{\mathcal{F}}^{\mathcal{R}_K} v_{\mathcal{F}}\right)\right|. \tag{3.28}$$

Then, we define the element-wise indicators as

$$\eta_K \coloneqq \left|a\left(\Pi_{\mathcal{F}}^{\mathcal{R}_K} u_{\mathcal{F}}, \Pi_{\mathcal{F}}^{\mathcal{R}_K} v_{\mathcal{F}}\right)\right|, \quad \forall K \in \mathcal{T}. \tag{3.29}$$

Here again, eq. (3.28) ensures that eliminating the basis functions associated with small indicators during the coarsening process should have a limited effect on the error of the QoI.

Remark: Since b is continuous on $\mathbb{H}$ with respect to the energy norm, we also have

$$|l(u_{\mathcal{F}}) - l(u_{\mathcal{E}_K})| \simeq \left|b\left(\Pi_{\mathcal{F}}^{\mathcal{R}_K} u_{\mathcal{F}}, \Pi_{\mathcal{F}}^{\mathcal{R}_K} v_{\mathcal{F}}\right)\right| \lesssim \left\|\Pi_{\mathcal{F}}^{\mathcal{R}_K} u_{\mathcal{F}}\right\|_e \left\|\Pi_{\mathcal{F}}^{\mathcal{R}_K} v_{\mathcal{F}}\right\|_e, \tag{3.30}$$

and we could also define the element-wise indicators based on the above equation. Notice that if we select l to be the source term in the adjoint problem defined by eq. (3.19), with eq. (3.30) we recover the element-wise indicators derived previously in eqs. (3.10) and (3.18). However, in the forthcoming numerical results, we employ the estimators based on eq. (3.29).

3.3.4. Error indicators using a pseudo-dual operator

The adjoint problem is often employed in the literature to guide GO refinements (see, e.g., [130, 156]). In addition, for the case of indefinite or non-symmetric problems, we further need to introduce an inner product (symmetric and positive definite form) to guide the refinements.

To overcome this issue, we first define $\Pi_{\mathcal{F}}^{\mathcal{E}_K} v_{\mathcal{F}}$ as a projection of the dual solution $v_{\mathcal{F}}$ into a given subset of *essential* basis functions $\mathcal{E}_K$. Such projections can be trivially implemented in the context of the multi-level data structures proposed in Zander et al. [207, 208, 210]; but not when using traditional data structures like those described in [62, 64, 65]. Then, we introduce a *pseudo-dual* bilinear form $\hat{b}$, in this case, defined by the 1D Laplace operator (although it is possible to select other symmetric positive definite bilinear forms) to solve the following residual-based *pseudo-dual* problem:

> Find $\tilde{\varepsilon}$ such that
>
> $$\hat{b}(\phi_{\mathcal{F}}, \tilde{\varepsilon}) = l(\phi_{\mathcal{F}}) - b\left(\phi_{\mathcal{F}}, \Pi_{\mathcal{F}}^{\mathcal{E}_K} v_{\mathcal{F}}\right), \quad \forall \phi \in \mathbb{H}. \tag{3.31}$$

In previous work, Romkes et al. [168] introduced an elliptic error representation. Later, Darrigrand et al. [60] utilized this concept in traditional data structures. However, their approach required dealing with two grids (fine and coarse) and PBI operators [62, 64, 66], which made implementation and mathematical analysis highly complex. In contrast, we define problem (3.31) using a simpler approach. We use the projection of $v_{\mathcal{F}}$ into $\mathcal{E}_K$, denoted as $\Pi_{\mathcal{F}}^{\mathcal{E}_K} v_{\mathcal{F}}$.

Thus, we define η_K as the error indicator associated with the element K as follows

$$\eta_K \coloneqq \left| \hat{b}\left(\Pi_{\mathcal{F}}^{\mathcal{R}_K} u_{\mathcal{F}}, \tilde{\varepsilon}\right) \right|, \quad \forall K \in \mathcal{T}, \tag{3.32}$$

i.e., we define the operator $a(\cdot,\cdot)$ simply as $a(\cdot,\cdot) = \hat{b}(\cdot,\cdot)$.

4. 1D Numerical results for Goal-Oriented h- and p-adaptivity

This chapter describes our h- and p-adaptive strategies tailored to address 1D problems governed by Helmholtz and convection-diffusion equations. These adaptive algorithms offer a distinctive approach, focusing on minimizing the error in a specific Quantity of Interest (QoI) rather than the global error. We will comprehensively describe our adaptive algorithms, elaborating on the error indicators utilized throughout this chapter. Our approach incorporates a *pseudo-dual* operator given by eq. (3.31), which proves advantageous for non-elliptic Goal-Oriented (GO) problems. The numerical results were published in Caro et al. [44].

The h- and p-adaptive algorithms proposed in this chapter follow the next refinement pattern: first, we perform a global and uniform h- or p-refinement (for the h- and p-adaptive versions, respectively). Then, we perform a coarsening step, removing some basis functions. This procedure is illustrated in Algorithm 1, and it was already introduced in [59] in the context of energy-norm adaptivity. The critical part is the coarsening step we depict in Algorithm 2. The critical step here is the computation of the element-wise error indicators described in section 3.3. In particular, we employ the eq. (3.32) to compute the error indicators utilized throughout this chapter.

To illustrate the performance of our adaptive strategies, we consider two problems governed by Helmholtz and convection-diffusion equations. We provide the evolution of the relative error in the QoI for h- and p-adaptivity and different values of the Partial Differential Equation (PDE) parameters. To define the relative error in the QoI, we compute $l(u)$ on a globally refined mesh. Then, we define the relative error in a QoI in percentage as follows:

$$e_{\text{rel}}^{\text{QoI}} := \frac{|l(u) - l(u_{\mathcal{T}_c})|}{|l(u)|} \cdot 100, \tag{4.1}$$

where u is the solution in a fine grid, while $u_{\mathcal{T}_c}$ is the solution associated with a coarser unrefined mesh. In some cases where the exact solution is available, we

will replace the fine grid solution u with the exact solution, and we will directly compute $e_{\text{rel}}^{\text{QoI}}$.

4.1. Helmholtz Goal-Oriented problem

Let us consider the following wave propagation problem:

> Find u such that,
>
> $$-u'' - k^2 u = \mathbb{1}_{\left(0,\frac{2}{5}\right)} \text{ in } (0,1)\,, \tag{4.2}$$
> $$u(0) = 0, \tag{4.3}$$
> $$u'(1) = 0. \tag{4.4}$$

We define the QoI as $l(u) = 5 \cdot \int_{\frac{3}{5}}^{\frac{4}{5}} u\,dx$. Figures 4.1 and 4.2 show the evolution of $e_{\text{rel}}^{\text{QoI}}$ by using h- and p-adaptivity, respectively. Note that the larger the number of Degrees of Freedom (nDoF) per wavelength, the faster $e_{\text{rel}}^{\text{QoI}}$ decreases. For example, in Figure 4.1, for $k = 7{\cdot}2\pi$, 10 Degrees of Freedom (DoF) per wavelength are sufficient to enter into the so-called asymptotic regime. In contrast, for $k = 28{\cdot}2\pi$, we need to consider at least 40 DoF per wavelength. In Figure 4.2, we select the initial mesh size such that the nDoF per wavelength is at least 3. This way, we satisfy the Nyquist rate. Both Figures 4.1 and 4.2 show optimal convergence rates in both h- and p-adaptivity. As a curiosity, we observe that the curves in Figure 4.1 are parallel, while the ones in Figure 4.2 coincide. That occurs due to dispersion (pollution) error, which quickly disappears with the p-method.

Figure 4.3 shows the solutions for the case $k = 7 \cdot 2\pi$. We also provide the corresponding h- and p-adaptive meshes. For the p-adaptive mesh, we show the mesh obtained in the 6th iteration, containing high approximation orders. To visualize the h-adaptive mesh, we display the mesh obtained in the 5th iteration. During this iteration, the refinements are denser in areas where the solution changes rapidly or exhibits sharp gradients. As a result, the element sizes in these regions are smaller than in other areas.

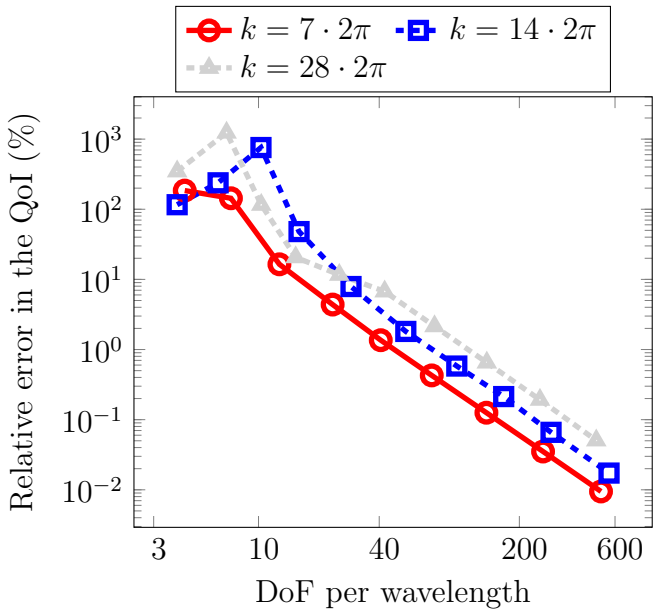

Figure 4.1.: Evolution of $e_{\text{rel}}^{\text{QoI}}$ using h-adaptivity. Initial mesh size $h = \frac{1}{30}$ and uniform $p = 1$.

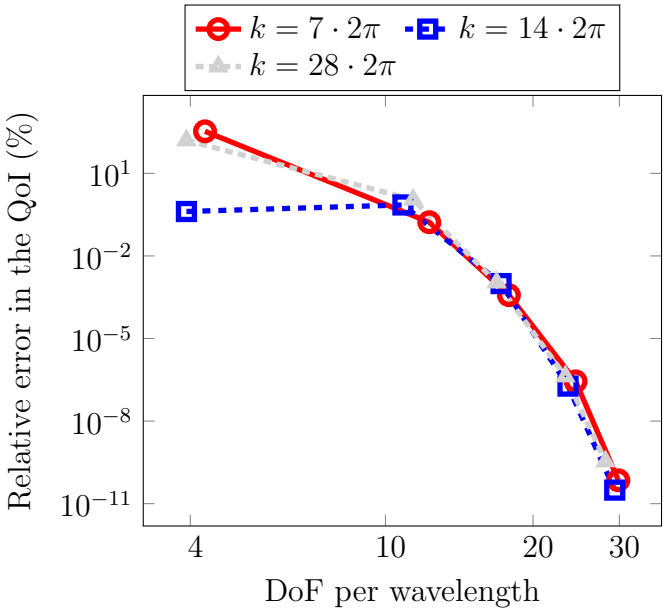

Figure 4.2.: Evolution of $e_{\text{rel}}^{\text{QoI}}$ using p-adaptivity. Uniform mesh size $h = \frac{1}{30}$.

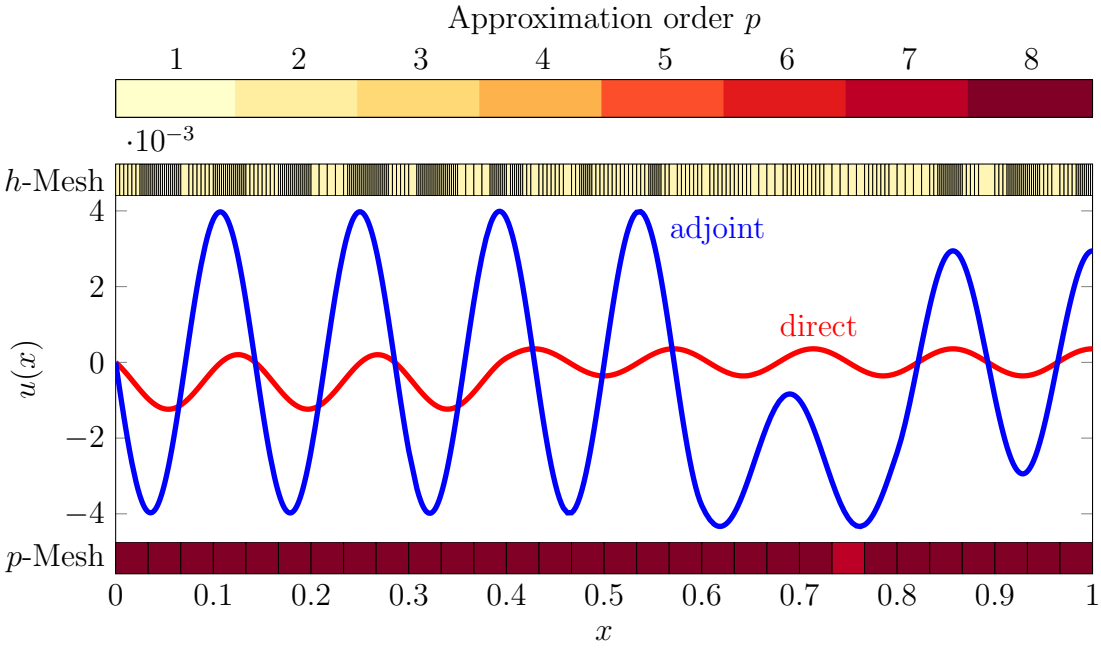

Figure 4.3.: Solutions with $k = 7 \cdot 2\pi$ problem after the h-adaptive process.

4.2. Convection-diffusion Goal-Oriented problem

Let us consider the boundary value problem associated with steady convective-diffusive transport:

> Find u such that,
>
> $$\begin{aligned} -\varepsilon u'' + \sigma \cdot u' &= \mathbb{1}_{(0,1)} \text{ in } (0,1)\,, \\ u(0) = u(1) &= 0, \end{aligned} \tag{4.5}$$

with $\sigma = 1$, and $0 < \varepsilon \ll 1$ the diffusive coefficient. We define the QoI as $l(u) = 5 \cdot \int_{\frac{4}{5}}^{1} \nabla u \, dx$.

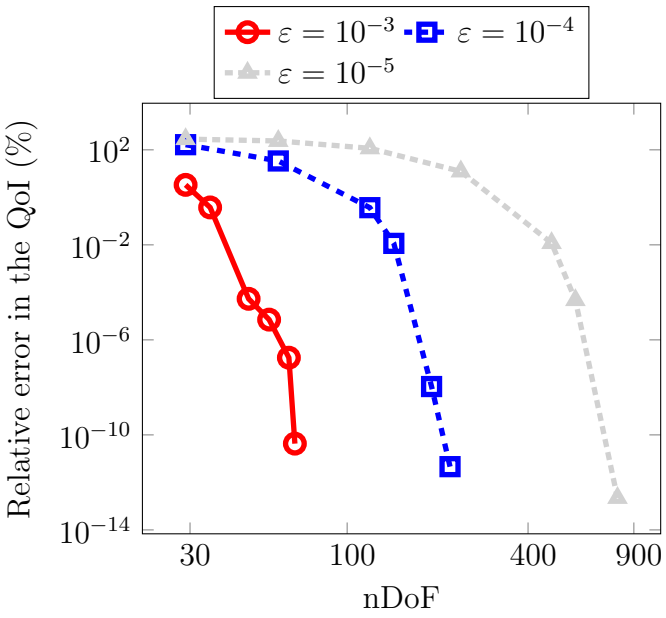

Figure 4.4.: Evolution of $e_{\text{rel}}^{\text{QoI}}$ using h-adaptivity. Initial mesh size $h = \frac{1}{30}$ and uniform $p = 1$.

We present the evolution of $e_{\text{rel}}^{\text{QoI}}$ with both h- and p-adaptivity in Figures 4.4 and 4.5, respectively. We achieve optimal convergence rates; but a smaller diffusive coefficient ε requires more nDoF to achieve these rates. To avoid potential rounding errors, we limit the order for p refinements not to exceed $p = 19$, as observed in Figure 4.5.

In the case $\varepsilon = 10^{-3}$, the solutions are displayed in Figure 4.6. We have also included the meshes and solutions corresponding to the 8th iteration for the h- and p-adaptive cases. We show the h-adaptive mesh obtained during the 8th

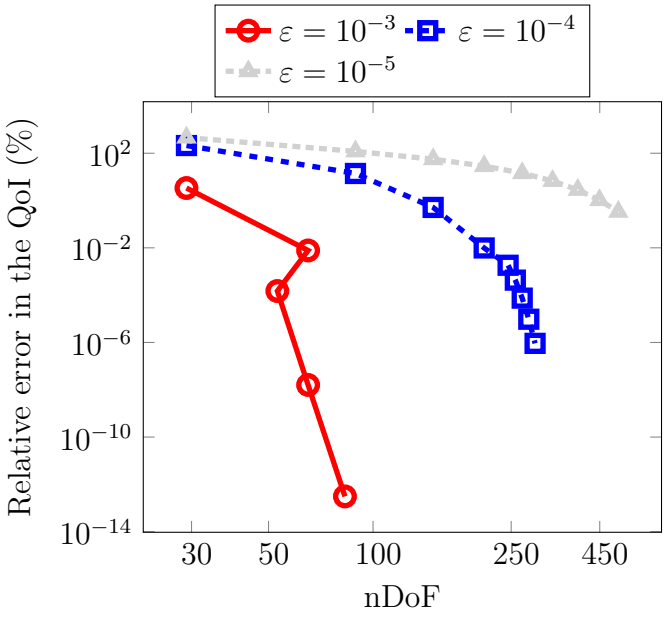

Figure 4.5.: Evolution of $e_{\text{rel}}^{\text{QoI}}$ using p-adaptivity. Uniform mesh size $h = \frac{1}{30}$.

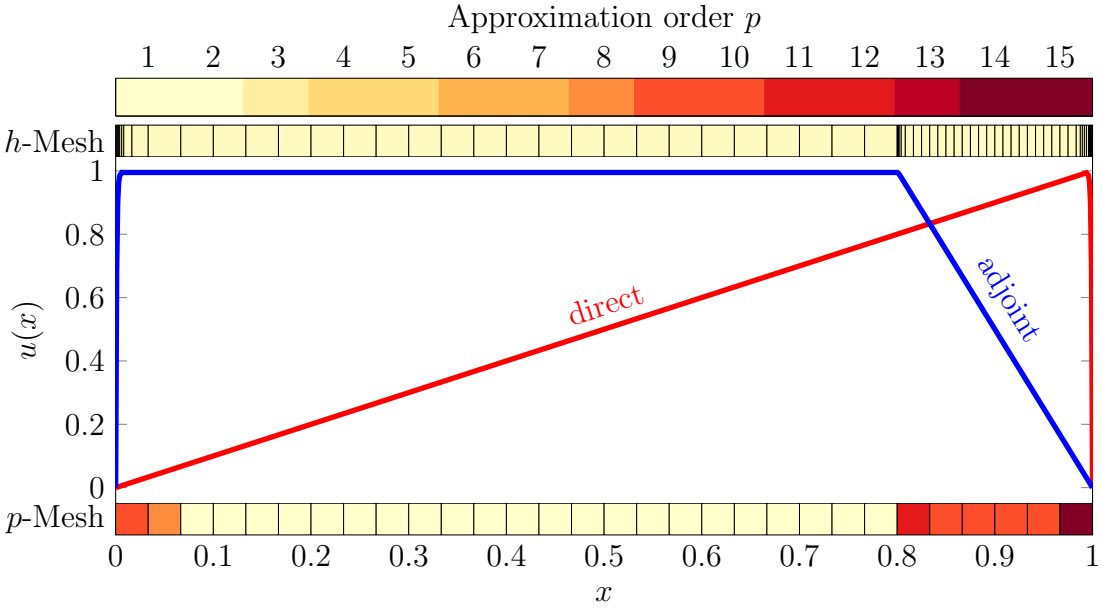

Figure 4.6.: Solutions with $\varepsilon = 10^{-3}$ problem after the h-adaptive process.

iteration for visualization purposes. In this iteration, refinements are denser in areas where the solution rapidly changes or sharp gradients exist. As a result, the element sizes in regions with boundary layers are smaller than in other areas,

while the polynomial orders p reach the value $p = 15$.

5. 2D Numerical results for hp-adaptivity

This chapter provides an overview of the performance of our hp-adaptive strategy for a wide range of problems. We solve 2D elliptic and non-elliptic problems based on Poisson, Helmholtz, and convection-diffusion equations exhibiting multiple singularities. For each example, we first display the results associated with the energy-norm adaptivity, followed by Goal-Oriented Adaptive (GOA) results. For all the experiments, we consider the Hilbert space $\mathbb{H} = \{u \in H^1(\Omega) \mid u = 0 \text{ on } \Gamma_D\}$, where Ω is the computational domain, and display the final adapted h- and hp-meshes and the convergence curves for hp-adaptivity and h-adaptivity with uniform $p = 1$ and $p = 2$. All the experiments start with a coarse mesh that is conforming to the materials and the source.

We refer to u as the solution in a fine grid, while $u_{\mathcal{T}_c}$ is the solution associated with a coarser unrefined mesh. In energy-norm adaptivity, we define the relative error in percentage as:

$$e_{\text{rel}}^{\text{energy}} := \frac{\|u - u_{\mathcal{T}_c}\|_{\mathbb{H}}}{\|u\|_{\mathbb{H}}} \cdot 100. \tag{5.1}$$

Our easy-to-implement approach only stores one grid at a time rather than maintaining several grids. Thus, we estimate the following lower bound of the error $e_{\text{rel}}^{\text{energy}}$ as follows:

$$\tilde{e}_{\text{rel}}^{\text{ energy}} := \frac{|\|u\|_{\mathbb{H}} - \|u_{\mathcal{T}_c}\|_{\mathbb{H}}|}{\|u\|_{\mathbb{H}}} \cdot 100 \leq e_{\text{rel}}^{\text{energy}}. \tag{5.2}$$

If the exact solution is available, we replace u with the exact solution to compute $e_{\text{rel}}^{\text{energy}}$ directly.

For the GOA problems, we define our Quantity of Interest (QoI) as

$$l(\phi) = \frac{1}{|\Omega_l|} \langle \mathbb{1}_{\Omega_l}, \phi \rangle_{L^2(\Omega)}, \ \forall \phi \in \mathbb{H}, \tag{5.3}$$

where $|\Omega_l|$ defines the area or volume of Ω_l and $\mathbb{1}_{\Omega_l}$ is a function equal to one if $x \in \Omega_l$, and zero otherwise. The subdomain Ω_l can be either a portion of the domain or a boundary region.

5.1. Singular Poisson example

We consider the following elliptic problem based on the Poisson equation.

> Find u such that
>
> $$-\Delta u = \mathbb{1}_{\Omega_f} \text{ in } \Omega, \tag{5.4}$$
> $$u = 0 \quad \text{on } \partial\Omega, \tag{5.5}$$

where $\Omega = \left((0,1) \times \left(\frac{1}{4}, \frac{3}{4}\right)\right) \cup \left(\left(\frac{1}{4}, \frac{3}{4}\right) \times (0,1)\right) \subset \mathbb{R}^2$ and $\Omega_f = \left(\frac{1}{4}, \frac{1}{2}\right)^2 \subset \Omega$. Following the definition of eq. (5.3) for the QoI, we select $\Omega_l = \left(\frac{1}{2}, \frac{3}{4}\right)^2 \subset \Omega$. Figure 5.1 shows the domain Ω of this elliptic problem. For elliptic problems in energy-norm adaptivity, we refer the interested reader to [59]. For Goal-Oriented (GO) adaptivity, Figures 5.2a and 5.2b show the solutions of the direct and adjoint problems, respectively.

We define the operators $b(\cdot,\cdot)$ and $a(\cdot,\cdot)$ associated with the above problem as follows:

$$b(\cdot,\cdot) \coloneqq \langle \nabla\cdot\,, \nabla\cdot \rangle_{L^2(\Omega)}\,, \tag{5.6}$$

and $a(\cdot,\cdot) = b(\cdot,\cdot)$.
Figure 5.3 shows the final h- and hp-adapted meshes and the evolution of $e_{\text{rel}}^{\text{QoI}}$. The first uniform mesh is composed of twelve root elements: given an initial 4×4 grid over a square domain, we have removed the four corner elements. The grid adapts to the four localized reentrant corners of the domain. The hp-adaptive strategy performs h-refinements near these singularities and p-refinement as we move away from them, as physically expected. We also observe heavy refinements around the central point of the domain. That is the only point where the right-hand sides of the direct and adjoint problems are discontinuous; therefore, solutions of the direct and adjoint problems simultaneously exhibit low regularity (only H^2). Consequently, some refinements there are expected. Convergence rates of the proposed hp-adaptive strategy are quasi-optimal (see Figure 5.3d).

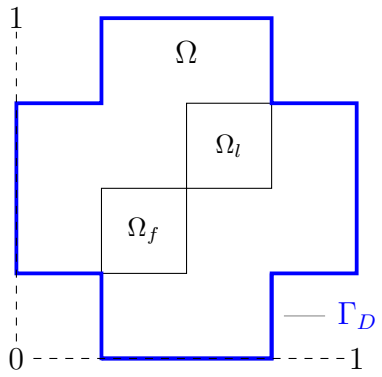

Figure 5.1.: Our singular Poisson example is defined over the domain Ω. The Dirichlet boundary is denoted by Γ_D. The source function is supported on Ω_f, and the QoI $l(\phi)$ is supported on Ω_l.

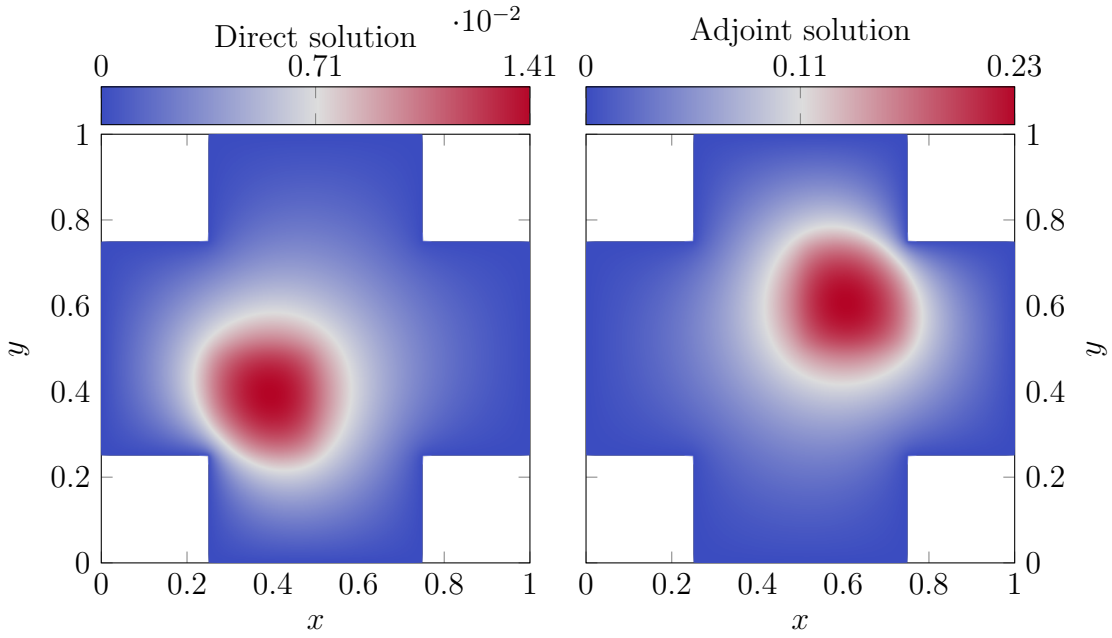

(a) Solution to the direct problem.

(b) Solution to the adjoint problem.

Figure 5.2.: Direct and adjoint solutions of our singular Poisson example.

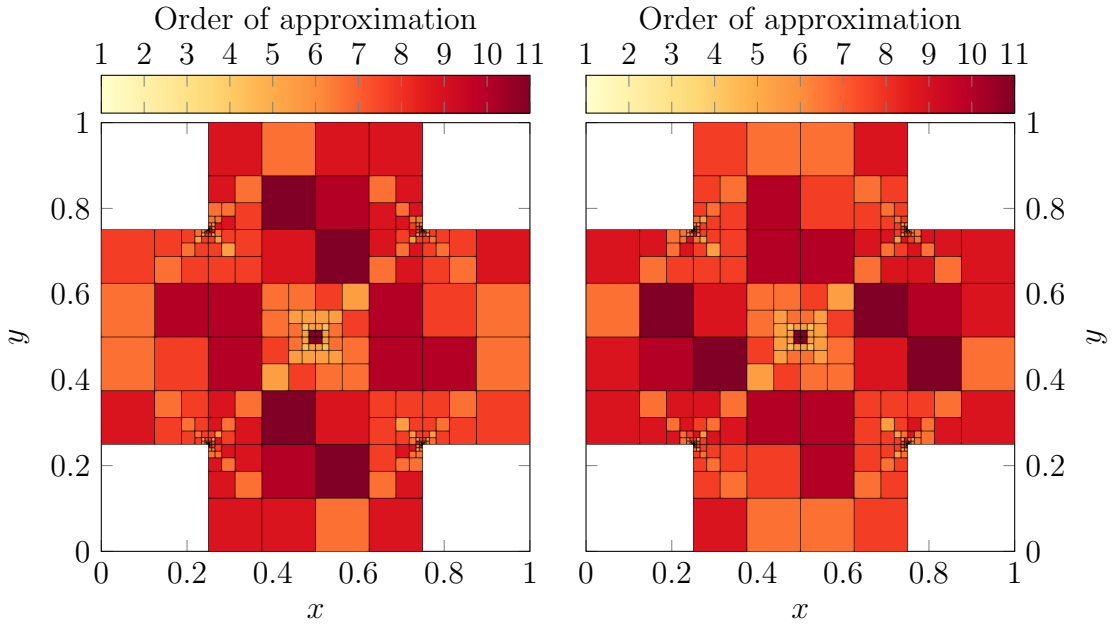

(a) Final *hp*-adapted mesh with polynomial orders in the x-direction.

(b) Final *hp*-adapted mesh with polynomial orders in the y-direction.

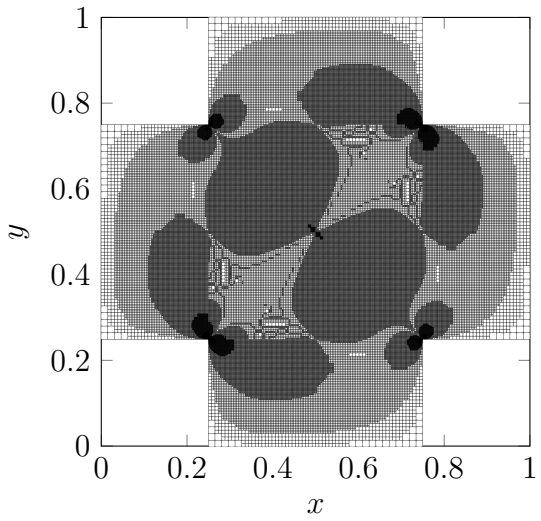

(c) Final h-adapted mesh, $p = 1$.

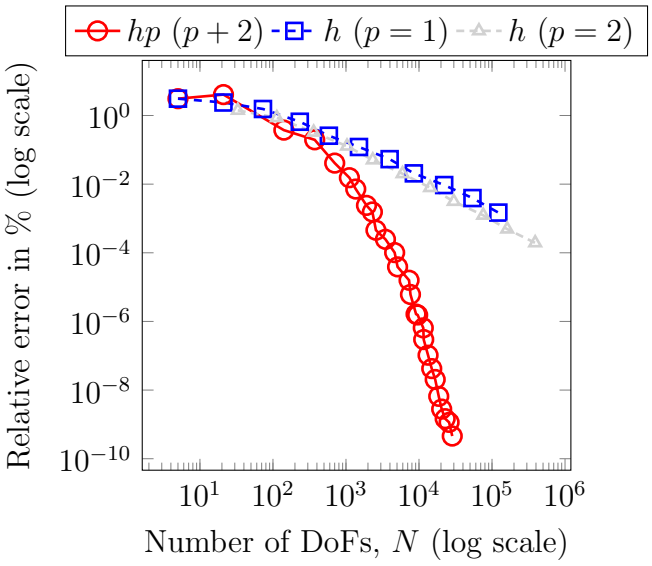

(d) Evolution of $e_{\text{rel}}^{\text{QoI}}$ in the process.

Figure 5.3.: Final h- and hp-adapted meshes for our singular Poisson example.

5.2. Wave propagation problem

We consider the following non-elliptic problem based on Helmholtz's equation.

Find u such that,

$$-\Delta u - k^2 u = \mathbb{1}_{\Omega_f} \text{ in } \Omega, \tag{5.7}$$
$$u = 0 \quad \text{on } \Gamma_D, \tag{5.8}$$
$$\nabla u \cdot \vec{n} = 0 \quad \text{on } \Gamma_N, \tag{5.9}$$

where $\Omega = (0,1)^2 \setminus \left(\frac{1}{4}, \frac{3}{4}\right)^2 \subset \mathbb{R}^2$, $\Omega_f = \left(0, \frac{1}{4}\right)^2 \subset \Omega$, and $k = (8 \cdot 2\pi, 2\pi)$. The complex-valued k indicates the medium is lossy. Γ_D and Γ_N stand for the parts of the boundary $\partial\Omega$ where we impose homogeneous Dirichlet and Neumann boundary conditions, respectively. From eq. (5.3), we define $\Omega_l = \left(\frac{3}{4}, 1\right)^2 \subset \Omega$. Figure 5.4 shows the domain of this hyperbolic (non-elliptic) problem.

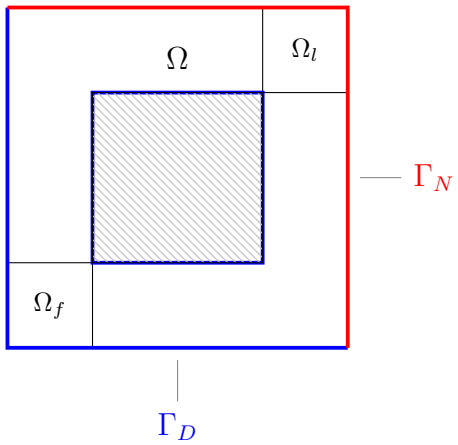

Figure 5.4.: Our wave propagation example is defined over the domain Ω with a hole in the middle (marked in gray). The Dirichlet boundary is denoted by Γ_D, while the Neumann boundary condition is denoted by Γ_N. The source function is supported on Ω_f, and the QoI $l(\phi)$ is supported on Ω_l.

5.2.1. Energy-norm adaptivity

For GO adaptivity, Figures 5.5a and 5.5b show the solutions to the direct and adjoint problems, respectively. Figure 5.6 shows the final h- and hp-adapted meshes and Figure 5.7 shows the evolution of $\tilde{e}_{\text{rel}}^{\text{energy}}$ and $e_{\text{rel}}^{\text{QoI}}$. The initial uniform

mesh is composed of twelve root elements. We perform a double h-hierarchical refinement on the initial mesh to obtain a fine mesh to start the adaptivity.

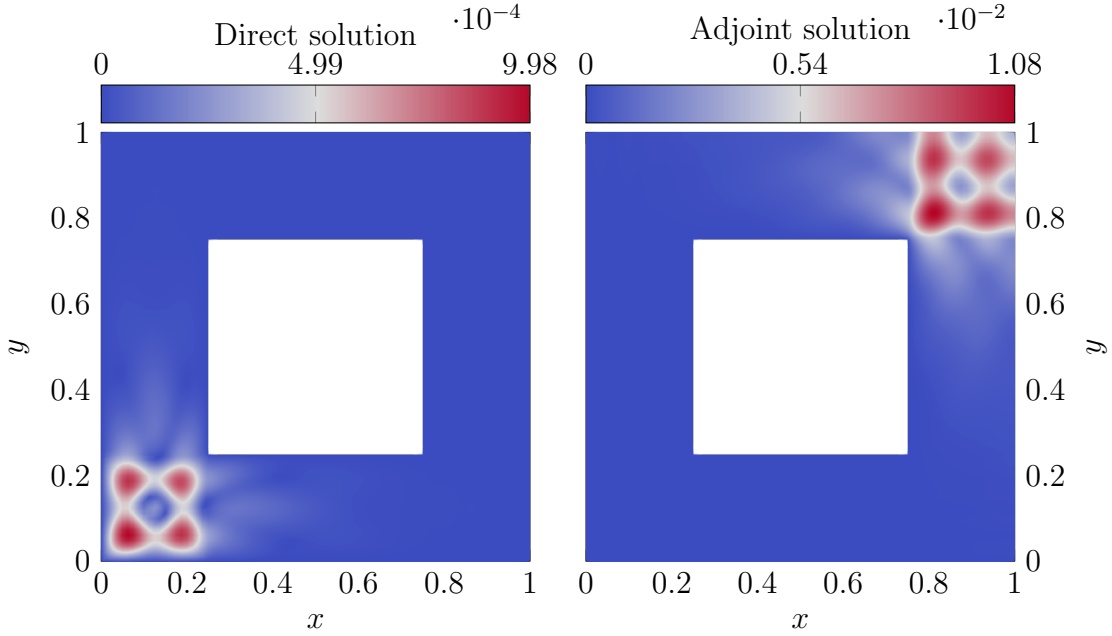

(a) Solution to the direct problem.

(b) Solution to the adjoint problem.

Figure 5.5.: Absolute value of the direct and adjoint solutions of our wave propagation example in a lossy medium.

For the h-adapted case, we observe heavy refinements around the source; however, almost no refinement occurs near the QoI. That happens due to the lossy nature of the problem. As a result, we observe a proper energy-norm convergence, as shown in Figure 5.7a, but a poor convergence behavior in the QoI, as demonstrated in Figure 5.7b.

When implementing the hp-adaptive strategy, the refinements tend to be denser around the source than in the vicinity of the QoI. However, some non-trivial refinements still occur around the QoI. Despite this, the relative error in the QoI, denoted as $e_{\text{rel}}^{\text{QoI}}$, still converges to a level of $10^{-3}\%$ with just 20k unknowns.

We define the operators $b(\cdot,\cdot)$ and $a(\cdot,\cdot)$ associated with the above problem as follows:

$$b(\cdot,\cdot) \coloneqq \langle \nabla\cdot\,, \nabla\cdot \rangle_{L^2(\Omega)} - k^2 \langle \cdot\,,\cdot \rangle_{L^2(\Omega)}\,, \quad a(\cdot,\cdot) \coloneqq \left| \langle \nabla\cdot\,, \nabla\cdot \rangle_{L^2(\Omega)} \right| + \left|k^2\right| \left| \langle \cdot\,,\cdot \rangle_{L^2(\Omega)} \right|. \tag{5.10}$$

Once more, $\|\cdot\|_e^2 = a(\cdot,\cdot)$ defines our energy norm and $|b(\phi,\psi)| \leq |a(\phi,\psi)|\,,\ \forall \phi,\psi \in \mathbb{H}$.

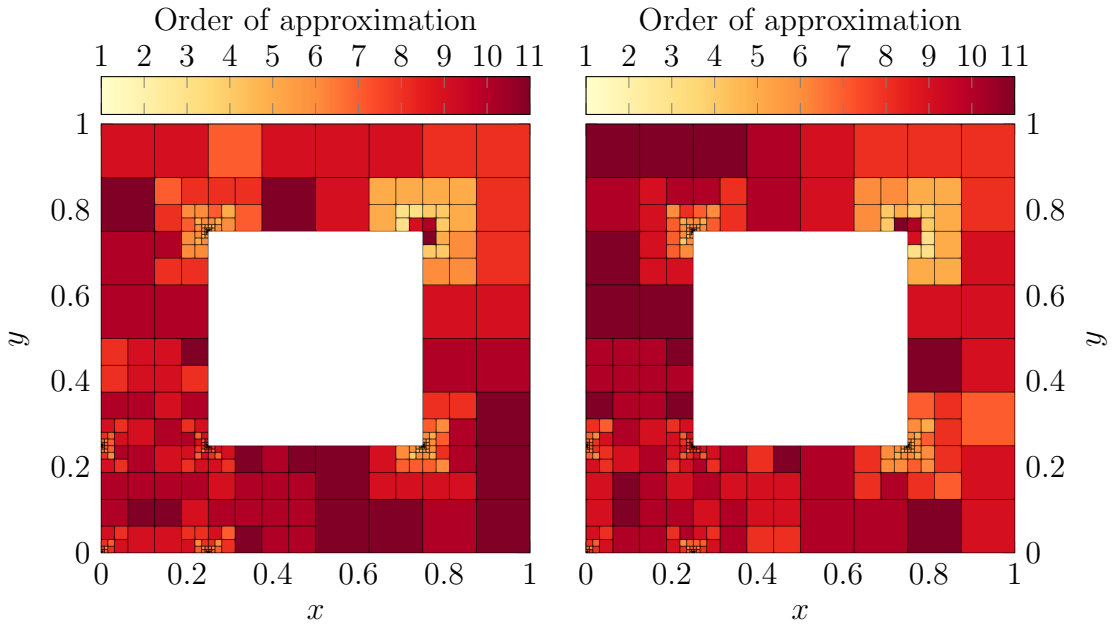

(a) Final *hp*-adapted mesh with polynomial orders in the x-direction.

(b) Final *hp*-adapted mesh with polynomial orders in the y-direction.

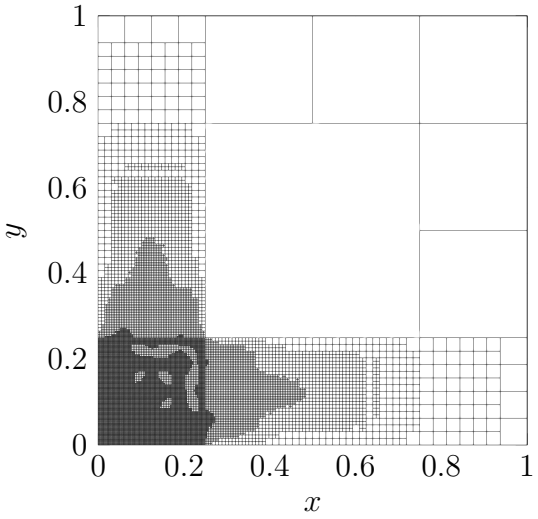

(c) Final h-adapted mesh, $p = 1$.

Figure 5.6.: Final h- and hp-adapted meshes for our wave propagation example in a lossy medium.

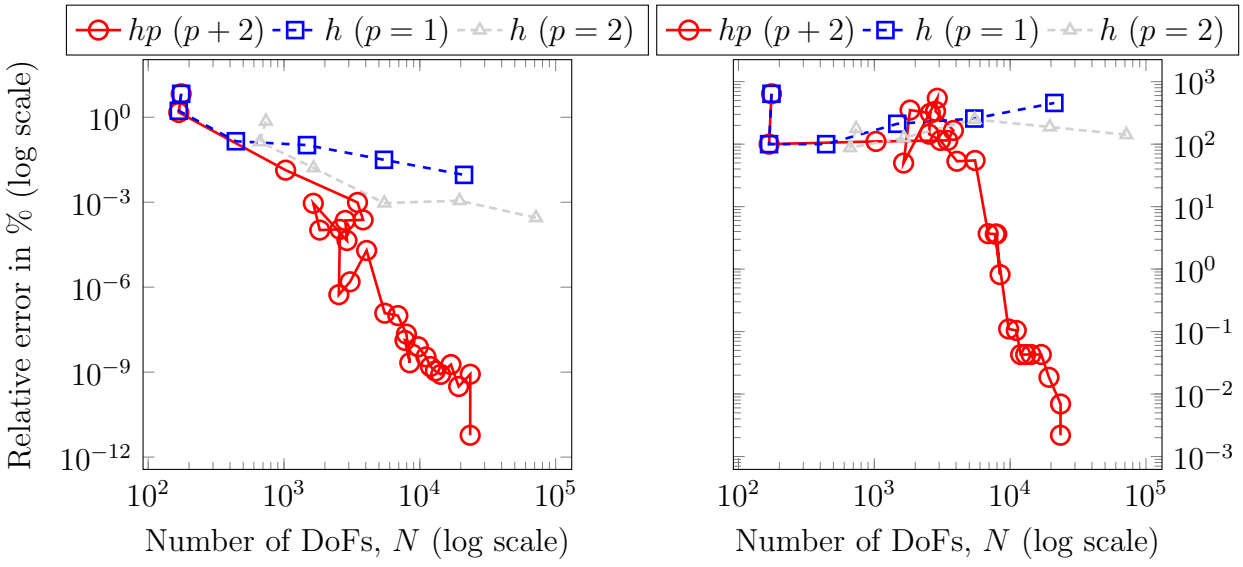

(a) Evolution of $\tilde{e}_{\text{rel}}^{\text{energy}}$ in the process.

(b) Evolution of $e_{\text{rel}}^{\text{QoI}}$ in the process.

Figure 5.7.: Energy-norm adaptivity. Evolution of $\tilde{e}_{\text{rel}}^{\text{energy}}$ and $e_{\text{rel}}^{\text{QoI}}$ in our wave propagation example in a lossy medium.

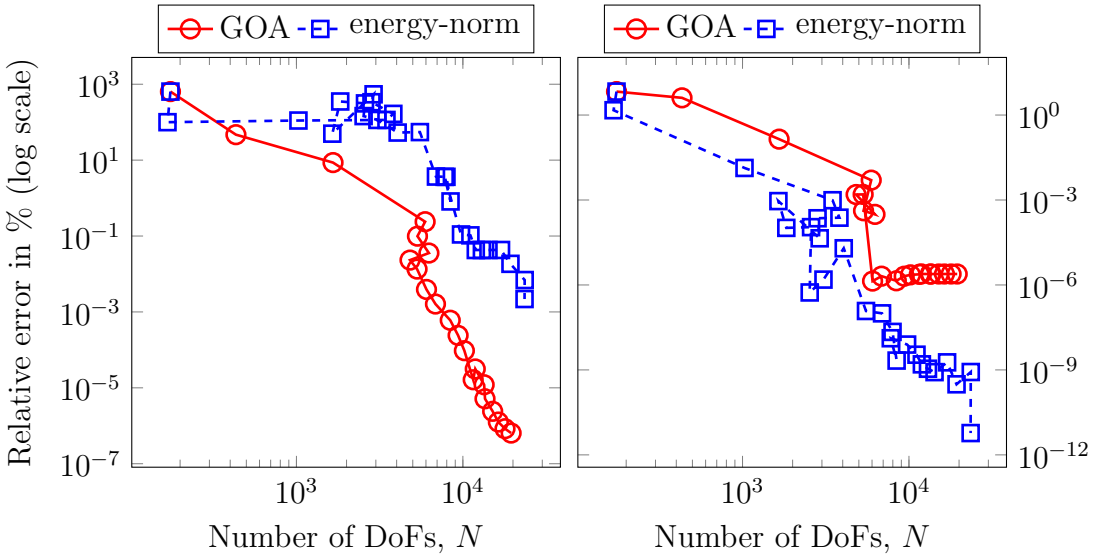

(a) Evolution of goal-oriented adaptivity.

(b) Evolution of energy-norm adaptivity.

Figure 5.8.: Convergence history of $e_{\text{rel}}^{\text{QoI}}$ and $\tilde{e}_{\text{rel}}^{\text{energy}}$ for the energy-norm and GO *hp*-adaptive strategies.

5.2.2. Goal-Oriented adaptivity

Figure 5.9 shows the final h- and hp-adapted meshes and the evolution of $e_{\text{rel}}^{\text{QoI}}$. The initial mesh is uniform and composed of twelve root elements. As in the energy-norm adaptivity, we perform a double h-hierarchical refinement on the initial mesh to obtain a fine mesh to start the adaptivity. We observe heavy h-refinements around four localized singularities at the interior corners of the domain. In addition, we recover exponential convergence rates for the h- and for the hp-adaptive versions. As a result, we construct a hp-adapted mesh with 20k unknowns that delivers a relative error in the QoI of $10^{-6}\%$ (three orders of magnitude better than in Figure 5.7b).

To better illustrate this idea, Figure 5.8 compares the evolution of $e_{\text{rel}}^{\text{QoI}}$ and $\tilde{e}_{\text{rel}}^{\text{energy}}$ when executing the energy-norm and the GO hp-adaptive strategies in our wave propagation example in a lossy medium. Figure 6.4a shows a relative error in the QoI three orders of magnitude better when performing GO adaptivity than considering energy-norm adaptivity. Figure 6.4b shows that the $\tilde{e}_{\text{rel}}^{\text{energy}}$ rapidly converges when employing energy-norm adaptivity, while with the hp-adaptive GO strategy, the rapid initial convergence stagnates at the level of $10^{-6}\%$. As expected, this situation is also noticeable in terms of h-adaptivity (see Figures 5.7 and 5.9d).

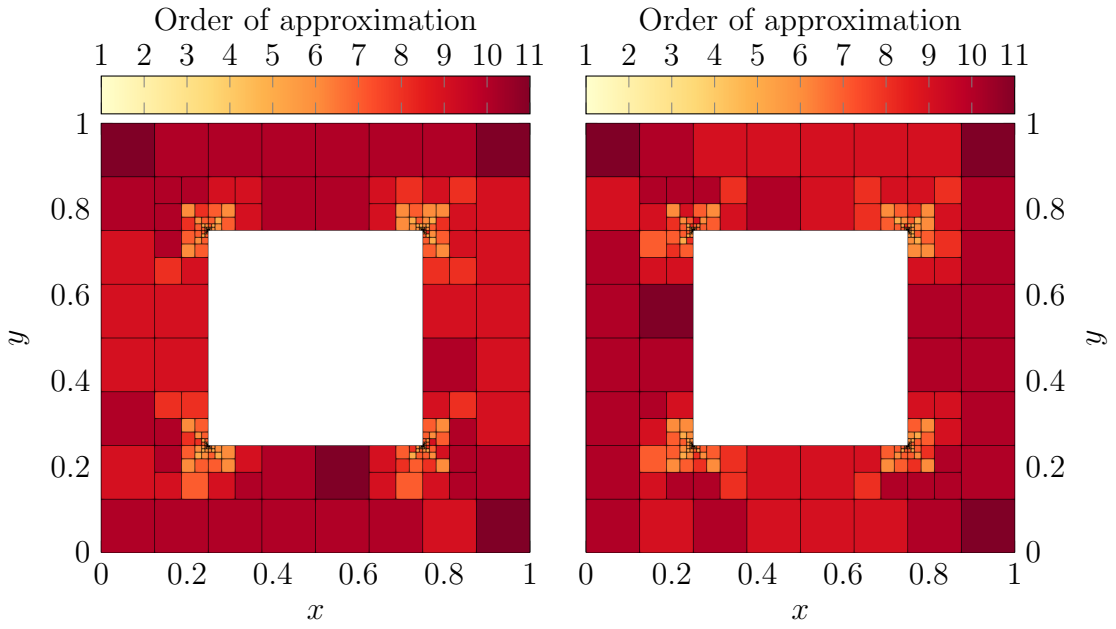

(a) Final *hp*-adapted mesh with polynomial orders in the x-direction.

(b) Final *hp*-adapted mesh with polynomial orders in the y-direction.

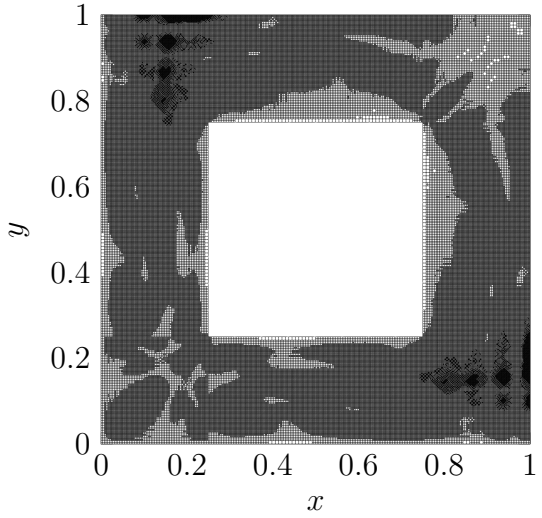

(c) Final h-adapted mesh, $p = 1$.

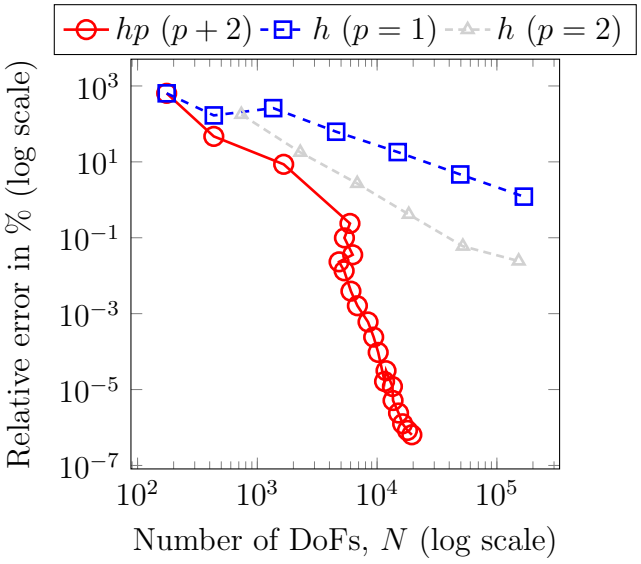

(d) Evolution of $e_{\text{rel}}^{\text{QoI}}$ in the process.

Figure 5.9.: Final h- and hp-adapted meshes for our singular GO wave propagation example in a lossy medium and the evolution of $e_{\text{rel}}^{\text{QoI}}$.

5.3. Convection-dominated diffusion problem

5.3.1. Convection-dominated diffusion: example 1

We consider the following non-elliptic problem based on the convection-dominated diffusion equation.

> Find u such that,
>
> $$-\varepsilon\Delta u + \sigma \cdot \nabla u = f \text{ in } \Omega, \qquad u = 0 \text{ on } \partial\Omega. \tag{5.11}$$

The selection of a suitable norm to measure the error in problems based on eq. (5.11) is an open research subject. For instance, authors of [77, 78] use the standard energy norm, in [79] a balanced norm, and in [180, 199] different norms from the previous ones. In here, we define the operators $b(\cdot,\cdot)$ and $a(\cdot,\cdot)$ associated with the above problem as follows:

$$b(\cdot,\cdot) \coloneqq \varepsilon \langle \nabla\cdot, \nabla\cdot \rangle_{L^2(\Omega)} + \langle \sigma\nabla\cdot, \cdot \rangle_{L^2(\Omega)}, \quad a(\cdot,\cdot) \coloneqq (\varepsilon + C) \langle \nabla\cdot, \nabla\cdot \rangle_{L^2(\Omega)}, \tag{5.12}$$

where $\|\cdot\|_e^2 = a(\cdot,\cdot)$ is our energy norm and $C \in \mathbb{R}^+$. We select this definition of $a(\cdot,\cdot)$ by bounding from above the convective term of $b(\cdot,\cdot)$ using a mesh-independent constant C for the Poincaré inequality that also includes the effect of σ [1] [2].

5.3.1.1. Energy-norm adaptivity

For this example, we consider $\varepsilon = 10^{-3}$ as the diffusive coefficient, $\sigma = (3,1)^{\mathrm{T}}$, and $\Omega = (0,1)^2$. The load function f is a linear continuos form on $\mathbb{H}$ and it is selected so that the solution u is of the form:

$$u(x,y) = e^{\frac{\varepsilon}{x(x-1)}} \cosh\Big(500\big(\frac{1}{2} + \sigma^{-1}(x,-y)\big)\Big)^{-2}. \tag{5.13}$$

Figure 5.10 shows the solution of this convection-dominated diffusion example. The initial uniform mesh is composed of thirty-six root elements. Figure 5.11

[1] It is essential to consider a mesh-independent norm $a(\cdot,\cdot)^{1/2}$ since we approximate some errors by computing the difference of the norm of two approximated solutions evaluated on *different* grids.

[2] The actual value of the constant C is unneeded in practice since we compute relative error indicators; in our case, we select $(C + \varepsilon) = 1$.

shows the final energy-norm h- and hp-adapted meshes and the evolution of e_{rel}. As expected, we observe heavy h-refinements around the line that characterizes the solution. In the hp-adapted case, we also observe an increase in the polynomial order in some of the elements near this characteristic line. We also observe exponential convergence rates (see Figure 5.11d).

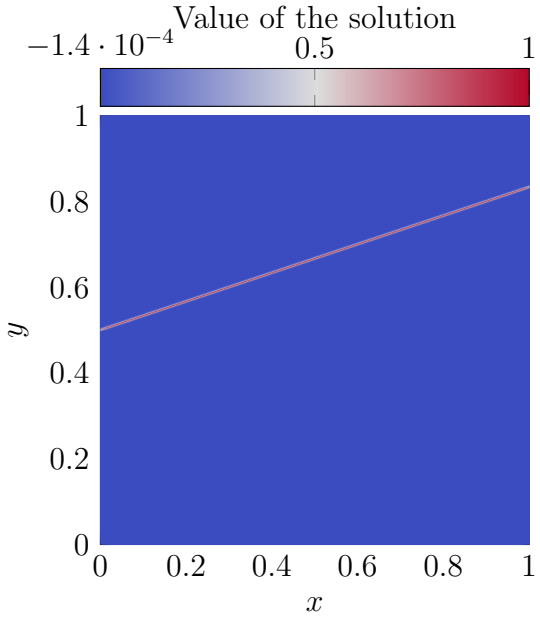

Figure 5.10.: Solution of the convection-dominated diffusion example 1.

5.3.2. Convection-dominated diffusion: example 2

We now consider a more challenging setting with advection skew to the mesh. We solve a similar problem to the one depicted in Figure 9.3 of [55] (see Figure 5.12). Our convection-dominated diffusion problem is governed by eq. (5.11) on the domain $\Omega = (0,1)^2$, with $\varepsilon = 10^{-4}$, $\sigma = (\cos\theta, \sin\theta)^{\mathrm{T}}$, $\theta = \arctan(2)$, and zero Dirichlet boundary conditions, as depicted in Figure 5.12a.

We define our source term f (with support in Ω_f and illustrated in Figure 5.12b)

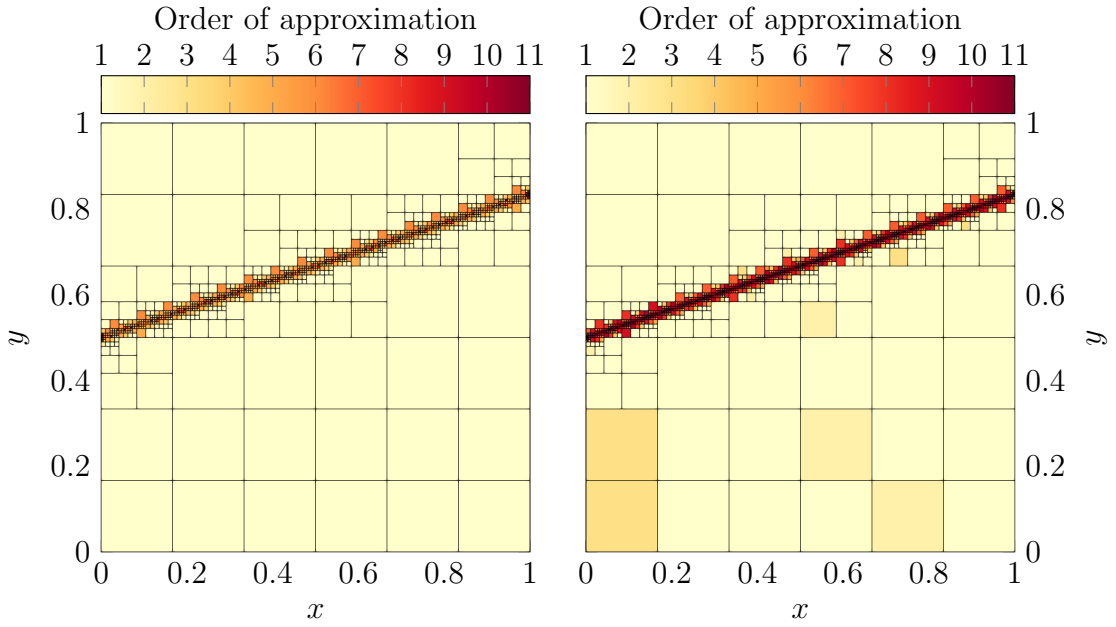

(a) Final *hp*-adapted mesh with polynomial orders in the x-direction.

(b) Final *hp*-adapted mesh with polynomial orders in the y-direction.

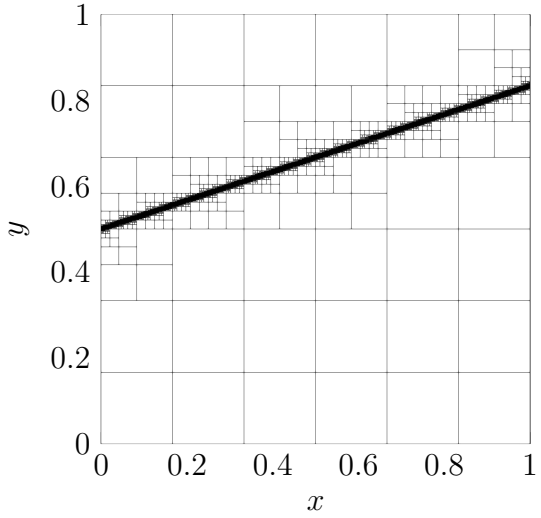

(c) Final *h*-adapted mesh, $p = 1$.

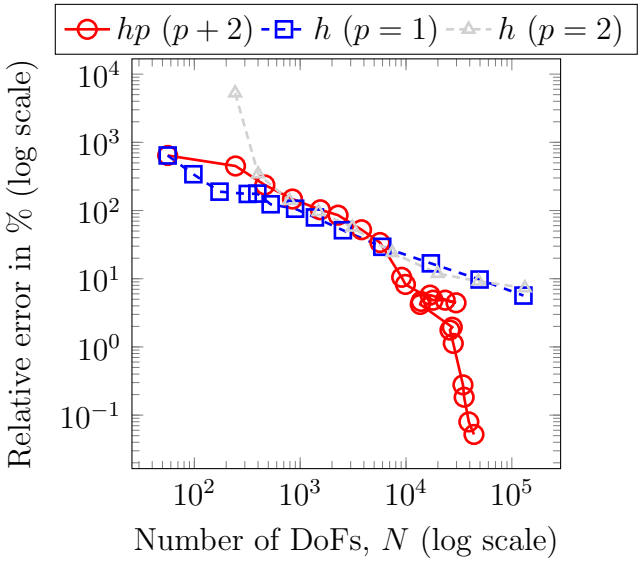

(d) Evolution of $e_{\text{rel}}^{\text{energy}}$ in the process.

Figure 5.11.: Final *h*- and *hp*-adapted meshes for our first convection-dominated diffusion example and the evolution of $e_{\text{rel}}^{\text{energy}}$.

as:

$$f(x,y) = \begin{cases} (1-4x)^2, & \text{if } 0 \le x \le 0.25, \quad 0.25 \le y \le 0.5, \\ (1-4y)^2, & \text{if } 0.25 \le x \le 1, \quad 0 \le y \le 0.25, \\ 1 + 16xy\,(-3+4x+4y), & \text{if } 0 \le x \le 0.25, \quad 0 \le y \le 0.25, \\ 0, & \text{otherwise.} \end{cases} \tag{5.14}$$

Both the problem of Figure 9.3 of [55] and our problem share a strong boundary layer along the top and right boundaries of the domain. In addition, our problem incorporates (a) a source discontinuity on the edge $0 \le x \le 0.25, y = 0.5$ that is visible in Figure 5.12b, and (b) a strong boundary layer for the adjoint problem along the bottom border of the domain. Thus, our example exhibits strong gradients of different (unknown) intensities in various areas of the domain, which makes it ideal for assessing the performance of our proposed *hp*-adaptive algorithm. The initial uniform mesh consists of 4×4 root elements for both adaptive strategies.

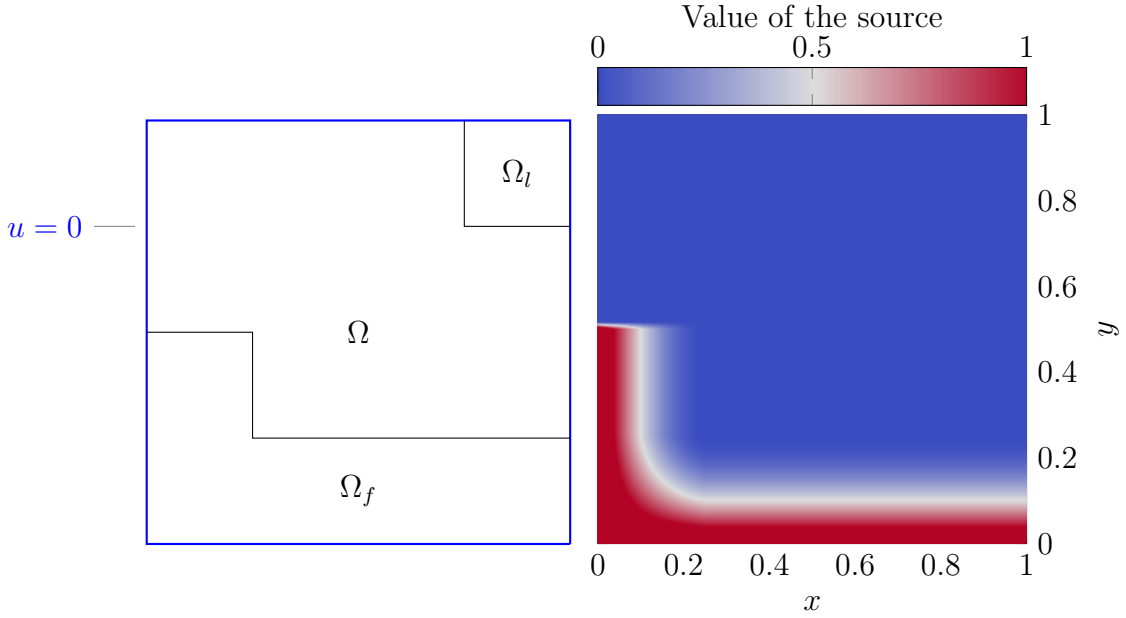

(a) Problem setting.

(b) Illustration of f in eq. (5.11).

Figure 5.12.: Problem description for our second convection-dominated diffusion with advection skew to the mesh.

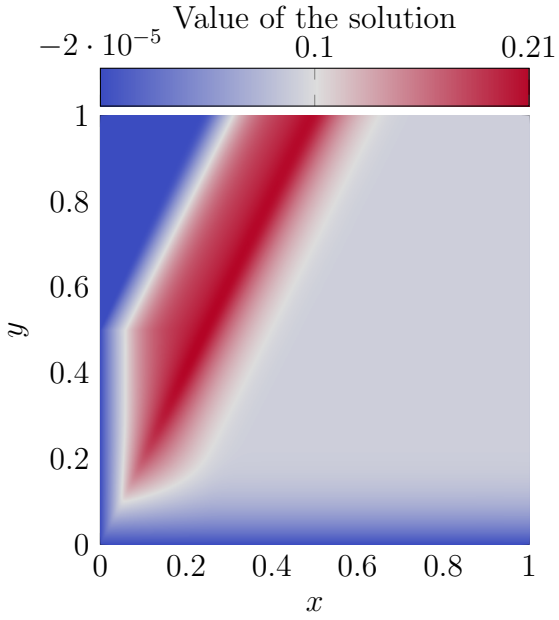

Figure 5.13.: Numerical solution of the convection-dominated diffusion example 2 for energy-norm adaptivity.

5.3.2.1. Energy-norm adaptivity

Figure 5.13 displays the final solution of the convection-dominated diffusion example 2 for the energy-norm adaptivity. Figure 5.14 shows the final energy-norm h- and hp-adapted meshes and the evolution of the relative error when using energy-norm adaptivity. As expected, h and hp meshes exhibit strong h-refinements towards the two boundary layers on the top and right sides of the domain. In addition, the hp-adaptivity is also able to capture both the advection propagation direction and the source discontinuity.

Figures 5.15 and 5.16 illustrate the evolution of the energy-based adaptive process by displaying at different iterations several solutions to the problem (left panels) and their corresponding hp-adaptive meshes (right panels). These meshes only display the polynomial orders in the x-direction, but analogous results are obtained for the y-direction. We accentuate the capability of the proposed algorithm to eliminate Degrees of Freedom (DoF) previously introduced during the pre-asymptotic regime due to spurious oscillations. For instance, at iteration 7 (Figure 5.15b), high polynomial orders p are set on the center-right part of the domain to capture the numerical artifacts exhibited by the solution (Figure 5.15a). Once we better solve the problem, the numerical pollution starts to vanish (Figure 5.15c), and consequently, some previously introduced high-order elements are

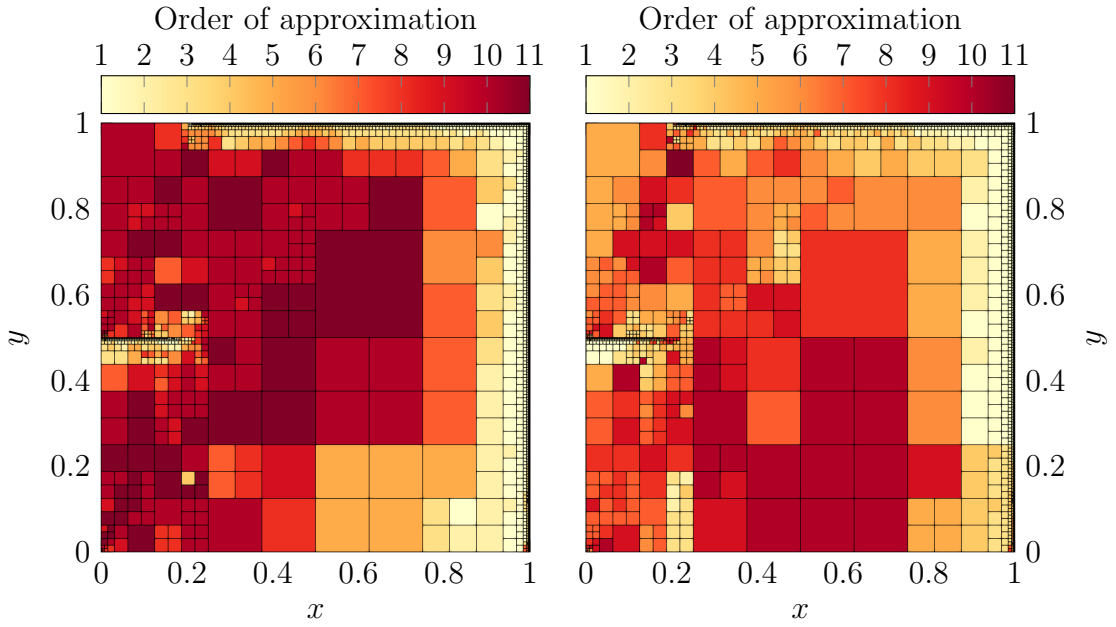

(a) Final *hp*-adapted mesh with polynomial orders in the x-direction.

(b) Final *hp*-adapted mesh with polynomial orders in the y-direction.

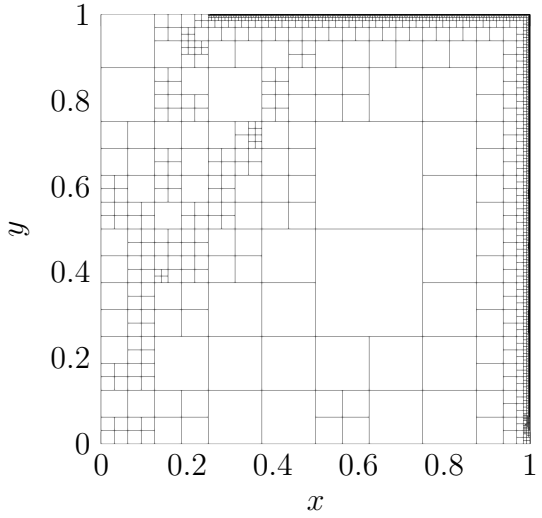

(c) Final h-adapted mesh, $p = 1$.

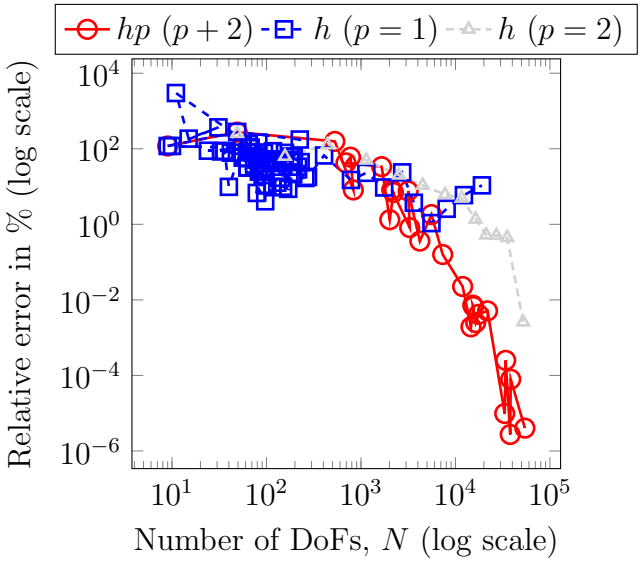

(d) Evolution of $\tilde{e}_{\text{rel}}^{\text{energy}}$ in the process.

Figure 5.14.: Final h- and hp-adapted meshes for our second convection-dominated diffusion example and the evolution of $\tilde{e}_{\text{rel}}^{\text{energy}}$.

p-unrefined (see Figure 5.15d) on the elements near the center of the domain and close to the right boundary layer.

We also highlight the gradual behavior of the adaptive process: at the beginning, the refinements are mostly introduced to capture the boundary layers (Figure 5.15d). Once the boundary layers are properly resolved (Figure 5.16b), the algorithm refines to catch better the direction of propagation of the convection part of the problem. The adaptive process is almost finished at this point, and the error is of the order of $10^{-4}\%$. The final refinements are devoted to improving the solution nearby the source discontinuity, and accordingly, we begin to observe more refinements towards this region (see Figure 5.16d). The final meshes (iteration 27) correspond to Figures 5.14a and 5.14b.

5.3.2.2. Goal-Oriented adaptivity

We select the domain of the QoI (illustrated in Figure 5.12a) to be $\Omega_l = \left(\frac{3}{4}, 1\right)^2 \subset \Omega$. Figure 5.17 displays the solutions to the forward and adjoint problems associated with the second example. As expected, we observe (a) higher resolution at the QoI —upper-right part of the domain—, and (b) spurious numerical oscillations in the forward problem far from the region of interest where the QoI is defined (compared to the energy-norm solution depicted in Figure 5.13).

Figure 5.18 displays the final h- and hp-adapted meshes and the evolution of $e_{\text{rel}}^{\text{QoI}}$. In contrast to the energy-norm adaptivity, where the refinements were more oriented towards the top and right boundary, here, the adjoint problem (Figure 5.17b) highly drives the refinements for both h- and hp-strategies, and hence, we observe further refinements on the boundary layers of the adjoint problem.

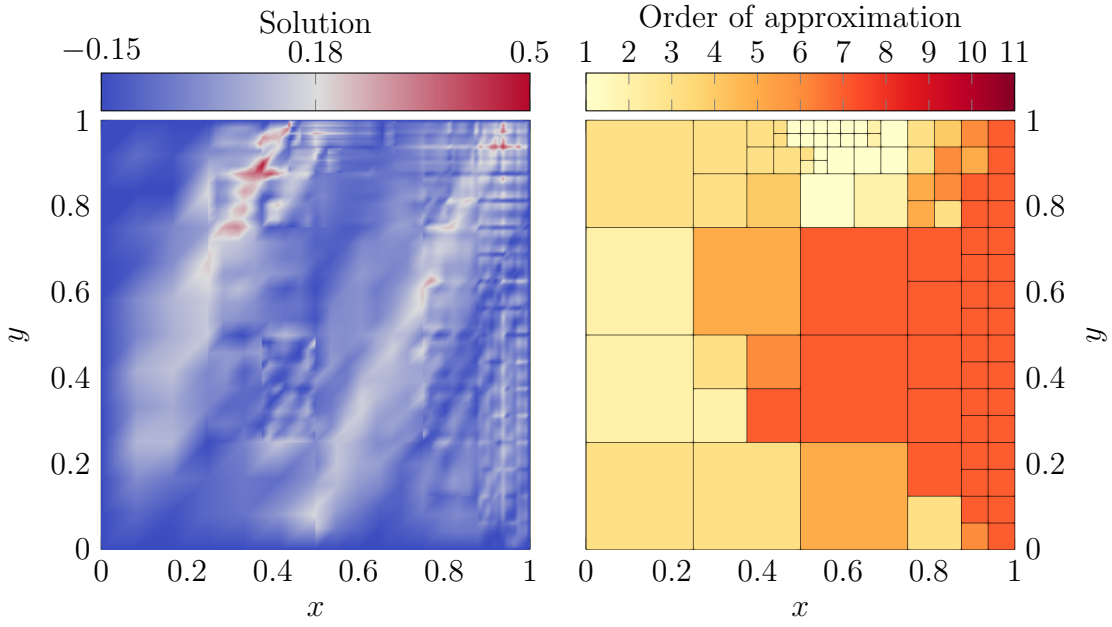

(a) Solution at iteration 7.

(b) *hp*-adapted mesh at iteration 7.

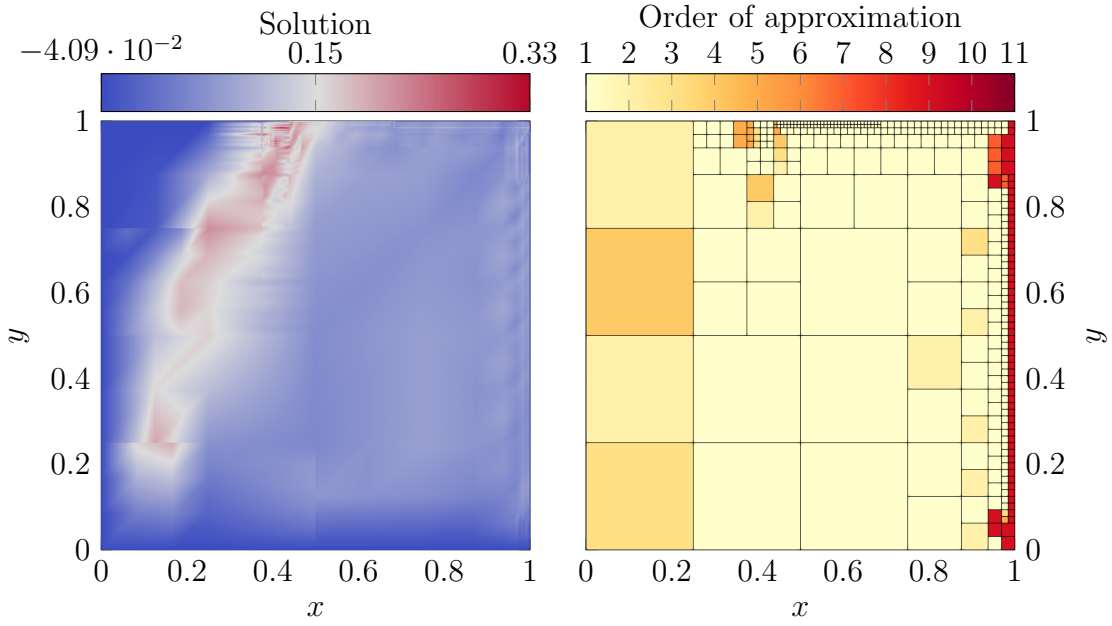

(c) Solution at iteration 10.

(d) *hp*-adapted mesh at iteration 10.

Figure 5.15.: Numerical solutions and *hp*-adapted meshes (polynomial orders in the x-direction) at iterations 7 and 10.

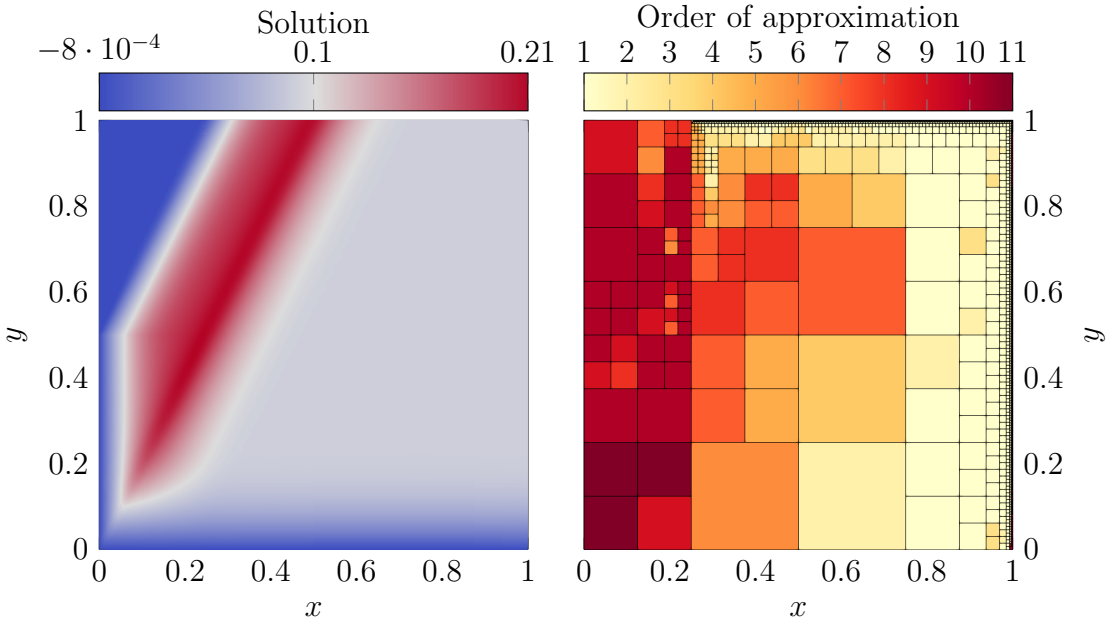

(a) Solution at iteration 17.

(b) *hp*-adapted mesh at iteration 17.

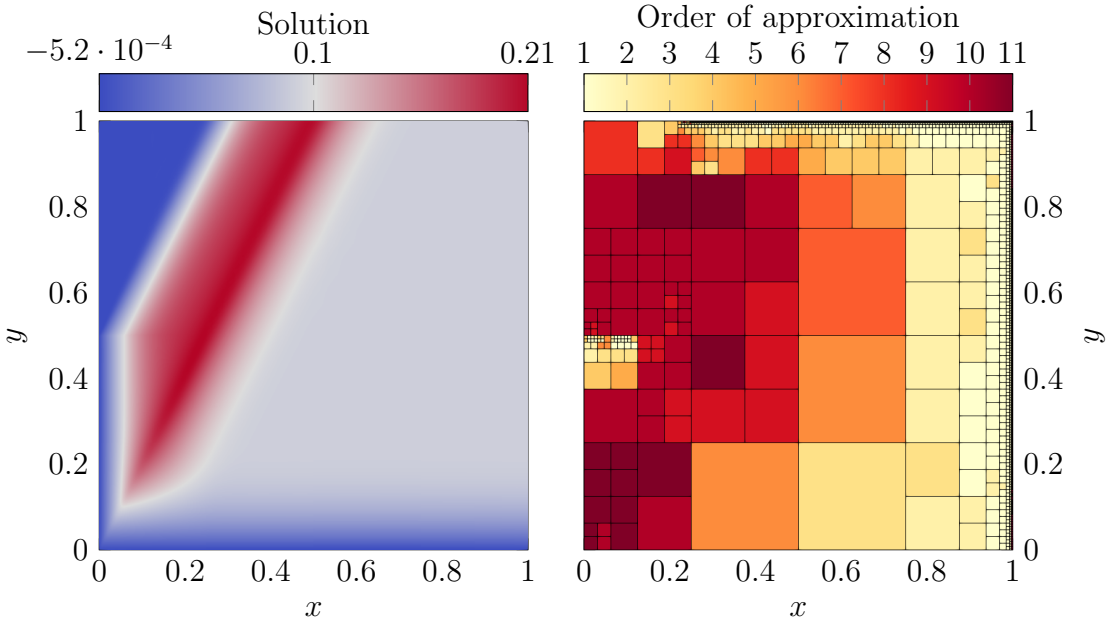

(c) Solution at iteration 21.

(d) *hp*-adapted mesh at iteration 21.

Figure 5.16.: Numerical solutions and *hp*-adapted meshes (polynomial orders in the x-direction) at iterations 17 and 21.

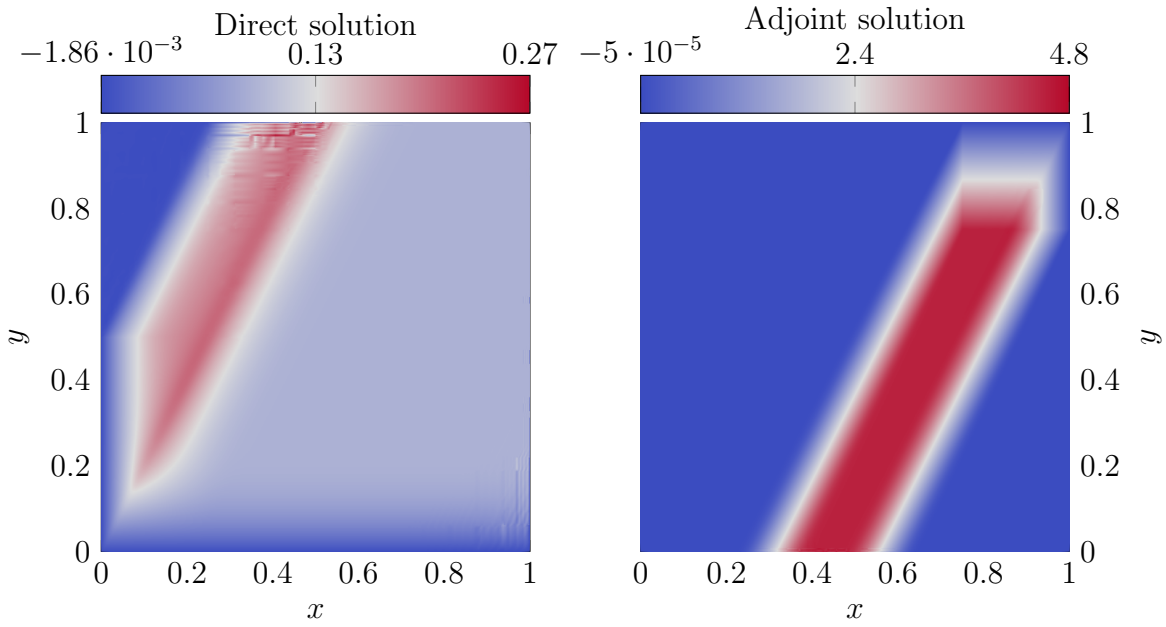

(a) Solution to the direct problem.

(b) Solution to the adjoint problem.

Figure 5.17.: Direct and adjoint numerical solutions of the convection-dominated diffusion problem for GO adaptivity.

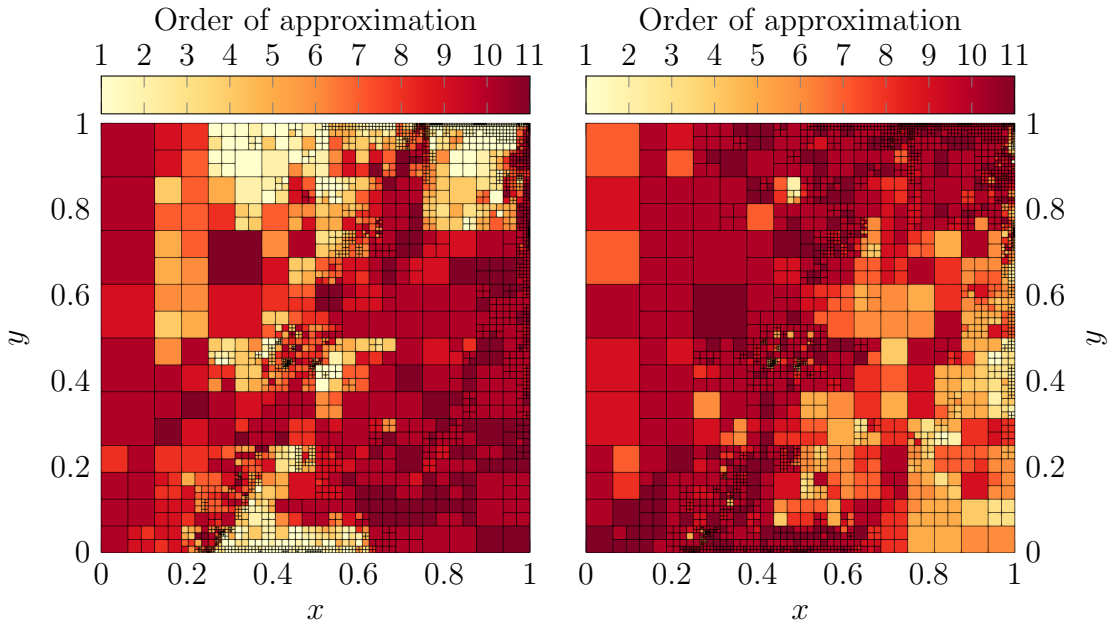

(a) Final *hp*-adapted mesh with polynomial orders in the x-direction.

(b) Final *hp*-adapted mesh with polynomial orders in the y-direction.

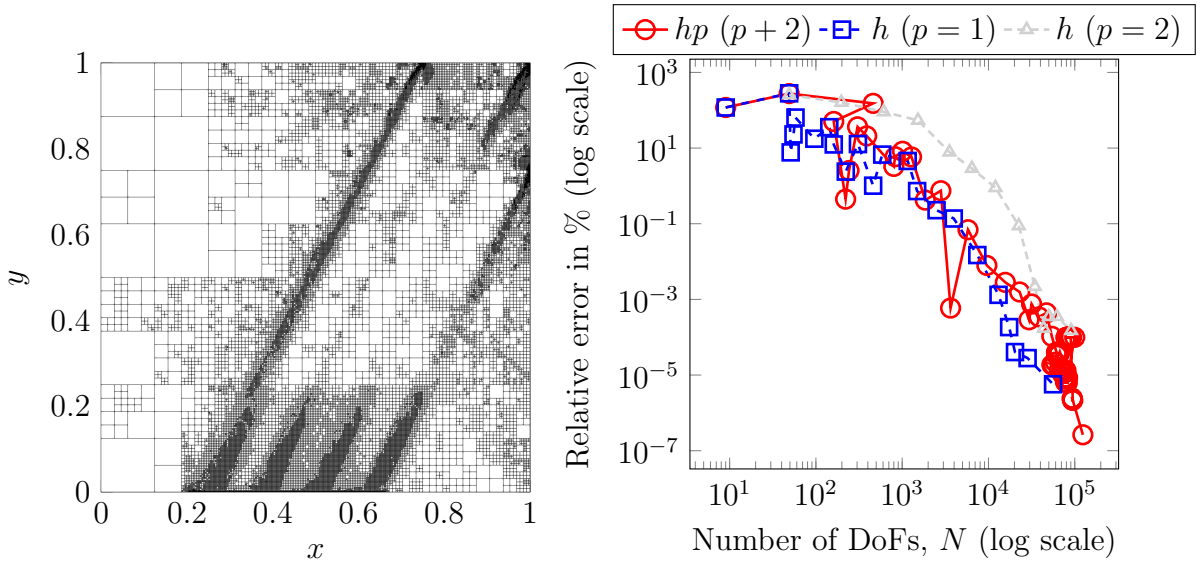

(c) Final h-adapted mesh, $p = 1$.

(d) Evolution of $e_{\text{rel}}^{\text{QoI}}$ in the process.

Figure 5.18.: Final h- and hp-adapted meshes for our second convection-dominated diffusion example and the evolution of $e_{\text{rel}}^{\text{QoI}}$.

6. 3D Numerical results for hp-adaptivity

6.1. Wave propagation problem

Let us consider the following non-elliptic problem based on heterogeneous Helmholtz's equation.

> Find u such that,
>
> $$-\nabla \cdot (\sigma \nabla u) - k^2 u = \mathbb{1}_{\Omega_f} \text{ in } \Omega, \tag{6.1}$$
> $$u = 0 \quad \text{on } \Gamma_D, \tag{6.2}$$
> $$\nabla u \cdot \vec{n} = 0 \quad \text{on } \Gamma_N, \tag{6.3}$$

where $\Omega = (0,1)^3 \subset \mathbb{R}^3$, $\Omega_f = \left(0, \frac{1}{4}\right)^3 \subset \Omega$, and $k = (4 \cdot 2\pi, 2\pi)$. Γ_D and Γ_N stand for the parts of the boundary $\partial\Omega$ where we impose homogeneous Dirichlet and Neumann boundary conditions, respectively. We impose Dirichlet boundary conditions on the 3 faces whose intersection is $(0,0,0)$ and Neumann boundary on the 3 faces whose intersection is $(1,1,1)$.

$$\Gamma_D \coloneqq ([0,1] \times [0,1] \times \{0\}) \cup ([0,1] \times \{0\} \times [0,1]) \cup (\{0\} \times [0,1] \times [0,1]), \tag{6.4}$$
$$\Gamma_N \coloneqq ((0,1) \times (0,1) \times \{1\}) \cup ((0,1) \times \{1\} \times (0,1)) \cup (\{1\} \times (0,1) \times (0,1)). \tag{6.5}$$

Here,

$$\sigma(x) = \begin{cases} 1 & \text{if } x \in \Omega_1 = \left\{0 < x < 1, 0 < y < \frac{1}{2}, 0 < z < 1\right\}, \\ 10^3 & \text{if } x \in \Omega_2 = \left\{\frac{1}{2} < x < 1, \frac{1}{2} < y < 1, 0 < z < \frac{1}{2}\right\}, \\ 10 & \text{if } x \in \Omega_3 = \left\{\frac{1}{2} < x < 1, \frac{1}{2} < y < 1, \frac{1}{2} < z < 1\right\}, \\ 10^{-2} & \text{if } x \in \Omega_4 = \left\{0 < x < \frac{1}{2}, \frac{1}{2} < y < 1, 0 < z < 1\right\}. \end{cases}$$

We define the operators $b(\cdot,\cdot)$ and $a(\cdot,\cdot)$ associated with the above problem as follows:

$$b(\cdot,\cdot) \coloneqq \langle \nabla \cdot, \sigma \nabla \cdot \rangle_{L^2(\Omega)} - k^2 \langle \cdot, \cdot \rangle_{L^2(\Omega)}, \quad a(\cdot,\cdot) \coloneqq \left| \langle \nabla \cdot, \sigma \nabla \cdot \rangle_{L^2(\Omega)} \right| + \left| k^2 \right| \left| \langle \cdot, \cdot \rangle_{L^2(\Omega)} \right|. \tag{6.6}$$

Once again, $\|\cdot\|_e^2 = a(\cdot,\cdot)$ is our energy norm and $|b(\phi,\psi)| \leq |a(\phi,\psi)|$, $\forall \phi,\psi \in \mathbb{H}$.

Figure 6.1 displays the different materials in the domain. Following the definition of eq. (5.3), we select $\Omega_l = \left(\frac{3}{4},1\right)^3 \subset \Omega$. For Goal-Oriented (GO) adaptivity, Figures 6.2a and 6.2b show the solutions of the direct and adjoint problems, respectively.

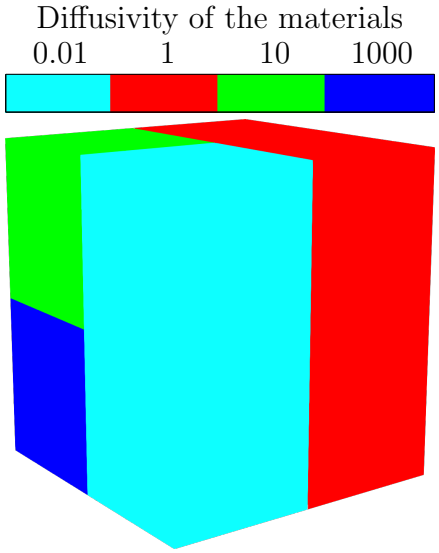

Figure 6.1.: Diffusive coefficient values for the different materials in the domain.

6.1.1. Energy-norm adaptivity

Figure 6.3 displays the final *hp*-adapted meshes for our 3D wave propagation example in a lossy medium using energy-norm adaptivity. The initial uniform mesh is composed of sixty-four root elements. As expected, we observe heavy *h*-refinements near different materials' interfaces. Figure 6.4 shows the corresponding convergence curves. As in the 2D case, the energy-norm *hp*-adaptivity provides proper convergence results in terms of energy. However, the convergence of the energy-norm adaptivity in terms of the error in the Quantity of Interest (QoI) is slow, especially in the pre-asymptotic regime.

6.1.2. Goal-Oriented adaptivity

Figure 6.5 displays the final *hp*-adapted meshes for our 3D wave propagation example in a lossy medium using GO adaptivity. The initial uniform mesh is com-

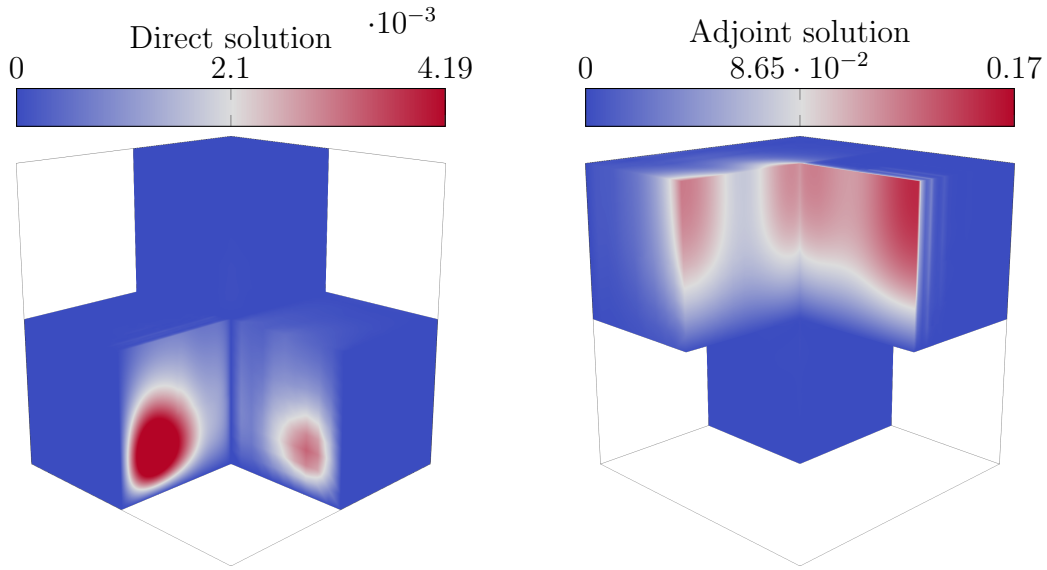

(a) Solution to the direct problem.

(b) Solution to the adjoint problem.

Figure 6.2.: Absolute value of the direct and adjoint solutions of our 3D wave propagation example in a lossy medium.

posed of sixty-four root elements. As expected, we observe heavy h-refinements near different materials' interfaces. When using GO adaptivity, the evolution of the error in the QoI exhibits much better behavior, while the energy convergence becomes suboptimal, as expected.

As computational problems grow in complexity and scale, they pose significant challenges to our computational capabilities. Developing parallel computational strategies for finite element discretization schemes [21, 150] solves these challenges. By distributing tasks and computations across multiple processors or computational nodes, these strategies can address complex engineering problems, increasing computational capacity and improving efficiency.

This dissertation follows an algorithm [99] that distributes the computational domain among participating processes. It subdivides the domain into sub-domains of relatively equal computational cost and assigns them to different processes, thus optimizing resource utilization. As the algorithm progresses, dynamic rebalancing techniques are employed to redistribute tasks, ensuring optimal load distribution across processes. Introducing adaptivity creates the challenge of balancing computational workload—techniques such as limiting refinements and process aggregation address this. Additionally, communication efficiency is supported by aggregating data into larger sets, minimizing the frequency and latency of data transfers.

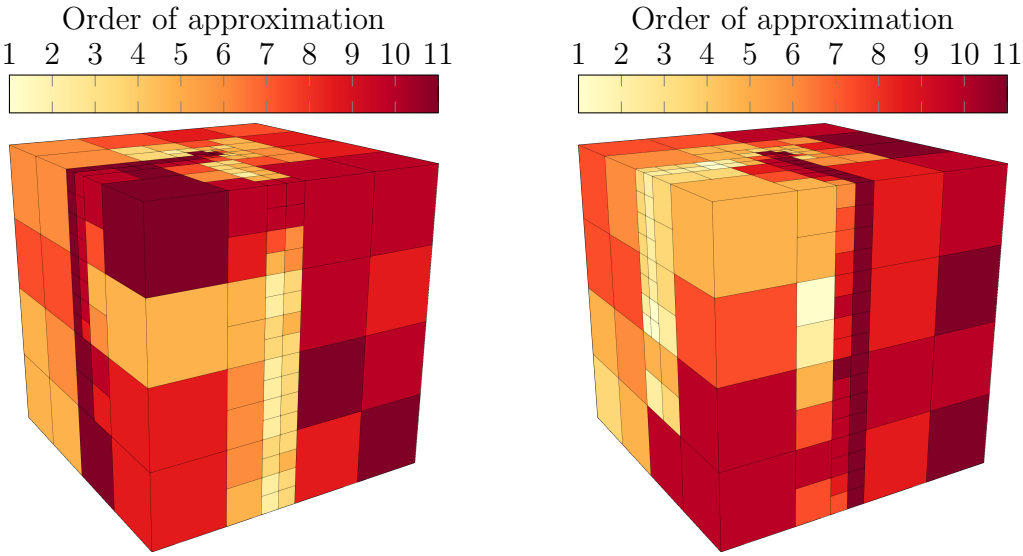

(a) Final *hp*-adapted mesh with polynomial orders p in the x-direction.

(b) Final *hp*-adapted mesh with polynomial orders p in the y-direction.

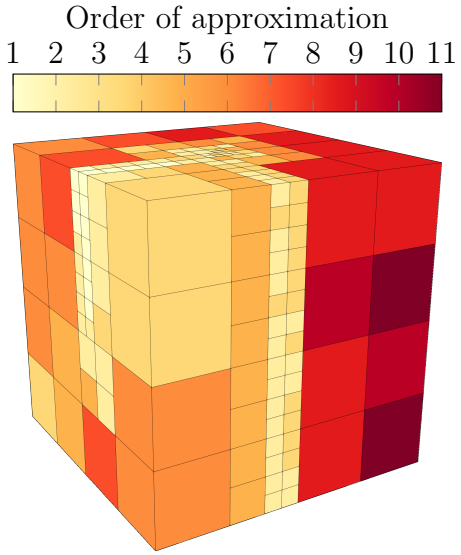

(c) Final *hp*-adapted mesh with polynomial orders p in the z-direction.

Figure 6.3.: Energy-norm adaptivity. Final *hp*-adapted meshes for our 3D wave propagation example in a lossy medium.

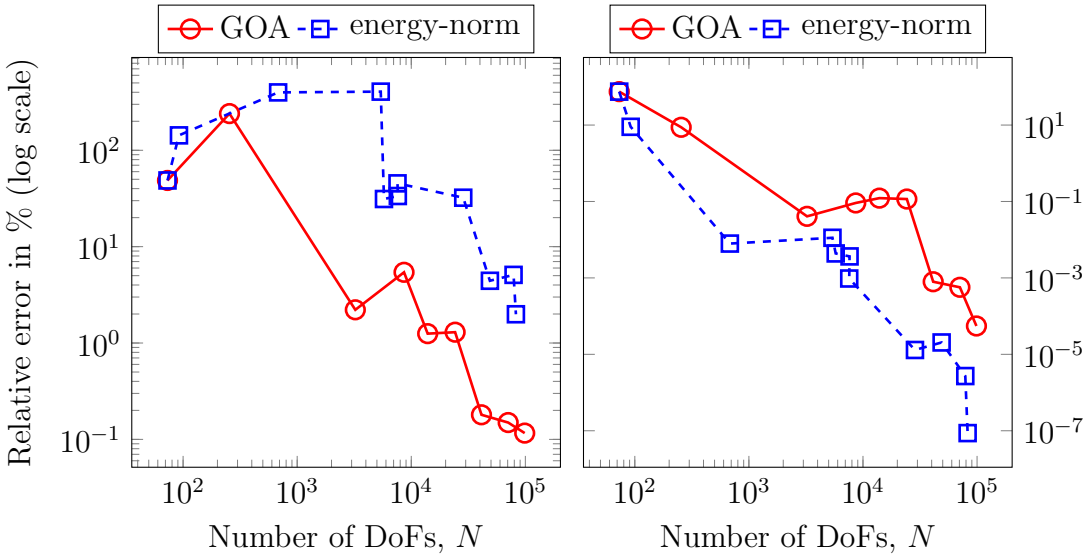

(a) Evolution of goal-oriented adaptivity. (b) Evolution of energy-norm adaptivity.

Figure 6.4.: Convergence history of $e_{\text{rel}}^{\text{QoI}}$ and $\tilde{e}_{\text{rel}}^{\text{energy}}$ for the energy-norm and GO *hp*-adaptive strategies.

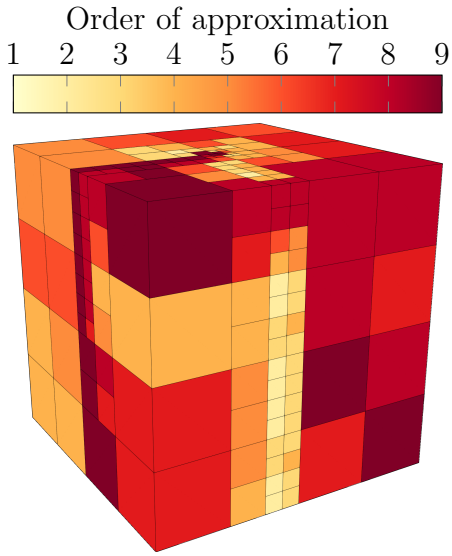

(a) Final *hp*-adapted mesh with polynomial orders p in the x-direction.

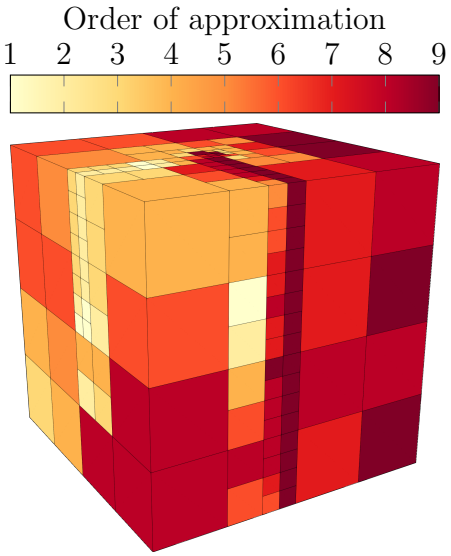

(b) Final *hp*-adapted mesh with polynomial orders p in the y-direction.

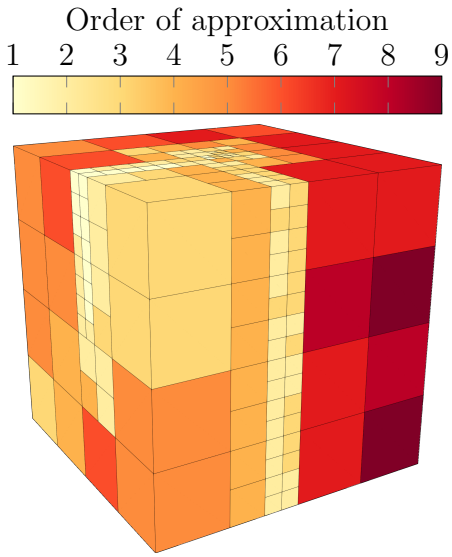

(c) Final *hp*-adapted mesh with polynomial orders p in the z-direction.

Figure 6.5.: GO adaptivity. Final *hp*-adapted meshes for our 3D wave propagation example in a lossy medium.

Part II.

Goal-Oriented hp-adaptivity for parametric PDEs.

7. Database generation for DL inversion

Deep Learning (DL) [85], a branch of Machine Learning (ML) [117], aims to emulate human learning by utilizing artificial Neural Networks (NNs) with multiple interconnected nodes. Recent studies have showcased the potential of DL to address complex challenges, such as solving parametric, high-dimensional, and fractional Partial Differential Equations (PDEs) [9, 74, 89, 103, 136, 188]. A comprehensive resource is the review by LeCun et al. [111].

The rise of ML and DL techniques has significantly impacted computational geophysics. Researchers have explored the use of DL algorithms in domains such as exploration geophysics, earthquake studies, and remote sensing [11, 31, 32, 95, 110]. DL has even found applications in geosteering [205]. The convergence of DL and geophysics is noticeable in Inverse Problem (IP), where solving forward problems becomes computationally challenging. Notably, Puzyrev et al.'s work in electromagnetic inversion is remarkable [158, 159]. Similarly, Shahriari et al. [174, 175] have significantly contributed to geosteering through DL-driven inverse approaches.

The DL-assisted solution of IPs holds excellent promise. It involves two main approaches: constructing the inverse operator and evaluating it for different measurements. This technique necessitates a comprehensive data set, often called the *ground truth*, generated by solving forward problems numerous times for various models [6, 20, 176] governed by PDEs. Despite its potential, solving IPs using DL presents its challenges [12, 106, 203], such as the non-convexity of loss functions and the requirement of basic quadrature rules for Deep Neural Networks (DNNs), as illustrated in previous studies [102, 166].

Although the integration of DL and the Finite Element Method (FEM) [34, 35, 151, 185] aims to reduce computational costs, the non-convexity of loss functions and the need for *data augmentation* remain challenges, as Jungiewicz et al. [100] and Shorten et al. [177] suggested. DL techniques continue to evolve rapidly. However, they have not superseded classical numerical methods like the FEM [28, 113, 170, 171, 201], which have demonstrated their robustness and efficiency over decades [112].

Despite the recent success of DL techniques in tackling complex problems, a sig-

nificant challenge in training a DNN to mimic the forward solver accurately lies in the need for a vast and reliable dataset. This dataset typically consists of pairs of model parameters and corresponding solutions of the forward problem governed by a PDE. However, obtaining such a dataset through accurate forward problem solutions can be computationally expensive. We propose a Multi-Adaptive Goal-Oriented (MAGO) strategy to address the computational costs and dataset requirements. The primary goal of MAGO is to generate reliable massive databases with reduced computational expenses. This strategy builds upon our previously developed Goal-Oriented Adaptive (GOA) approach for non-parametric PDEs (see Part I of this dissertation). The database generation process consists of two main stages: first, we construct a sufficiently accurate *hp*-FEM discretization for a wide range of samples, and then, we solve a massive number of FEM problems using this adapted mesh to generate the required data. The key to this approach is employing a single *hp*-adapted mesh throughout the entire data generation phase.

Generating a database of multiple sample model parameters using a GOA strategy presents several challenges. First, the computational cost of generating each adaptive mesh is high, requiring solving multiple forward problems. Second, even automatic algorithms often necessitate some user interaction, such as generating suitable initial meshes, making repeating for each sample impractical. Managing and saving many meshes, one for each sample, can lead to significant implementation complexity. As a result, this straightforward approach may not be optimal and requires an extension to handle multiple samples simultaneously.

In this chapter, we propose extending a well-established *hp*-FEM adaptive strategy [43, 44], which has demonstrated remarkable success in handling non-parametric PDEs. As widely recognized, *hp*-FEM adaptive methods are renowned for their exceptional accuracy and the ability to achieve exponential convergence rates while effectively minimizing computational costs. Therefore, *hp*-FEM automatic adaptive strategies are well-suited for tackling challenging problems, including parametric PDEs or situations where *a priori* information about the solution is unavailable.

The main innovation of our approach is that it only requires a few samples to develop a single *hp*-adaptive FEM. This single *hp*-adaptive FEM can provide highly accurate solutions for many model parameters, even those different from the original ones. We base our approach on a single *hp*-adaptive FEM and expand on the *hp*-adaptive strategy we developed earlier, as detailed in Part I of this dissertation and as summarized in Algorithm 3. Our proposed strategy can achieve a robust, fast, and computationally efficient alternative while ensuring high accuracy.

Algorithm 3: Goal-Oriented *hp*-adaptive mesh process

Input: PDE, initial finite element mesh, model parameters, definition of the Quantity of Interest (QoI)

Output: A final *hp*-adapted mesh

while *error in the QoI exceeds a certain threshold* **do**
  Perform a global refinement (user-defined);
  while *the average error indicators are above the threshold* **do**
    Solve the forward problem using eq. (7.2);
    Solve the adjoint problem using eq. (7.4);
    Calculate error indicators using eq. (7.7);
    Remove basis functions with low error indicators to unrefine the mesh;
  end
  Update error in the QoI;
end

7.1. A Goal-Oriented strategy for parametric PDEs

When dealing with the solution of parametric PDEs, we consider S different samples of model parameters. Each sample is denoted as $\boldsymbol{m}_i = \{\sigma_1, \ldots, \sigma_P\}$, where P represents the number of parameters involved in each sample. Collecting all samples can be represented as $\boldsymbol{M} = \{\boldsymbol{m}_1, \ldots, \boldsymbol{m}_S\}$. As illustrated in Figure 7.1, this contains S diverse samples of model parameters, with $P = 4$ in this specific case.

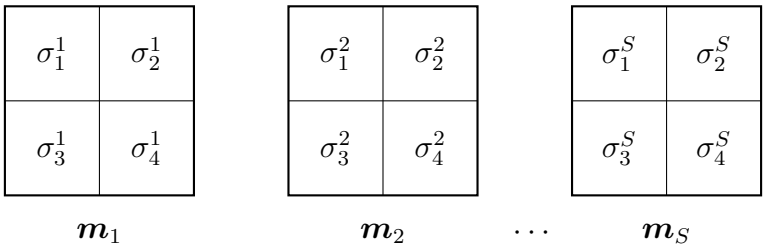

Figure 7.1.: Representation of S different samples.

7.1.1. Variational abstract formulations

In the context of numerically solving the PDEs, we consider that $0 < \sigma_i^{\min} \leq \sigma_i^{\max} < \infty$ and $b^{\boldsymbol{m}}$ corresponds to the bilinear form that characterizes the problem

related to the model $\boldsymbol{m}$. This bilinear form is continuous on $\mathbb{H} \times \mathbb{H}$ and defines an inner product on $\mathbb{H}$. Then, we define the forward direct problem in terms of the following general abstract variational formulation:

Find $u^{\boldsymbol{m}} \in \mathbb{H}$ such that

$$b^{\boldsymbol{m}}\left(u^{\boldsymbol{m}}, \phi\right) = f^{\boldsymbol{m}}\left(\phi\right), \quad \forall \phi \in \mathbb{H}, \tag{7.1}$$

where $f^{\boldsymbol{m}}$ is an element of the dual space $\mathbb{H}'$ defined by a linear form.

To discretize the abstract variational problem, we use $\mathcal{T}$ to represent a finite element mesh. We define $\mathbb{H}_{\mathcal{F}}$ as the subspace of $\mathbb{H}$ spanned by the basis functions $\{\phi_1, \ldots, \phi_{n_{\mathcal{F}}}\}$, where $\mathcal{F} = \{\phi_i\}_{i=1}^{n_{\mathcal{F}}}$. Here, $n_{\mathcal{F}}$ represents the dimension of the subspace $\mathbb{H}_{\mathcal{F}}$. The basis functions ϕ_i form a set to construct the finite element approximation. This way, we can obtain $u_{\mathcal{F}}$, corresponding to the Galerkin approximation of u within the subspace $\mathbb{H}_{\mathcal{F}}$. Then, the discrete counterpart of this abstract variational formulation reads as follows:

Find $u_{\mathcal{F}}^{\boldsymbol{m}} \in \mathbb{H}_{\mathcal{F}}$ such that

$$b^{\boldsymbol{m}}\left(u_{\mathcal{F}}^{\boldsymbol{m}}, \phi_{\mathcal{F}}\right) = f^{\boldsymbol{m}}\left(\phi_{\mathcal{F}}\right), \quad \forall \phi_{\mathcal{F}} \in \mathbb{H}_{\mathcal{F}}. \tag{7.2}$$

To lead the adaptive process of GOA strategies, we consider the associated adjoint problem to eq. (3.2), which reads as follows:

Find $v^{\boldsymbol{m}} \in \mathbb{H}$ such that

$$b^{\boldsymbol{m}}\left(\phi, v^{\boldsymbol{m}}\right) = l^{\boldsymbol{m}}\left(\phi\right), \quad \forall \phi \in \mathbb{H}, \tag{7.3}$$

where $l^{\boldsymbol{m}}$ is a linear continuous form. The discrete equivalent of this problem is given by:

Find $v_{\mathcal{F}}^{\boldsymbol{m}} \in \mathbb{H}_{\mathcal{F}}$ such that

$$b^{\boldsymbol{m}}\left(\phi_{\mathcal{F}}, v_{\mathcal{F}}^{\boldsymbol{m}}\right) = l^{\boldsymbol{m}}\left(\phi_{\mathcal{F}}\right), \quad \forall \phi_{\mathcal{F}} \in \mathbb{H}_{\mathcal{F}}. \tag{7.4}$$

7.1.2. Element-wise indicators

We aim to quantify the change in the QoI when we remove certain basis functions from the set of *removable* basis functions $\mathcal{R}_K$ associated with an element $K \in \mathcal{T}$. Specifically, we are interested in controlling $\left|l\left(u_{\mathcal{F}}^{\boldsymbol{m}}\right) - l\left(u_{\mathcal{E}_K}^{\boldsymbol{m}}\right)\right|$, $\forall K \in \mathcal{T}$.

Since we are dealing with a single mesh, we do not directly compute the solution $u^{\boldsymbol{m}}_{\mathcal{E}_K}$ associated with eq. (3.2) on $\mathcal{E}_K$. Instead, we approximate it by projecting $u^{\boldsymbol{m}}_{\mathcal{F}}$ into $\mathcal{E}_K$. This projection is performed using the *projection* operator defined in Section 3.2, which simulates the presence of a second grid without explicitly implementing it. Given a subset of basis functions $\mathcal{S} \subset \mathcal{F}$ that generates a space $\mathbb{H}_{\mathcal{S}} \subset \mathbb{H}_{\mathcal{F}}$, the projection operator $\Pi^{\mathcal{S}}_{\mathcal{F}}$ maps $\mathbb{H}_{\mathcal{F}}$ to $\mathbb{H}_{\mathcal{S}}$ and is defined as follows:

$$\Pi^{\mathcal{S}}_{\mathcal{F}} u^{\boldsymbol{m}}_{\mathcal{F}} \coloneqq \sum_{\phi_i \in \mathcal{S}} u^{\boldsymbol{m}}_i \phi_i. \tag{7.5}$$

Using Section 3.3, we find that

$$\left| l\left(u^{\boldsymbol{m}}_{\mathcal{F}}\right) - l\left(u^{\boldsymbol{m}}_{\mathcal{E}_K}\right) \right| \simeq \left| b\left(\Pi^{\mathcal{R}_K}_{\mathcal{F}} u^{\boldsymbol{m}}_{\mathcal{F}}, \Pi^{\mathcal{R}_K}_{\mathcal{F}} v^{\boldsymbol{m}}_{\mathcal{F}}\right) \right| \leq \left| a\left(\Pi^{\mathcal{R}_K}_{\mathcal{F}} u^{\boldsymbol{m}}_{\mathcal{F}}, \Pi^{\mathcal{R}_K}_{\mathcal{F}} v^{\boldsymbol{m}}_{\mathcal{F}}\right) \right|, \tag{7.6}$$

where a is an alternative operator —not necessarily the original bilinear form— such that $|b(\phi,\psi)| \leq |a(\phi,\psi)|\ \forall \phi,\psi \in \mathbb{H}$ and $\|\cdot\|^2_e = a(\cdot,\cdot)$ is the energy norm of the problem (i.e., a defines an inner product).

The basis functions associated with small values in eq. (7.6) are expected to have limited impact on the solution $u^{\boldsymbol{m}}_{\mathcal{F}}$; thus, eliminating them should not significantly affect the error in the QoI. Therefore, we define the isotropic element-wise indicators $\eta_K, \forall K \in \mathcal{T}$, as follows:

$$\eta_K \coloneqq \left| a\left(\Pi^{\mathcal{R}_K}_{\mathcal{F}} u^{\boldsymbol{m}}_{\mathcal{F}}, \Pi^{\mathcal{R}_K}_{\mathcal{F}} v^{\boldsymbol{m}}_{\mathcal{F}}\right) \right|, \quad \forall K \in \mathcal{T}, \tag{7.7}$$

and subsequently remove those basis functions with small indicators. For details on anisotropic indicators, implementation technicalities, and further information, we refer the interested reader to [43, 59].

7.1.3. A Multi-Adaptive Goal-Oriented strategy

Now, let us explore the concept of MAGO. In this approach, we have S forward and adjoint problems, with each sample associated with a specific QoI denoted as $l^{\boldsymbol{m}_i}$, where $i = 1, \ldots, S$. Our main goal is to construct a single final hp-mesh, optimizing its size to be as small as possible while ensuring accurate computation of the QoI for all the samples in a single GOA process. To achieve this, we solve the S forward discrete problems given by:

> Find $u^{\boldsymbol{m}_i}_{\mathcal{F}} \in \mathbb{H}_{\mathcal{F}}$ such that
>
> $$b^{\boldsymbol{m}_i}\left(u^{\boldsymbol{m}_i}_{\mathcal{F}}, \phi_{\mathcal{F}}\right) = f^{\boldsymbol{m}_i}\left(\phi_{\mathcal{F}}\right), \quad \forall \phi_{\mathcal{F}} \in \mathbb{H}_{\mathcal{F}}. \tag{7.8}$$

Similarly, the discrete abstract variational formulation for solving the S associated adjoint discrete problems is as follows:

Find $v_{\mathcal{F}}^{\boldsymbol{m}_i} \in \mathbb{H}_{\mathcal{F}}$ such that

$$b^{\boldsymbol{m}_i}\left(\phi_{\mathcal{F}}, v_{\mathcal{F}}^{\boldsymbol{m}_i}\right) = l^{\boldsymbol{m}_i}\left(\phi_{\mathcal{F}}\right), \quad \forall \phi_{\mathcal{F}} \in \mathbb{H}_{\mathcal{F}}, \tag{7.9}$$

where $i = 1, \ldots, S$, indicating that we solve the S forward and adjoint discrete problems.

Following the approach outlined in Section 3.3, our next step is to determine the basis functions inside the set of *removable* basis functions, denoted as $\mathcal{R}_K$, that do not significantly affect the error in the QoI when eliminating them. Then, assuming that our discretization $\mathcal{T}$ computes all the Quantities of Interest (QoIs) efficiently, from eq. (7.7) we have that for each sample $i = 1, \ldots, S$:

$$\left|l\left(u_{\mathcal{F}}^{\boldsymbol{m}_i}\right) - l\left(u_{\mathcal{E}_K}^{\boldsymbol{m}_i}\right)\right| \simeq \left|b\left(\Pi_{\mathcal{F}}^{\mathcal{R}_K} u_{\mathcal{F}}^{\boldsymbol{m}_i}, \Pi_{\mathcal{F}}^{\mathcal{R}_K} v_{\mathcal{F}}^{\boldsymbol{m}_i}\right)\right| \leq \left|a\left(\Pi_{\mathcal{F}}^{\mathcal{R}_K} u_{\mathcal{F}}^{\boldsymbol{m}_i}, \Pi_{\mathcal{F}}^{\mathcal{R}_K} v_{\mathcal{F}}^{\boldsymbol{m}_i}\right)\right|. \tag{7.10}$$

In this expression, we control the error in each sample individually. However, we need an indicator that combines all the samples simultaneously since the objective is to perform a single GOA procedure. To do so, we define an element-wise error indicator η_K for each element K as follows:

$$\eta_K = \left\|a\left(\Pi_{\mathcal{F}}^{\mathcal{R}_K} u_{\mathcal{F}}^{\boldsymbol{m}_i}, \Pi_{\mathcal{F}}^{\mathcal{R}_K} v_{\mathcal{F}}^{\boldsymbol{m}_i}\right)\right\|_{l^p}. \tag{7.11}$$

Using the l^p norm, we combine the individual errors from all S samples into one. Thus, by removing the basis functions with small combined contributions, we ensure that the error in all the QoIs remains unaltered. It is worth mentioning that the choice of the norm in eq. (7.11) is up to the user and may depend on the specific application.

We propose the MAGO strategy in Algorithm 4, which utilizes a sequence of mesh refinements and coarsening, following a similar concept as in Section 3.1. However, in the MAGO approach, we aim to provide sufficiently accurate solutions for all the samples. Therefore, we iterate the adaptive process until the error in the worst-case scenario is below a user-prescribed tolerance. The termination criterion is defined by ensuring that the errors in the QoI between a fine mesh F and a coarser mesh C are below a specified tolerance TOL for all the samples:

$$\max_{i,\, \{\boldsymbol{m}_i\}_{i=1}^{S}} \left\{ \frac{\left|l\left(u_{\mathrm{F}}^{\boldsymbol{m}_i}\right) - l\left(u_{\mathrm{C}}^{\boldsymbol{m}_i}\right)\right|}{\left|l\left(u_{\mathrm{F}}^{\boldsymbol{m}_i}\right)\right|} \right\} < TOL. \tag{7.12}$$

It is important to note that the successive global refinements guarantee the convergence of this procedure for one or more samples, while the coarsening stages ensure almost optimal convergence rates [29, 40]. By combining these adaptive steps, the MAGO approach efficiently constructs a single *hp*-mesh that accurately captures the QoIs for all the samples simultaneously.

Algorithm 4: Multi-Adaptive Goal-Oriented adaptive process

Input: PDE, initial finite element mesh, S samples of model parameters, definition of the QoI

Output: A final *hp*-adapted mesh

while *eq.* (7.12) *is not satisfied* **do**
    Perform a global refinement (user-defined);
    while *error indicators above threshold* **do**
        for *each sample* $\boldsymbol{m}_i$ *where* $i = 1$ *to* S **do**
            Solve the forward problem for sample $\boldsymbol{m}_i$ using eq. (7.8);
            Solve the adjoint problem for sample $\boldsymbol{m}_i$ using eq. (7.9);
            Calculate error indicators for the i-th sample using eq. (7.7);
        end
        Compute the error indicators using eq. (7.11), which combines those from all samples into a single measure;
        Remove basis functions with low error indicators to unrefine the mesh;
    end
    Update error in the QoI;
end

7.2. Generation of databases

We refer to the two main stages of the database production process as the *Adaptive* and *Generation* processes. In the *Adaptive* process, which is the initial stage, we construct a highly accurate *hp*-grid, referred to as the adapted mesh, capable of accommodating an arbitrary number of samples (S_{A}). Subsequently, in the *Generation* process, we employ this adapted mesh to solve multiple FEM problems, generating the required data. This approach's key aspect is using a single *hp*-FEM, i.e., the adapted mesh, throughout the entire *Generation* process.

To elaborate further, we begin by generating a reduced number of samples of model parameters (S_{A}) that parametrize the PDE of the problem. We then construct the adapted mesh, ensuring it satisfies eq. (7.12), where the maximum error for all the S_{A} samples falls below a user-prescribed tolerance. The central concept behind this approach is the anticipation of achieving low errors when employing the adapted mesh with samples different from those used in the adaptive process. In the subsequent *Generation* process, we solve one FEM problem for each sample in S_{G}, which represents a set of additional samples we consider. This process allows us to obtain accurate synthetic data or measurements database. The overall process can be summarized as follows:

1. *Adaptive* process:
   a) Generate S_{A} samples of model parameters to be used in the *Adaptive* process.
   b) Construct the adapted grid by employing the *hp*-FEM following the guidelines described in Section 7.1.
2. *Generation* process:
   a) Generate S_{G} additional samples of model parameters specifically for the *Generation* process.
   b) For each sample in S_{G}, solve a FEM problem using the adapted mesh, which was specifically designed during the *Adaptive* process to deliver highly accurate solutions for a wide range of model parameters.

By following this approach, we can efficiently generate a reliable database of accurate synthetic data or measurements using a single adapted mesh for multiple samples, thereby reducing computational expenses and maintaining high accuracy across various scenarios.

7.2.1. Computational costs of MAGO

The GOA strategy, elaborated upon in Part I of this dissertation and presented in Algorithm 3, comprises a series of refining and coarsening steps. We use a

direct solver to solve each FEM problem, contributing to the computational cost of building the *hp*-mesh. The total cost is given by:

$$C^{\mathrm{GOA}} = \sum_{i=1}^{N\mathrm{rIter}} \sum_{j=1}^{N\mathrm{rCoarse}} \Big[C_{\mathrm{as}}\left(N^{ij}\right) + C_{\mathrm{an}}\left(N^{ij}\right) + C_{\mathrm{fa}}\left(N^{ij}\right) + 2\, C_{\mathrm{so}}\left(N^{ij}\right) + C_{\mathrm{es}}\left(N^{ij}\right) \Big]. \tag{7.13}$$

Each component of the cost corresponds to specific operations: C_{as} for assembling the matrix, C_{an} for the analysis part of the direct solver, C_{fa} for factorization, C_{so} for solving the linear system of equations after factorization (i.e., backward elimination), and C_{es} for computing the error estimators. Additionally, N^{ij} represents the number of Degrees of Freedom (nDoF) of the meshes at each iteration i of the adaptive process and each coarsening step j associated with each iteration i. Notably, the factor of 2 in the C_{so} term accounts for solving both the forward and adjoint problems. Since we use a direct solver, the extra cost for solving the adjoint problem associated with the forward problem reduces to only backward and forward substitutions.

The costs related to the finest grid with N_{f} Degrees of Freedom (DoF) dominate those associated with the coarser grids. Consequently, we can approximate Equation (7.13) by:

$$C^{\mathrm{GOA}}\left(N_{\mathrm{f}}\right) \approx C_{\mathrm{as}}\left(N_{\mathrm{f}}\right) + C_{\mathrm{an}}\left(N_{\mathrm{f}}\right) + C_{\mathrm{fa}}\left(N_{\mathrm{f}}\right) + 2\, C_{\mathrm{so}}\left(N_{\mathrm{f}}\right) + C_{\mathrm{es}}\left(N_{\mathrm{f}}\right). \tag{7.14}$$

Thus, the approximate costs of generating a database of S_{G} samples with the Single-Adaptive Goal-Oriented (SAGO) and the MAGO approaches are as follows:

SAGO approach: We approximate the computational cost C^{SAGO} of generating one GOA mesh for each of the S_{G} samples by:

$$C^{\mathrm{SAGO}} = \sum_{i=1}^{S_{\mathrm{G}}} C^{\mathrm{GOA}}\left(N_{\mathrm{f}}^{(i)}\right). \tag{7.15}$$

MAGO approach: The cost C^{MAGO} of generating the database with the MAGO strategy is the sum of the costs of constructing the adapted mesh C^{A} plus the cost of actually generating the data C^{G}, that is, $C^{\mathrm{MAGO}} = C^{\mathrm{A}} + C^{\mathrm{G}}$.

We approximate the cost of the *Adaptive* process with S_{A} samples by:

$$C^{\mathrm{A}} = S_{\mathrm{A}}\, C^{\mathrm{GOA}}\left(N_{\mathrm{f}}^{\mathrm{mago}}\right), \tag{7.16}$$

where $N_{\mathrm{f}}^{\mathrm{mago}}$ represents the nDoF in the fine mesh adapted using the MAGO strategy.

After generating the adapted coarse mesh of size $N_{\mathrm{c}}^{\mathrm{mago}}$, we proceed to generate the data. The approximate cost of the *Generation* process is then given by:

$$C^{\mathrm{G}} = S_{\mathrm{G}}\left[C_{\mathrm{as}}\left(N_{\mathrm{c}}^{\mathrm{mago}}\right) + C_{\mathrm{an}}\left(N_{\mathrm{c}}^{\mathrm{mago}}\right) + C_{\mathrm{fa}}\left(N_{\mathrm{c}}^{\mathrm{mago}}\right) + 2\,C_{\mathrm{so}}\left(N_{\mathrm{c}}^{\mathrm{mago}}\right)\right]. \tag{7.17}$$

In our MAGO approach, all samples share the same discretization, which conforms with the material parameters of the PDE. This design allows us to precompute and reuse certain information across different samples. As detailed in the following subsection, we perform precomputations for the integrals of the global matrices and the analysis part of the direct solver of equations, thereby reducing the assembling and analysis processes to a single occurrence. Considering that the cost of computing the estimators is comparable to the cost of assembling [146], we obtain the following approximations:

$$C^{\mathrm{A}} = 2\,C_{\mathrm{as}}\left(N_{\mathrm{f}}^{\mathrm{mago}}\right) + C_{\mathrm{an}}\left(N_{\mathrm{f}}^{\mathrm{mago}}\right) + S_{\mathrm{A}}\left[C_{\mathrm{fa}}\left(N_{\mathrm{f}}^{\mathrm{mago}}\right) + 2\,C_{\mathrm{so}}\left(N_{\mathrm{f}}^{\mathrm{mago}}\right)\right], \tag{7.18}$$

and

$$C^{\mathrm{G}} = C_{\mathrm{as}}\left(N_{\mathrm{c}}^{\mathrm{mago}}\right) + C_{\mathrm{an}}\left(N_{\mathrm{c}}^{\mathrm{mago}}\right) + S_{\mathrm{G}}\left[C_{\mathrm{fa}}\left(N_{\mathrm{c}}^{\mathrm{mago}}\right) + 2\,C_{\mathrm{so}}\left(N_{\mathrm{c}}^{\mathrm{mago}}\right)\right]. \tag{7.19}$$

Compared to the SAGO approach, the costs associated with assembling, analysis, and estimation occur only once due to the precomputations, contributing to improved efficiency and reduced computational overhead.

Factorization costs dominate other aspects in traditional C^0-continuous FEM problems when using a direct solver. It scales as (see, e.g., [52, 53]):

$$\mathcal{O}\left(N^{(1+(d-1)/2)}\right), \tag{7.20}$$

where $d = 1, 2, 3$ represents the dimension of the problem and N denotes the nDoF. The final approximate costs for the SAGO and MAGO approaches are as follows:

$$C^{\mathrm{SAGO}} \approx \sum_{i=1}^{S_{\mathrm{G}}} C_{\mathrm{fa}}\left(N_{\mathrm{f}}^{i}\right) \approx S_{\mathrm{G}}\left[C_{\mathrm{fa}}\left(N_{\mathrm{f}}^{\mathrm{sago}}\right)\right], \tag{7.21}$$

where $N_{\mathrm{f}}^{\mathrm{sago}}$ represents an average value (using eq. (7.20)) of the nDoF of the S_{G} fine grids, and

$$C^{\mathrm{MAGO}} = S_{\mathrm{A}}\left[C_{\mathrm{fa}}\left(N_{\mathrm{f}}^{\mathrm{mago}}\right)\right] + S_{\mathrm{G}}\left[C_{\mathrm{fa}}\left(N_{\mathrm{c}}^{\mathrm{mago}}\right)\right]. \tag{7.22}$$

While $S_{\mathrm{A}} \ll S_{\mathrm{G}}$, the relationship between $N_{\mathrm{f}}^{\mathrm{mago}}$, $N_{\mathrm{c}}^{\mathrm{mago}}$, and $N_{\mathrm{f}}^{\mathrm{sago}}$ is not generalizable. This relationship depends on various factors, including the initial mesh configuration, the refinement and coarsening criteria, the convergence behavior of the solution, and the problem's complexity. In some instances, investing resources in building a sufficiently good adapted mesh with only a fraction of samples is reasonable. The gains in the *Generation* part of the strategy will likely compensate for this computational effort, considering the specific problem. Consequently, we expect that $C^{\mathrm{MAGO}} < C^{\mathrm{SAGO}}$. However, it is essential to note that the number of samples S_{A} and the mesh size significantly impact the accuracy of the generated data. Thus, a tradeoff exists between accuracy and the cost of obtaining the adapted mesh.

7.2.2. Precomputations of the global matrices

In many adaptive FEM implementations, the integrals associated with the bilinear form and error indicators are calculated element by element. However, when dealing with many material samples S (possibly reaching hundreds of thousands), computing all these integrals for each sample becomes computationally expensive. To overcome this challenge, we take advantage of our materials being piecewise constant and conforming to discretization. We perform a clever optimization by precomputing and storing the integrals for an arbitrary *unitary* sample, where material properties are assumed to equal one. Once these integrals are precomputed, we can reuse this information across all samples instead of recalculating the integrals for each sample. This technique significantly accelerates the integration process and reduces the computational cost of handling many material samples.

The bilinear form in the problem may consist of multiple terms, denoted as:

$$b^{\boldsymbol{m}_i}(\cdot,\cdot) = \sum_{j=1}^{M_b} b_j^{\boldsymbol{m}_i}(\cdot,\cdot), \tag{7.23}$$

where M_b represents the number of terms in the bilinear form.

For each material sample $\boldsymbol{m}_i$, we compute the contributions associated with each element K as follows:

$$\left[b^{\boldsymbol{m}_i}(\cdot,\cdot)\right]_K = \sum_{j=1}^{M_b} m_i^j(K)\left[b_j^1(\cdot,\cdot)\right]_K, \tag{7.24}$$

Algorithm 5: Precomputation of element-wise matrices

Input: Given variational formulation
Output: Pre-computed element-wise unitary matrices

for *Each term in the bilinear form* ($j = 1, \ldots, M_b$) **do**
  for *Each element in the finite element discretization* ($K \in \mathcal{T}$) **do**
    Compute and store the element-wise unitary matrix $\left[b_j^1(\cdot,\cdot)\right]_K$;
  end
end

Algorithm 6: Precomputation: assembling the global matrices

Input: Variational formulation of the problem, S samples, pre-computed matrices
Output: Assembled global matrices for all samples

for *Each sample* $\boldsymbol{m}_i$ ($i = 1, \ldots, S$) **do**
  for *Each term in the bilinear form* ($j = 1, \ldots, M_b$) **do**
    for *Each element in the finite element discretization* ($K \in \mathcal{T}$) **do**
      Initialize the element-wise matrix to zero: $[b^{\boldsymbol{m}_i}(\cdot,\cdot)]_K = 0$;
      Load the pre-computed element-wise unitary matrix $\left[b_j^1(\cdot,\cdot)\right]_K$ (see Algorithm 5);
      Load the material property of the element ($m_i^j(K)$);
      Update the value of the element matrix $[b^{\boldsymbol{m}_i}(\cdot,\cdot)]_K = [b^{\boldsymbol{m}_i}(\cdot,\cdot)]_K + m_i^j(K)\left[b_j^1(\cdot,\cdot)\right]_K$;
      Assemble the global matrix by inserting $[b^{\boldsymbol{m}_i}(\cdot,\cdot)]_K$ into $b^{\boldsymbol{m}_i}(\cdot,\cdot)$;
    end
  end
  We obtain the fully assembled matrix associated with the i-th sample.
end

where $m_i^j(K)$ represents the scalar material property associated with the K-th element of the i-th material sample and the j-th term of the bilinear form. Additionally, $\left[b_j^1(\cdot,\cdot)\right]_K$ corresponds to the j-th *unitary* element-wise bilinear term (sub-matrix) associated with the element K. Specifically, $m_i^j(K) = 1$ for the bilinear terms independent of the material properties.

To optimize the computation process, we pre-compute and store all the unitary integrals in $\left[b_j^1(\cdot,\cdot)\right]_K$ for all elements in the discretization, $K \in \mathcal{T}$, and for $j = 1, \ldots, M_b$. This way, we only need to compute these integrals once and then load the pre-computed unitary sub-matrices for each of the S samples. By multiplying them with the corresponding material property for each element, we can efficiently assemble the global bilinear matrices and compute the error indicators as scalar products according to eq. (7.10). The overall process is summarized using the following algorithms: Algorithm 5 shows how we compute and store the *unitary* element-wise matrices; Algorithms 6 and 7 explain how we construct the global matrices and compute the error indicators, respectively, utilizing the pre-computed information.

Algorithm 7: Precomputation: computation of the error indicators

Input: Error indicator, variational formulation of the error, S samples, pre-computed matrices, forward and adjoint solutions

Output: Error indicator for all samples at the same time

for *Each sample* $\boldsymbol{m}_i$ $(i = 1, \ldots, S)$ **do**
  for *Each term in the bilinear form* $(j = 1, \ldots, M_b)$ **do**
    for *Each element in the finite element discretization* $(K \in \mathcal{T})$ **do**
      Initialize the element-wise matrix to zero: $[a^{\boldsymbol{m}_i}(\cdot,\cdot)]_K = 0$;
      Load the pre-computed element-wise unitary matrix $\left[a_j^1(\cdot,\cdot)\right]_K$ from Algorithm 5;
      Load the material property of the element as $m_i^j(K)$;
      Update the element matrix as $[a^{\boldsymbol{m}_i}(\cdot,\cdot)]_K = [a^{\boldsymbol{m}_i}(\cdot,\cdot)]_K + m_i^j(K)\left[a_j^1(\cdot,\cdot)\right]_K$;
    end
  end
  Compute the error indicators for the i-th sample using eq. (7.7);
end
Compute a single error indicator considering all the samples according to eq. (7.11);

Notably, the precomputation of global matrices can be utilized in both the *Adaptive* and *Generation* parts, enhancing the efficiency of the adaptive FEM.

7.3. Numerical results

This section demonstrates the performance of the MAGO approach in generating large databases for various problems. It highlights the method's capability to adaptively construct meshes and compute the QoI across a broad spectrum of sample configurations. The primary objective is to design an optimized single *hp*-mesh, whose size is as small as possible, to efficiently determine the QoI for all samples. These QoI are denoted as $l\left(u^{\boldsymbol{m}_i}\right)$ for $i = 1, \ldots, S$.

7.3.1. Definitions

We categorize the numerical results into three categories based on the purpose they serve:

1. To demonstrate the quasi-exponential convergence of the MAGO strategy, showcasing how the MAGO approach achieves rapid convergence in adaptive mesh generation.

2. To verify the accuracy of the produced measurements, assess the precision of the computed QoI values obtained using the MAGO approach.

3. To highlight the numerical advantages of the MAGO approach, quantifying its benefits in terms of computational efficiency and mesh size reduction.

The problems considered include 2D scenarios involving Poisson and Helmholtz equations. The Hilbert space $\mathbb{H}$ chosen for all problems is defined as $\mathbb{H} = \{u \in H^1(\Omega) \mid u = 0 \text{ on } \Gamma_D\}$, where Γ_D denotes the boundary with Dirichlet boundary conditions. The mesh is designed specifically for all scenarios' materials, sources, and desired QoI.

7.3.1.1. Convergence of the MAGO adaptivity

We investigate the convergence behavior of the MAGO approach by varying the number of samples S_{A} used to construct adapted meshes. This follows the procedure detailed in Item 1 of Section 7.2. We present visualizations of the final adapted *hp*-meshes for various cases and introduce quasi-exponential convergence curves, showcasing the effectiveness of the MAGO strategy.

To calculate convergence, we calculate two relative errors in the QoI concerning the nDoF during the adaptive processes: the maximum relative error $e_{\mathrm{rel}}^{\mathrm{max}}$ and the mean relative error $e_{\mathrm{rel}}^{\mathrm{mean}}$.

These errors are computed among the S_{A} samples, where the value of S_{A} varies based on specific examples. The maximum relative error is given by:

$$e_{\mathrm{rel}}^{\max} = \max_{i=1,\dots,S} \left| \frac{l\left(u^{\boldsymbol{m}_i}\right) - l\left(u_{\mathcal{T}}^{\boldsymbol{m}_i}\right)}{l\left(u^{\boldsymbol{m}_i}\right)} \right| \cdot 100. \tag{7.25}$$

The mean relative error is:

$$e_{\mathrm{rel}}^{\mathrm{mean}} = \frac{1}{S} \sum_{i=1}^{S} \left| \frac{l\left(u^{\boldsymbol{m}_i}\right) - l\left(u_{\mathcal{T}}^{\boldsymbol{m}_i}\right)}{l\left(u^{\boldsymbol{m}_i}\right)} \right| \cdot 100. \tag{7.26}$$

In these equations, $u^{\boldsymbol{m}_i}$ and $u_{\mathcal{T}}^{\boldsymbol{m}_i}$ represent the solutions linked to a given model $\boldsymbol{m}_i$ on a fine and a coarser mesh, respectively. The maximum relative error highlights the worst-case error among samples, whereas the mean relative error offers an average accuracy overview. The maximum, mean, and traditional (e_{rel}) relative errors are identical for a single sample.

7.3.1.2. Computational costs of generating the database

Equations (7.21) and (7.22) provide an approximate estimation of the computational costs for the SAGO and MAGO approaches, respectively, where the cost is influenced by the nDoF, as articulated in Equation (7.20). Consequently, we approximate the computational cost C^{SAGO} of generating one GOA mesh for each of the S_{G} samples by:

$$C^{\mathrm{SAGO}} \approx \sum_{i=1}^{S_{\mathrm{G}}} \left(N_{\mathrm{f}(i)}^{\mathrm{sago}} \right)^{(1+(d-1)/2)}. \tag{7.27}$$

In addition, we provide an approximate estimation of the computational costs for the MAGO by:

$$C^{\mathrm{MAGO}} \approx \sum_{i=1}^{S_{\mathrm{A}}} \left(N_{\mathrm{f}(i)}^{\mathrm{mago}} \right)^{(1+(d-1)/2)} + \sum_{i=1}^{S_{\mathrm{G}}} \left(N_{\mathrm{c}(i)}^{\mathrm{sago}} \right)^{(1+(d-1)/2)}. \tag{7.28}$$

While we may omit certain additional costs for clarity, it is essential to highlight that generating the database using the MAGO approach yields significant savings, as detailed in Section 7.2.

7.3.1.3. Generating model parameter samples

We generate all model parameter samples randomly. Specifically, we use a uniform distribution over the interval $[-1, 3]$ to derive the values of $\log_{10}(m_i)$. Consequently, the values of σ_i can vary by up to four orders of magnitude, ranging from 10^{-1} to 10^{3}.

7.3.2. Wave propagation example

We consider the following non-elliptic problem based on Helmholtz's equation.

> Find u such that
>
> $$-\nabla \cdot (\nabla u) - j\sigma(\boldsymbol{x})\, u = 1 \text{ in } \Omega, \tag{7.29}$$
> $$u = 0 \text{ on } \partial\Omega. \tag{7.30}$$

7.3.2.1. Example: wave propagation problem

We employ a 5×5 grid for numerical computations, encompassing a square computational domain, $\Omega = [0,1]^2$. Within this domain, we distinguish two regions, Ω_f and Ω_l, which symbolize the source and the QoI, respectively. These regions are defined within Ω as $\Omega_f = \left(\frac{1}{20}, \frac{3}{20}\right)^2$ and $\Omega_l = \left(\frac{17}{20}, \frac{19}{20}\right)^2$, with the origin situated at the bottom-left corner of the domain. Figure 7.2 shows the computational domain Ω, its boundary $\partial\Omega$ (subject to Dirichlet conditions), and the locations of Ω_l and Ω_f. In this depiction, Ω_l defines the region of the QoI function $l(\phi)$, whereas Ω_f is the region for the source function.

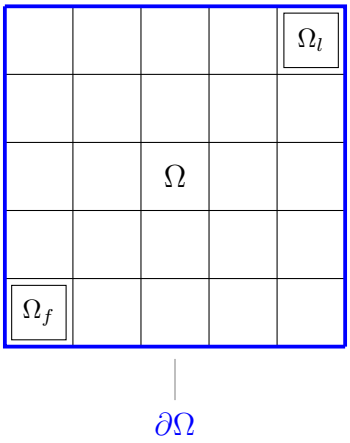

Figure 7.2.: Our grid-based domain example is defined over the domain Ω. The Dirichlet boundary condition is denoted by $\partial\Omega$. The source function is supported on Ω_f, and the QoI $l(\phi)$ is supported on Ω_l.

Figures 7.3a and 7.3b show the absolute values of forward and adjoint numerical solutions on a logarithmic scale.

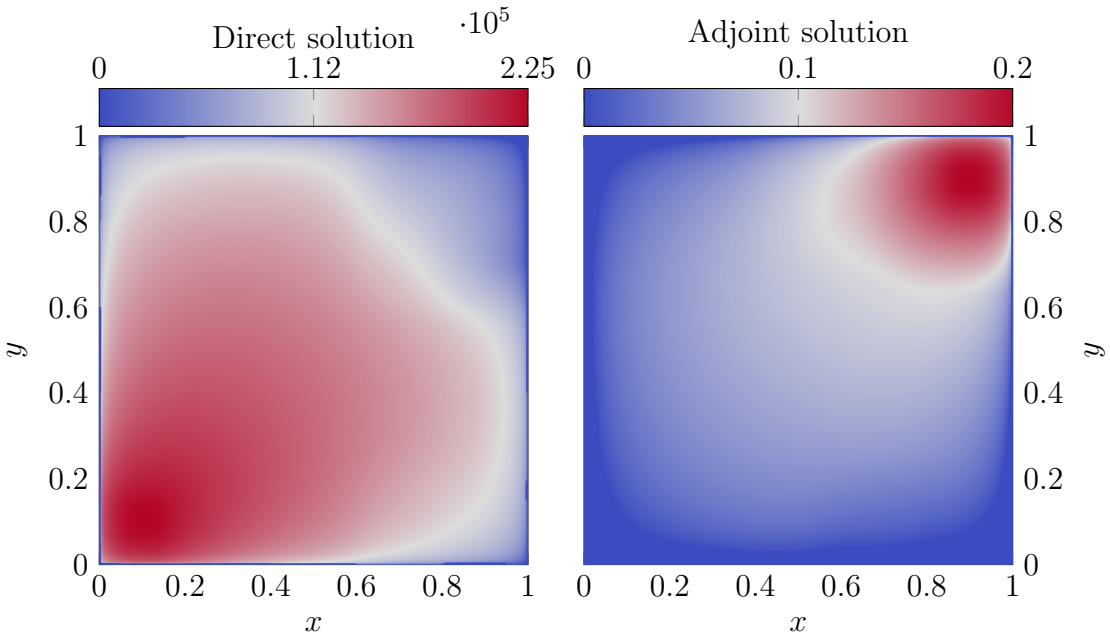

(a) Solution to the direct problem.

(b) Solution to the adjoint problem.

Figure 7.3.: Absolute value of the solutions of our wave propagation example.

7.3.2.2. Wave propagation: convergence

Figure 7.4 presents the numerical results for the wave propagation example using just a single sample for the adaptive process, consistent with the GOA approach as referenced in [43, 44]. This wave propagation final *hp*-adapted grids are shown in Figures 7.4a and 7.4b. The material coefficient distribution across the domain is depicted in Figure 7.4c. We observe significant *p*-refinements alongside the *h*-refinements towards the material discontinuities expected for this equation. The quasi-optimal exponential convergence graph for this scenario, along with the progress of $e_{\text{rel}}^{\text{max}}$ and $e_{\text{rel}}^{\text{mean}}$, can be found in Figure 7.4d. For a comprehensive understanding of the adaptive process's performance, we also examined varying S_{A} counts. Results corresponding to S_{A} values of 5, 10, 100, and 1000 are detailed in Figures 7.5 to 7.8.

MAGO's adaptive strategy exhibits a quasi-optimal convergence rate, showing consistent behavior across the three norms chosen for error indicator combination (l_1, l_2, and l_∞), which are represented by red, blue, and grey lines, respectively. This process aligns with the traditional GOA approach for a single sample, leading us to depict only a single curve. However, as the number of samples increases, maintaining precision for all on a single *hp* grid becomes more challenging.

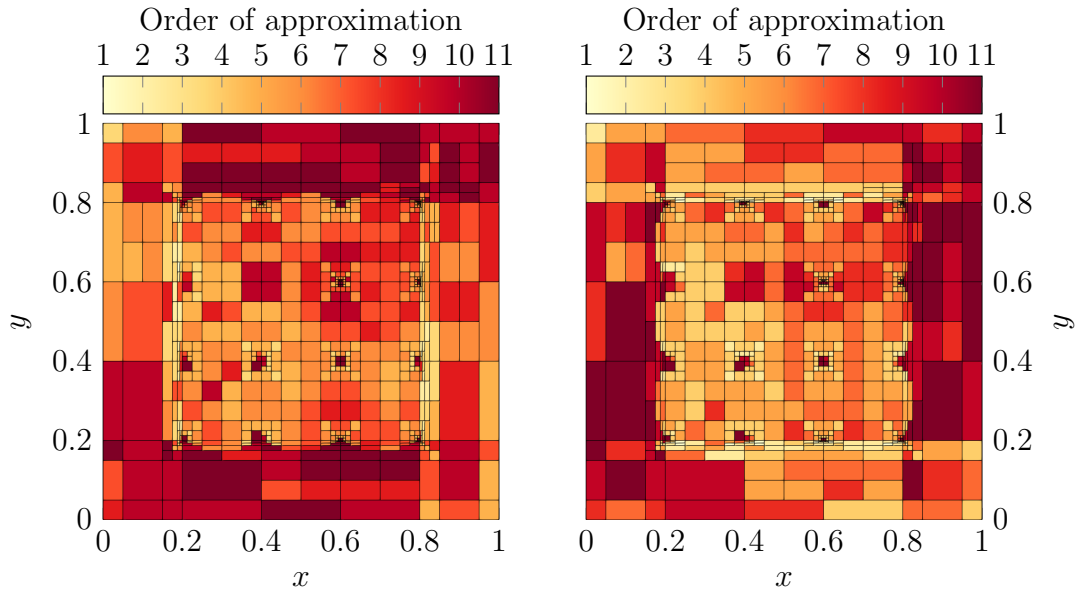

(a) Final *hp*-adapted mesh with polynomial orders p in the x-direction.

(b) Final *hp*-adapted mesh with polynomial orders p in the y-direction.

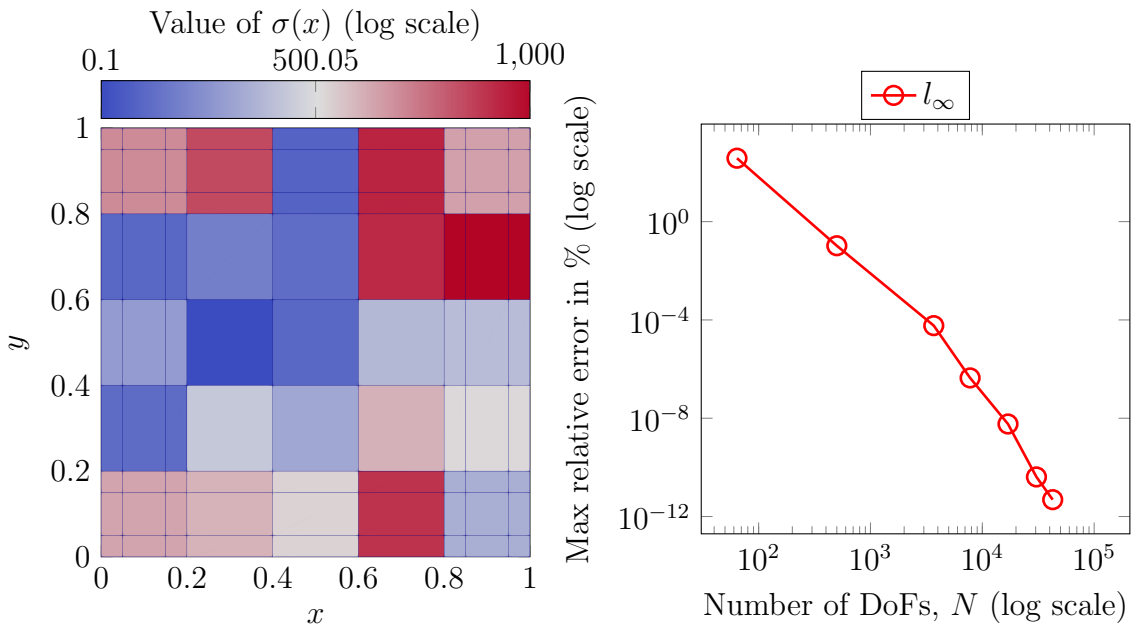

(c) Values for the materials in the domain.

(d) Evolution of $e_{\text{rel}}^{\max}$ in the process.

Figure 7.4.: *hp*-adapted meshes for our 1-sample wave propagation.

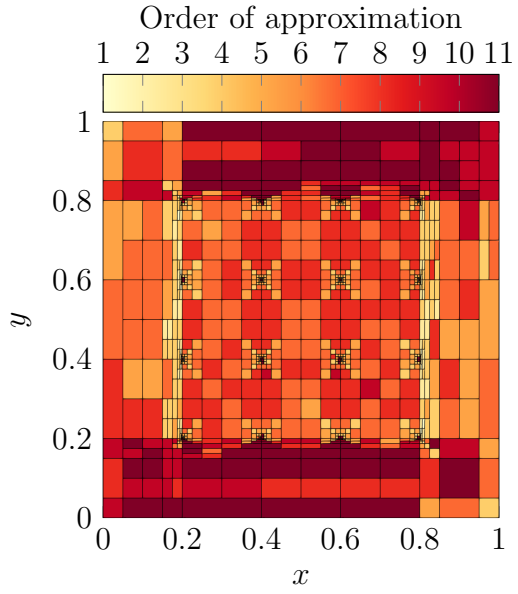

(a) Final *hp*-adapted mesh with polynomial orders p in the x-direction.

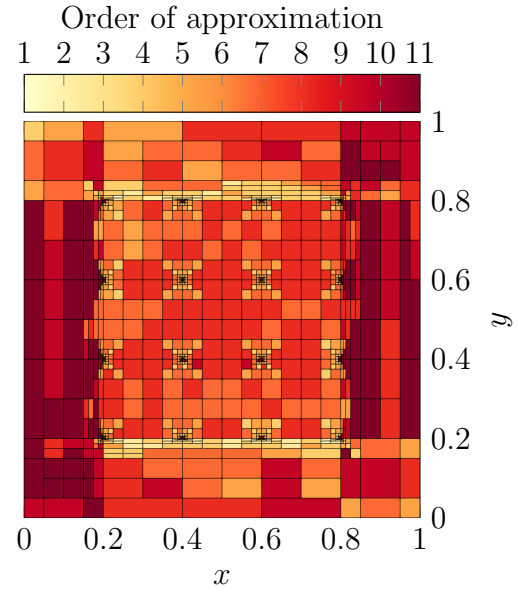

(b) Final *hp*-adapted mesh with polynomial orders p in the y-direction.

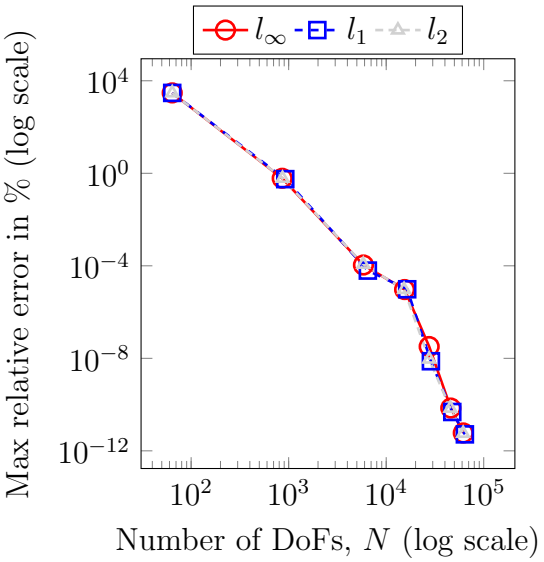

(c) Evolution of $e_{\text{rel}}^{\text{max}}$ in the process.

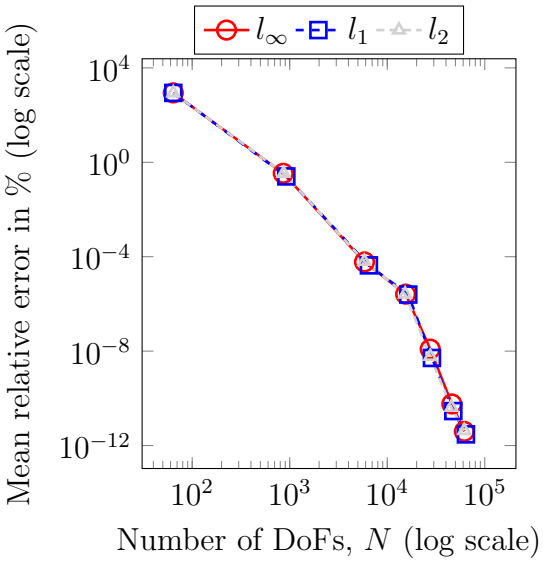

(d) Evolution of $e_{\text{rel}}^{\text{mean}}$ in the process.

Figure 7.5.: *hp*-adapted meshes for our 5-sample wave propagation.

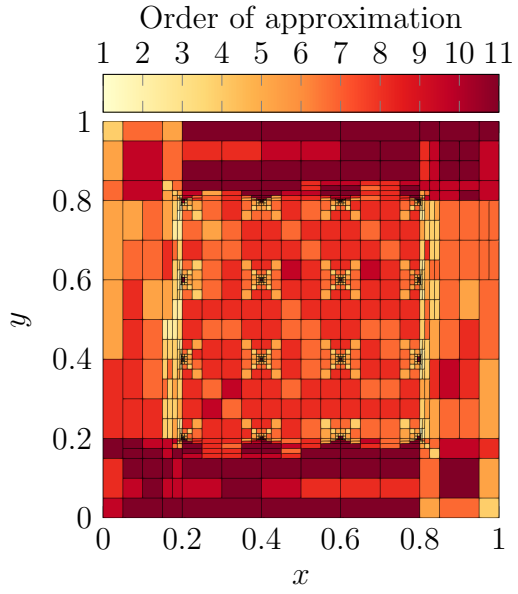

(a) Final *hp*-adapted mesh with polynomial orders p in the x-direction.

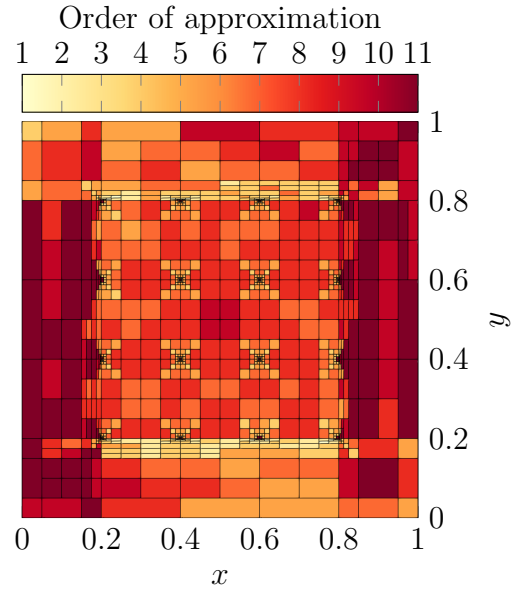

(b) Final *hp*-adapted mesh with polynomial orders p in the y-direction.

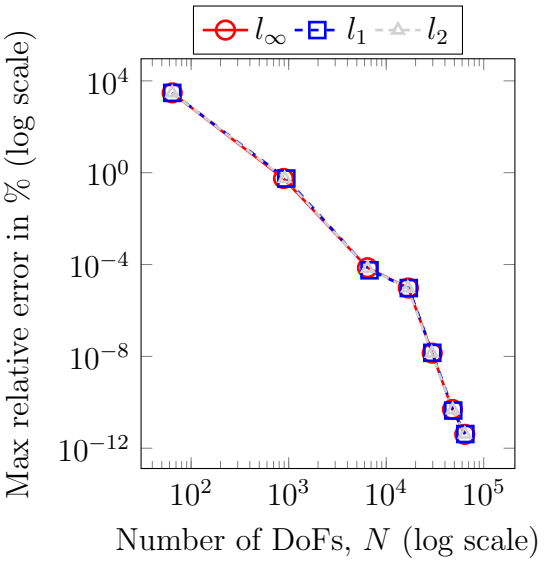

(c) Evolution of $e_{\text{rel}}^{\text{max}}$ in the process.

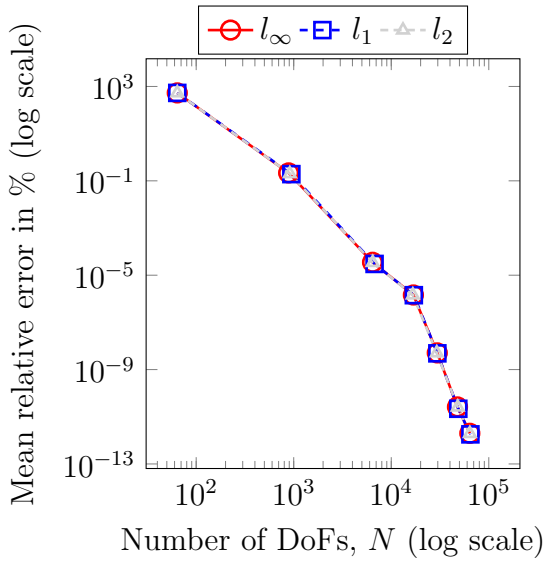

(d) Evolution of $e_{\text{rel}}^{\text{mean}}$ in the process.

Figure 7.6.: *hp*-adapted meshes for our 10-sample wave propagation.

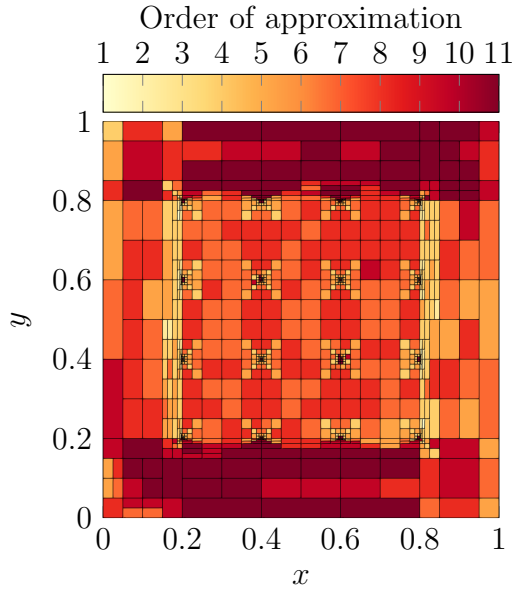

(a) Final *hp*-adapted mesh with polynomial orders p in the x-direction.

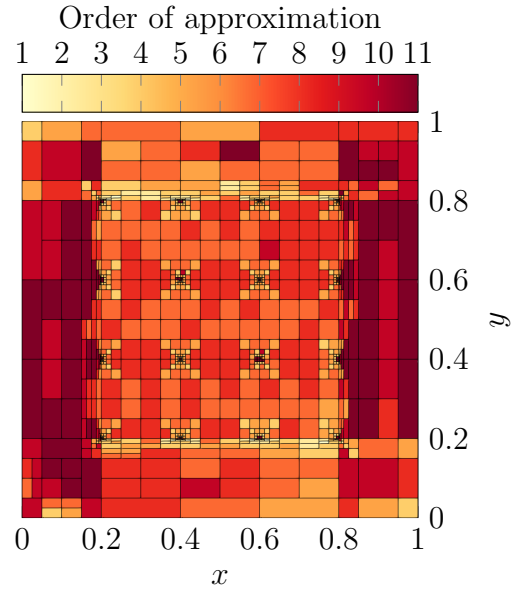

(b) Final *hp*-adapted mesh with polynomial orders p in the y-direction.

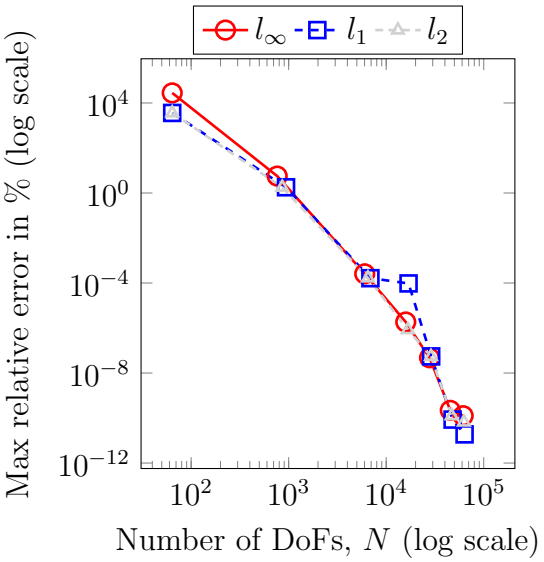

(c) Evolution of $e_{\text{rel}}^{\text{max}}$ in the process.

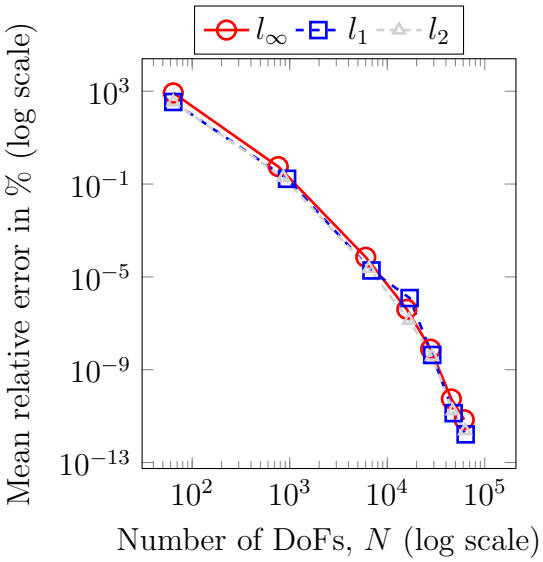

(d) Evolution of $e_{\text{rel}}^{\text{mean}}$ in the process.

Figure 7.7.: *hp*-adapted meshes for our 100-sample wave propagation.

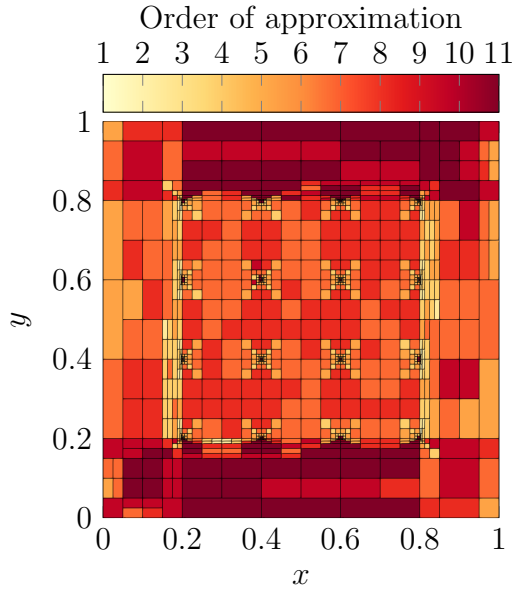

(a) Final *hp*-adapted mesh with polynomial orders p in the x-direction.

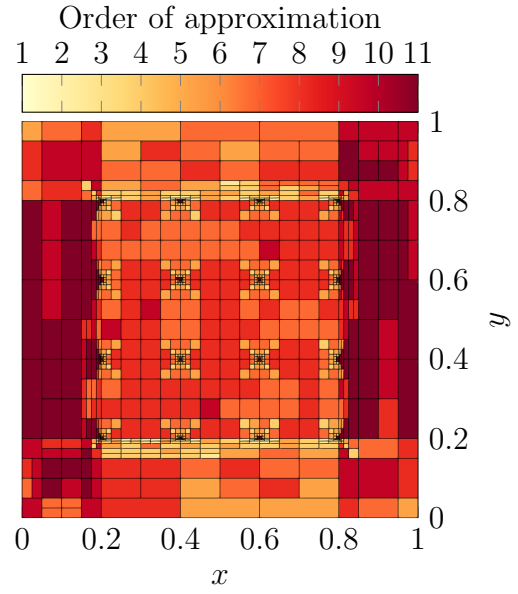

(b) Final *hp*-adapted mesh with polynomial orders p in the y-direction.

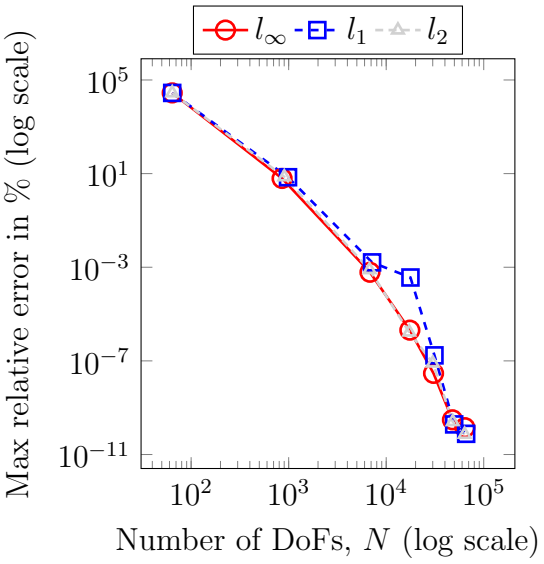

(c) Evolution of $e_{\text{rel}}^{\max}$ in the process.

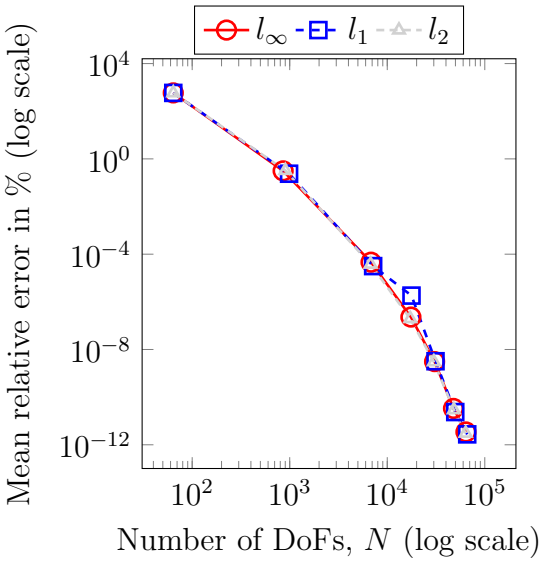

(d) Evolution of $e_{\text{rel}}^{\text{mean}}$ in the process.

Figure 7.8.: *hp*-adapted meshes for our 1000-sample wave propagation.

7.3.2.3. Wave propagation: accuracy

To showcase the efficiency of the MAGO approach, we present statistical properties of errors via standard box plots. These plots offer a detailed depiction of the error distribution. Tukey [186] introduced these box plots in 1977 to provide a robust data representation. The box plots visually represent how the maximum relative error in the QoI varies with different numbers of training samples for the adaptive process.

As shown in Figure 7.9, the box plots represent various values of S_{A} in the MAGO process. We consider the adaptive grids when they reach a maximum relative error, $e_{\mathrm{rel}}^{\max}$ that drops below 10^{-5}. Every number over each upper whisker represents the nDoF in each *hp* grid with the maximum relative error reduced to under 10^{-5}. The trend suggests that as the number of training samples for the adaptive process increases, the maximum relative error in the QoI tends to decrease or remain stable. The variation in relative errors becomes more confined with increasing training samples, as indicated by the tightening spread of the box plots.

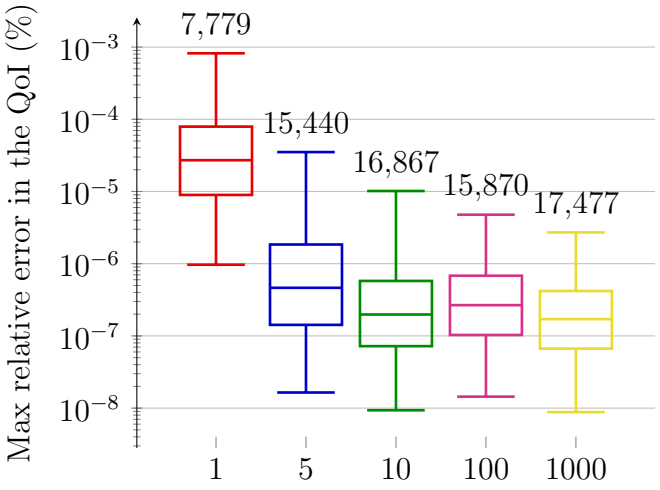

Figure 7.9.: Box plots for **different adaptive grids** with a threshold maximum relative error set at 10^{-5}.

7.3.2.4. Wave propagation: computational costs

We estimate the computational cost based on the factorization cost, which constitutes the most resource-intensive part of data generation and a significant expense in many FEM codes. In Tables 7.1 and 7.2, we approximate the computational

expenses in terms of Floating Point Operations (FLOPs) associated with database generation using the SAGO and MAGO approaches. We compute C^{SAGO} using Equation (7.27). The maximum relative error is constrained to be under 10^{-5}.

We observe that the MAGO approach is more cost-effective for solving problems in this case, as $C^{\mathrm{MAGO}} < C^{\mathrm{SAGO}}$. The median values of the maximum relative error are below 10^{-6}, indicating a significantly higher accuracy by one order of magnitude in the results, and demonstrated in Figure 7.9. This increased accuracy is achieved at a reduced cost, making the MAGO approach particularly suitable for solving challenging problems.

Number of DoF	C^{SAGO}			
	S_{G}			
$N_{\mathrm{f}}^{\mathrm{sago}}$	10^5	10^7	10^9	10^{11}
41259	$8.4238 \cdot 10^{11}$	$8.4238 \cdot 10^{13}$	$8.4238 \cdot 10^{15}$	$8.4238 \cdot 10^{17}$

Table 7.1.: The computational cost based on the factorization cost of generating the database using the SAGO strategy.

	Number of DoF		C^{MAGO}			
			S_{G}			
S_{A}	$N_{\mathrm{c}}^{\mathrm{mago}}$	$N_{\mathrm{f}}^{\mathrm{mago}}$	10^5	10^7	10^9	10^{11}
5	15440	52351	$1.9191 \cdot 10^{11}$	$1.9185 \cdot 10^{13}$	$1.9185 \cdot 10^{15}$	$1.9185 \cdot 10^{17}$
10	16867	57171	$2.1919 \cdot 10^{11}$	$2.1906 \cdot 10^{13}$	$2.1906 \cdot 10^{15}$	$2.1906 \cdot 10^{17}$
100	15870	53661	$2.0117 \cdot 10^{11}$	$1.9994 \cdot 10^{13}$	$1.9992 \cdot 10^{15}$	$1.9992 \cdot 10^{17}$
1000	17477	60381	$2.4588 \cdot 10^{11}$	$2.3120 \cdot 10^{13}$	$2.3105 \cdot 10^{15}$	$2.3105 \cdot 10^{17}$

Table 7.2.: The computational cost based on the factorization cost of generating the database using the MAGO strategy.

7.3.3. Poisson example

We consider the following elliptic problem based on the Poisson equation.

> Find u such that
>
> $$-\nabla \cdot (\sigma(\boldsymbol{x}) \nabla u) = 1 \text{ in } \Omega, \tag{7.31}$$
> $$u = 0 \text{ on } \partial\Omega. \tag{7.32}$$

7.3.3.1. Example: cross-shaped domain Poisson problem

We address a Poisson problem over a domain Ω in a two-dimensional space, represented on a 5×5 grid. The domain Ω resembles a cross and is defined by $\Omega = \left([0,1] \times \left[\frac{1}{5}, \frac{4}{5}\right]\right) \cup \left(\left[\frac{1}{5}, \frac{4}{5}\right] \times [0,1]\right)$. Please refer to Figure 7.10 to visualize the domain. Within this domain, there are two notable regions: Ω_f, the source area, and Ω_l, the QoI area. Both Ω_f and Ω_l are subregions within Ω. Specifically, Ω_f is the square defined by $x \in \left[\frac{1}{5}, \frac{2}{5}\right]$ and $y \in \left[\frac{1}{5}, \frac{2}{5}\right]$, and Ω_l is the square with $x \in \left[\frac{3}{5}, \frac{4}{5}\right]$ and $y \in \left[\frac{3}{5}, \frac{4}{5}\right]$. The origin of the coordinate system is the bottom-left corner of the domain.

Figures 7.11a and 7.11b showcase the absolute values of forward and adjoint numerical solutions, respectively, on a logarithmic scale.

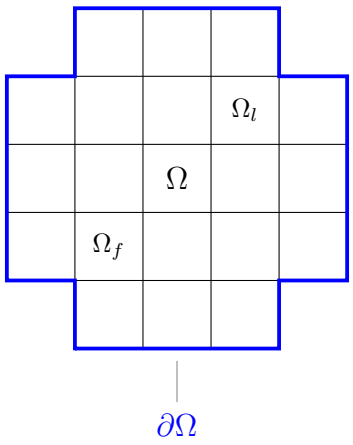

Figure 7.10.: Computational domain Ω, where homogeneous Dirichlet boundary conditions are imposed on $\partial\Omega$. Additionally, we define Ω_l as the support of the QoI $l(\phi)$, and Ω_f as the support of the source function.

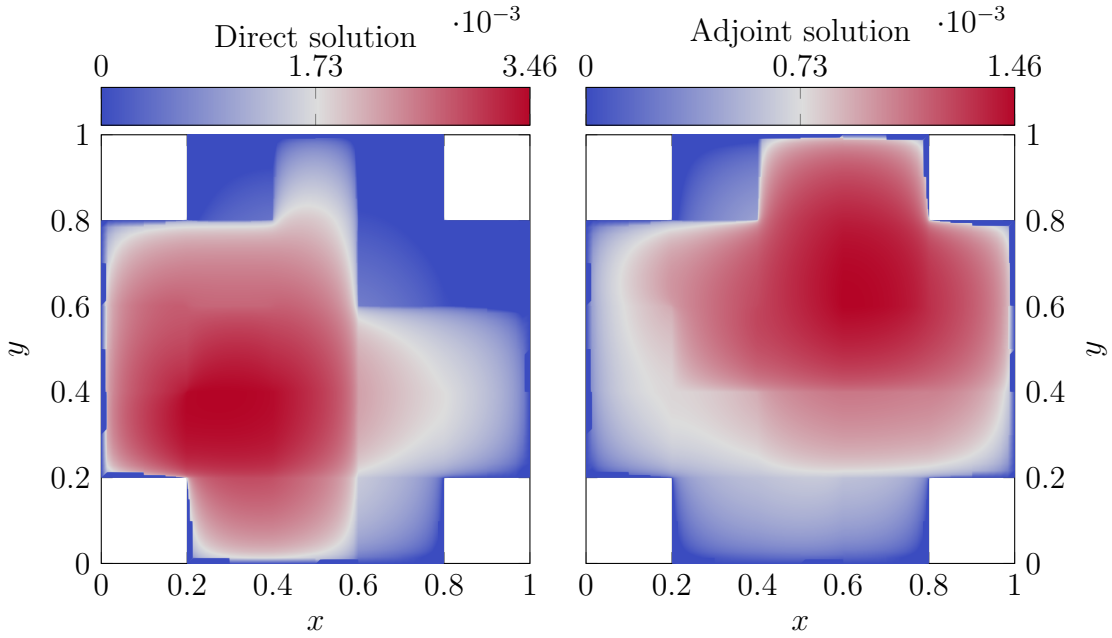

(a) Solution to the direct problem.

(b) Solution to the adjoint problem.

Figure 7.11.: Absolute value of the solutions of our cross-shaped domain Poisson example.

7.3.3.2. Cross-shaped domain Poisson: convergence

We present the numerical results for our MAGO process with one sample in Figure 7.12, and for S_{A} equal to 5, 10, 50, and 100 in Figures 7.13 to 7.16, respectively. The convergence is quasi-optimal, and the three norms (l_1, l_2, and l_∞) yield similar results as in previous examples. Predictably, regions with significant material coefficient fluctuations witness more substantial mesh refinement, resulting in more compact mesh elements (denoted as h) near intersections of multiple materials. In addition, Figure 7.12c represents the material properties. The quasi-optimal exponential convergence graph for this scenario, along with the progress of $e_{\mathrm{rel}}^{\mathrm{max}}$ and $e_{\mathrm{rel}}^{\mathrm{mean}}$, can be found in Figure 7.12d.

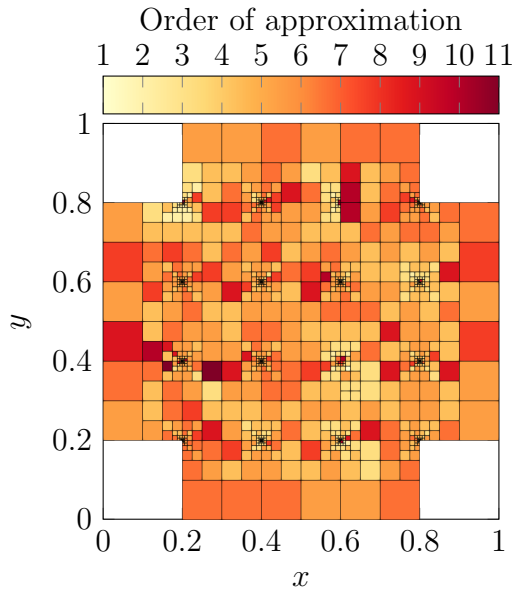

(a) Final *hp*-adapted mesh with polynomial orders p in the x-direction.

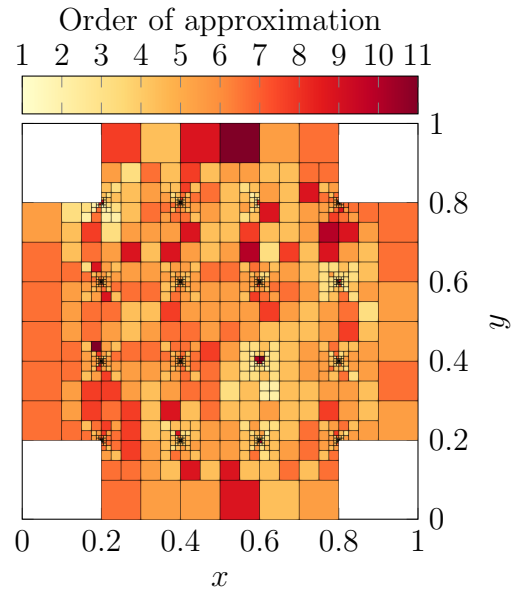

(b) Final *hp*-adapted mesh with polynomial orders p in the y-direction.

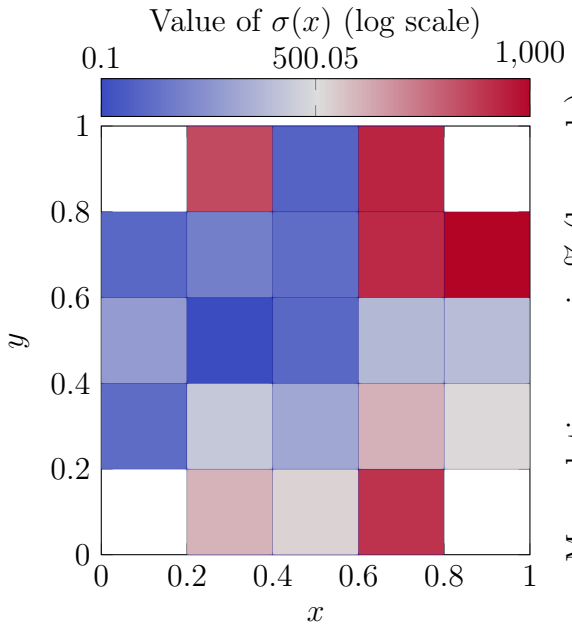

(c) Values for the materials in the domain.

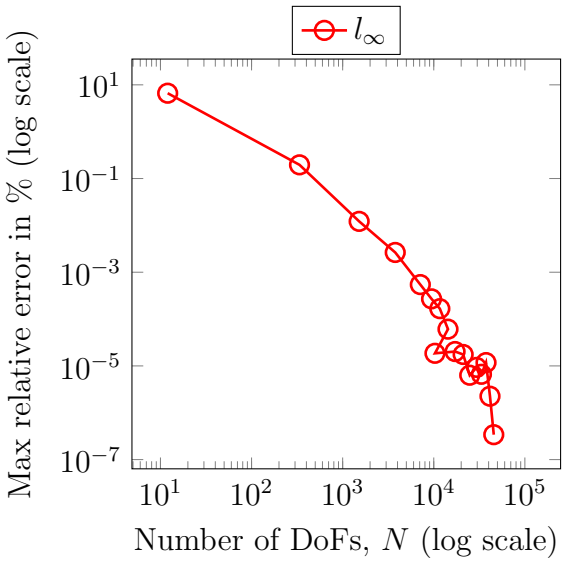

(d) Evolution of $e_{\text{rel}}^{\max}$ in the process.

Figure 7.12.: *hp*-adapted meshes for our 1-sample cross-shaped domain example.

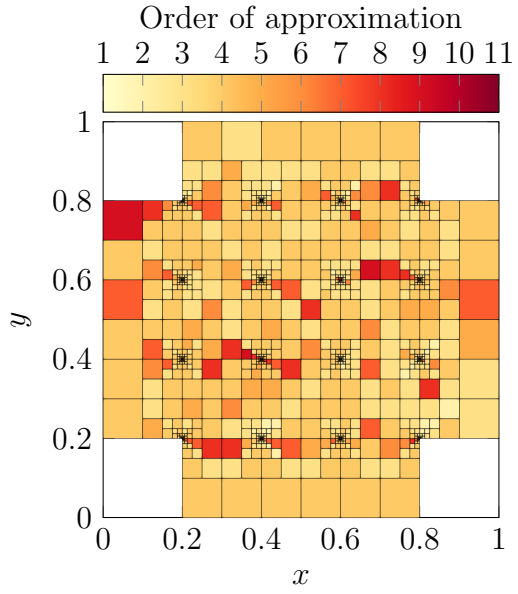

(a) Final *hp*-adapted mesh with polynomial orders p in the x-direction.

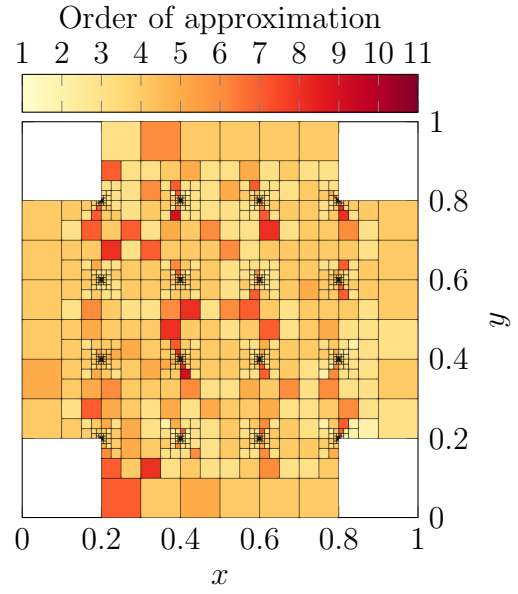

(b) Final *hp*-adapted mesh with polynomial orders p in the y-direction.

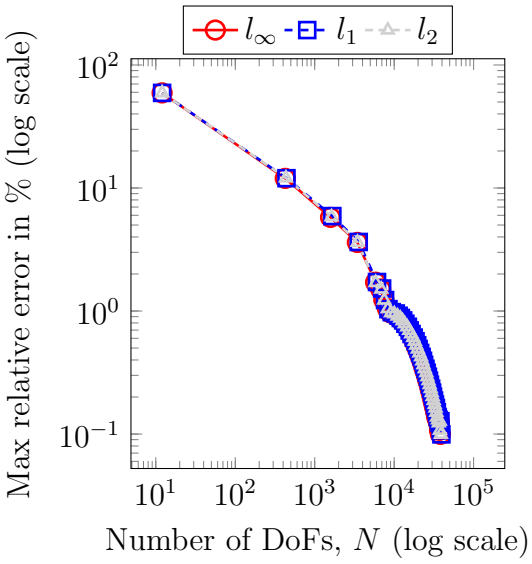

(c) Evolution of $e_{\text{rel}}^{\text{max}}$ in the process.

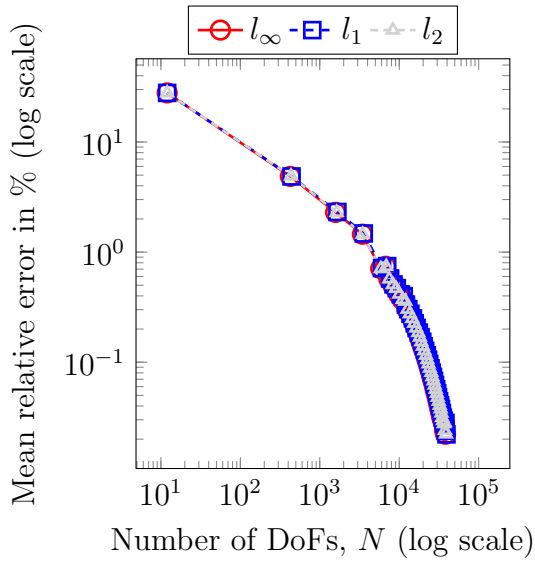

(d) Evolution of $e_{\text{rel}}^{\text{mean}}$ in the process.

Figure 7.13.: *hp*-adapted meshes for our 5-sample cross-shaped domain example.

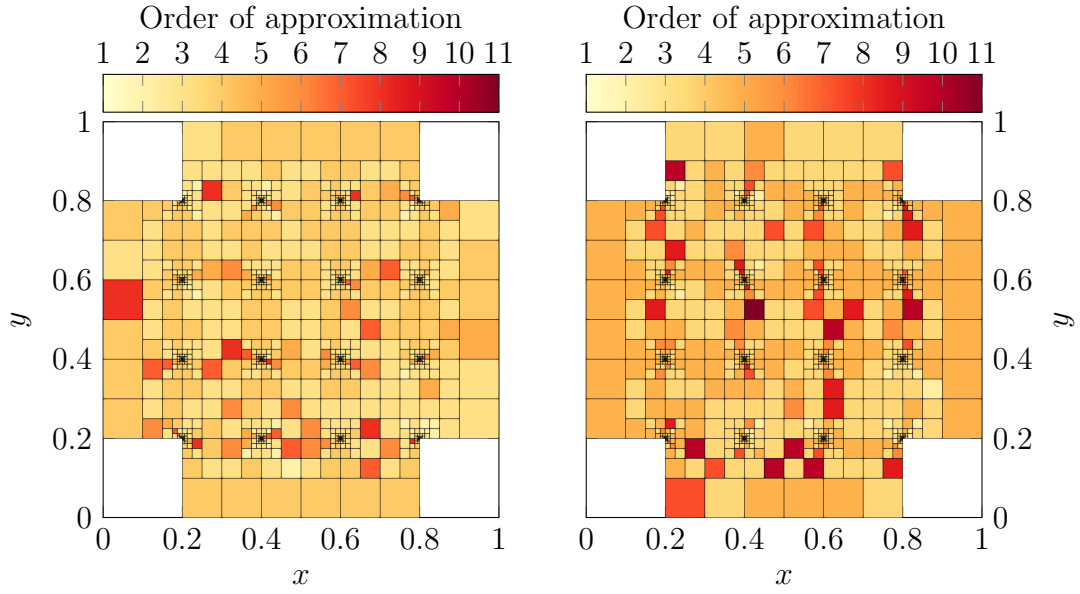

(a) Final *hp*-adapted mesh with polynomial orders p in the x-direction.

(b) Final *hp*-adapted mesh with polynomial orders p in the y-direction.

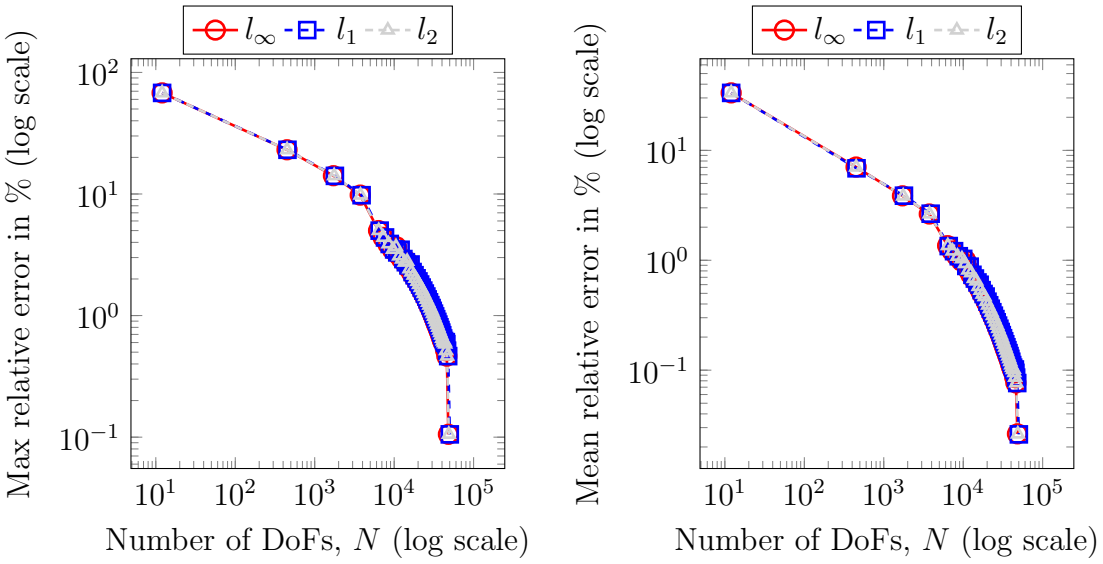

(c) Evolution of $e_{\text{rel}}^{\max}$ in the process.

(d) Evolution of $e_{\text{rel}}^{\text{mean}}$ in the process.

Figure 7.14.: *hp*-adapted meshes for our 10-sample cross-shaped domain example.

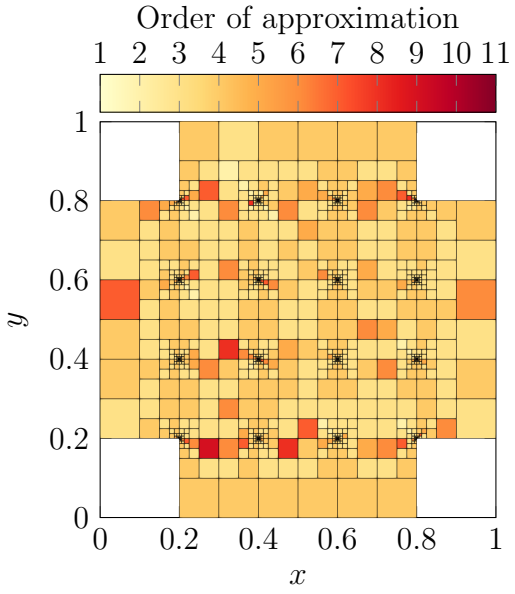

(a) Final *hp*-adapted mesh with polynomial orders p in the x-direction.

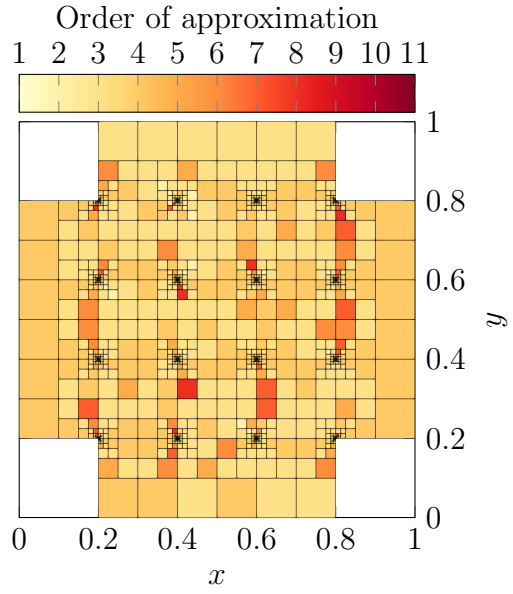

(b) Final *hp*-adapted mesh with polynomial orders p in the y-direction.

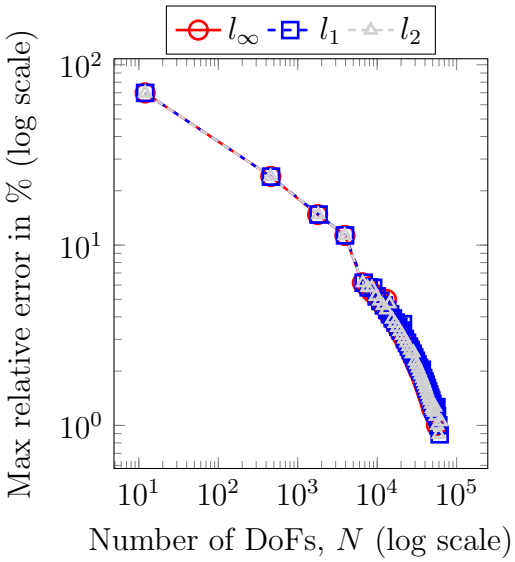

(c) Evolution of $e_{\text{rel}}^{\text{max}}$ in the process.

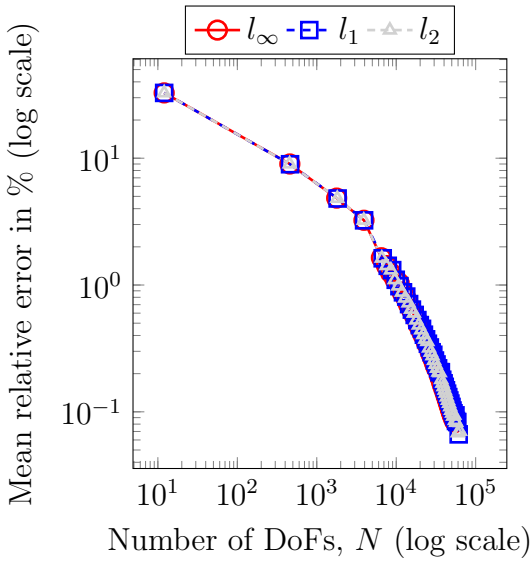

(d) Evolution of $e_{\text{rel}}^{\text{mean}}$ in the process.

Figure 7.15.: *hp*-adapted meshes for our 50-sample cross-shaped domain example.

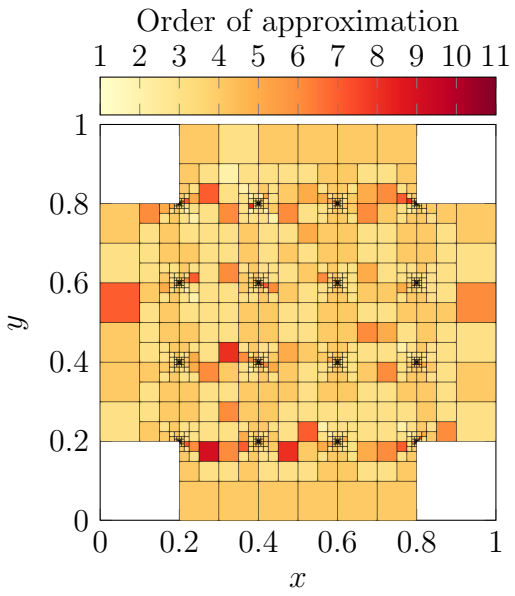

(a) Final *hp*-adapted mesh with polynomial orders p in the x-direction.

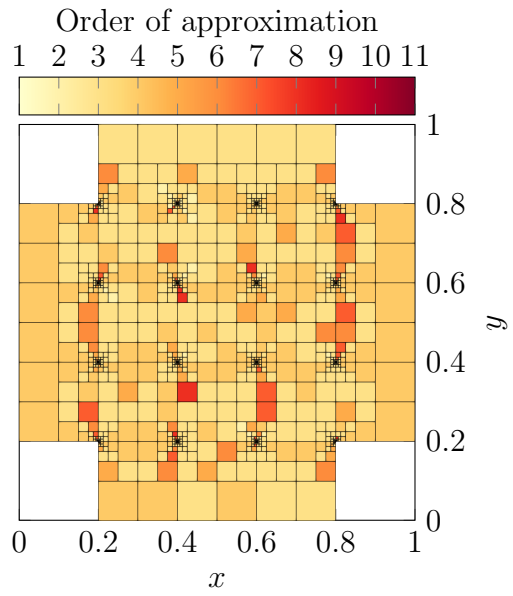

(b) Final *hp*-adapted mesh with polynomial orders p in the y-direction.

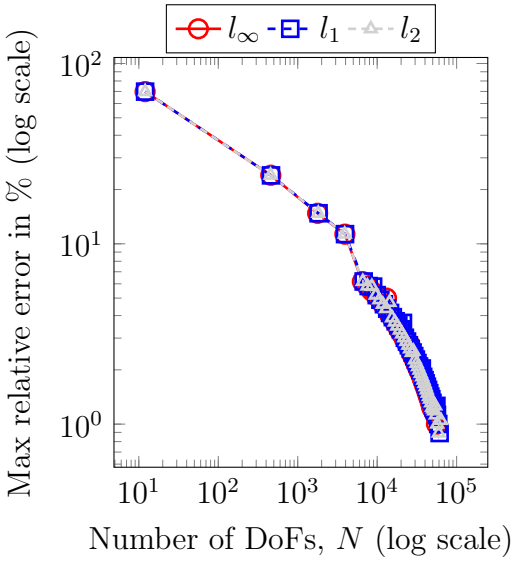

(c) Evolution of $e_{\text{rel}}^{\text{max}}$ in the process.

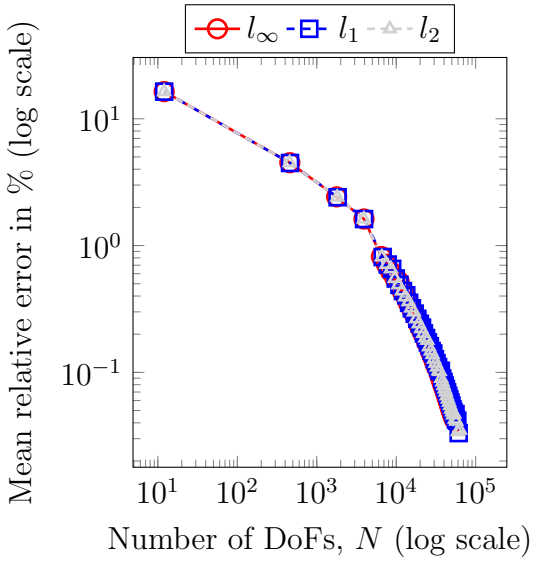

(d) Evolution of $e_{\text{rel}}^{\text{mean}}$ in the process.

Figure 7.16.: *hp*-adapted meshes for our 100-sample cross-shaped domain example.

7.3.3.3. Cross-shaped domain Poisson: accuracy

Figure 7.17 displays a series of box plots corresponding to different adaptive grids. The x-axis denotes the number of samples (S_{A}) used during the MAGO process to formulate the final *hp* grid. We stop every MAGO adaptation once the maximum relative error ($e_{\mathrm{rel}}^{\max}$) is reduced to under 1.0%. Every number over each upper whisker represents the nDoF in each *hp* grid with the maximum relative error reduced to under 1.0%. The general trend suggests that as the number of training samples for the adaptive process increases, the maximum relative error in the QoI tends to decrease. The spread of relative errors becomes greater with more training samples. However, the median error values do not change dramatically after fifty training samples, suggesting decreasing returns in error reduction with additional samples.

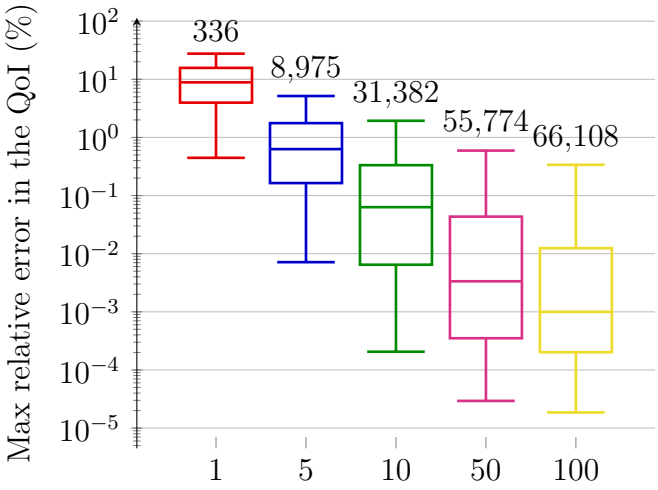

Figure 7.17.: Box plots for **different adaptive grids** with a threshold maximum relative error set at 1.0%.

7.3.3.4. Cross-shaped domain Poisson: computational costs

In Tables 7.3 and 7.4, we approximate the computational expenses in terms of FLOPs associated with database generation using the SAGO and MAGO approaches. We compute C^{SAGO} using Equation (7.27). The maximum relative error is constrained to be under 1.0%.

While solving problems using the SAGO approach appears to be cost-effective, it is essential to acknowledge a limitation, as $C^{\mathrm{SAGO}} < C^{\mathrm{MAGO}}$.

Number of DoF	C^{SAGO}			
	S_{G}			
$N_{\text{f}}^{\text{sago}}$	10^5	10^7	10^9	10^{11}
23494	$5.1131 \cdot 10^{11}$	$5.1131 \cdot 10^{13}$	$5.1131 \cdot 10^{15}$	$5.1131 \cdot 10^{17}$

Table 7.3.: The computational cost based on the factorization cost of generating the database using the SAGO strategy.

	Number of DoF		C^{MAGO}			
			S_{G}			
S_{A}	$N_{\text{c}}^{\text{mago}}$	$N_{\text{f}}^{\text{mago}}$	10^5	10^7	10^9	10^{11}
5	8975	77651	$8.5134 \cdot 10^{10}$	$8.5027 \cdot 10^{12}$	$8.5026 \cdot 10^{14}$	$8.5026 \cdot 10^{16}$
10	31382	362543	$5.5811 \cdot 10^{11}$	$5.5595 \cdot 10^{13}$	$5.5593 \cdot 10^{15}$	$5.5593 \cdot 10^{17}$
50	55774	637779	$1.3427 \cdot 10^{12}$	$1.3174 \cdot 10^{14}$	$1.3172 \cdot 10^{16}$	$1.3172 \cdot 10^{18}$
100	66108	734061	$1.7626 \cdot 10^{12}$	$1.7004 \cdot 10^{14}$	$1.6997 \cdot 10^{16}$	$1.6997 \cdot 10^{18}$

Table 7.4.: The computational cost based on the factorization cost of generating the database using the MAGO strategy.

7.3.3.5. Example: grid-based domain Poisson problem

We use a 5×5 grid to represent the material properties within a computational domain defined in Section 7.3.2.1. Figure 7.2 displays this domain. Figures 7.18a and 7.18b display the absolute values of the forward and adjoint numerical solutions, respectively, on a logarithmic scale.

7.3.3.6. Grid-based domain Poisson: convergence

Figure 7.19 displays the computational outcomes for the grid-based domain Poisson example when employing one sample for its adaptive routine, corresponding to the GOA approach described in [43, 44]. Figures 7.19a and 7.19b show the final *hp*-adapted mesh for this example, whereas Figure 7.19c maps out the domain's material coefficient layout. As anticipated, areas with pronounced material coefficient disparities require from intense refinements. Consequently, mesh sizes, denoted by h, are finer at junctures where diverse materials intersect. Figure 7.19d shows a quasi-exponential convergence pattern. As depicted in Figure 7.19d, it distinctly illustrates that an increased number of samples in the adaptive process (S_{A}) leads to improved convergence behavior. For instance, Figures 7.20 to 7.23 encapsulate findings when S_{A} is assigned values of 5, 10, 50, and 100.

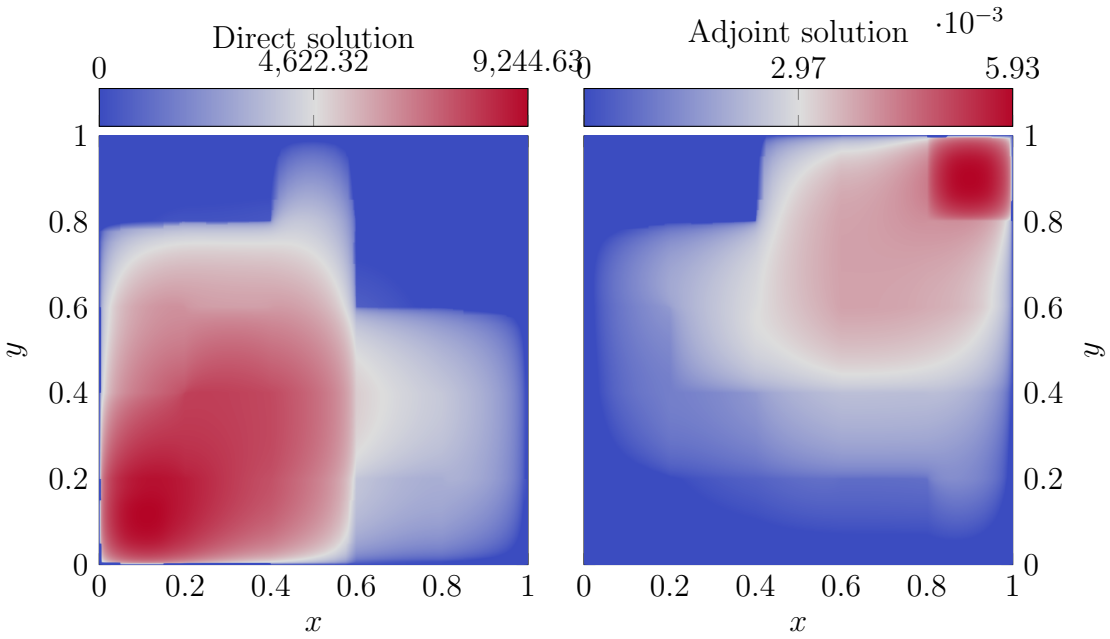

(a) Solution to the direct problem.

(b) Solution to the adjoint problem.

Figure 7.18.: Absolute value of the solutions of our Poisson example.

Drawing from the observations, MAGO's adaptive strategy showcases a quasi-optimal convergence rate. As samples for the adaptive routine increase, ensuring precision on a unified *hp* grid for all samples grows complex. Hence, while we observe quasi-optimal convergence rates consistently, the relative errors are amplified as S_{A} rises.

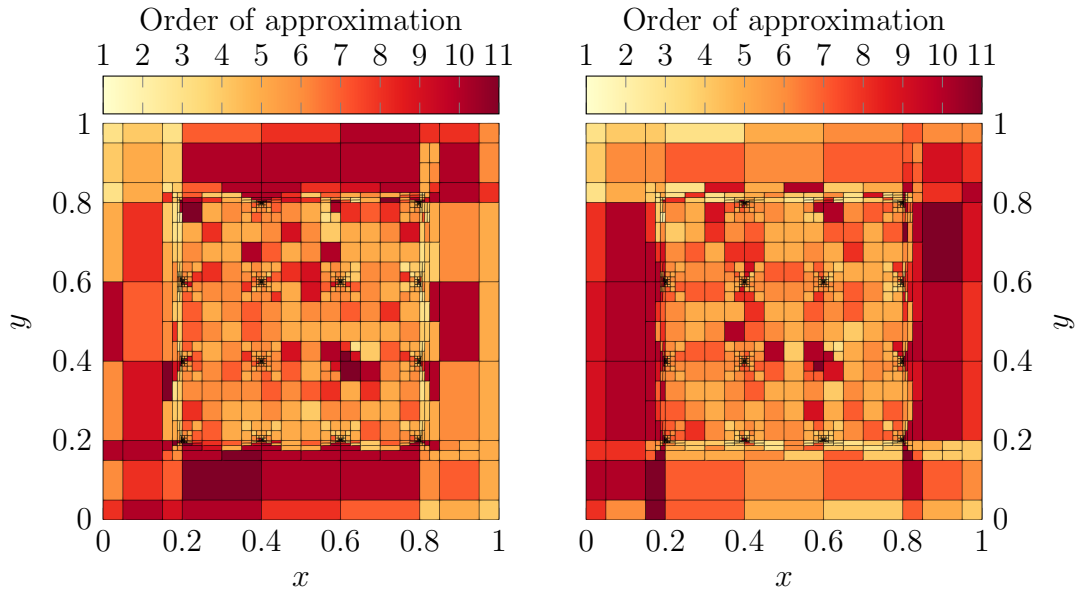

(a) Final *hp*-adapted mesh with polynomial orders p in the x-direction.

(b) Final *hp*-adapted mesh with polynomial orders p in the y-direction.

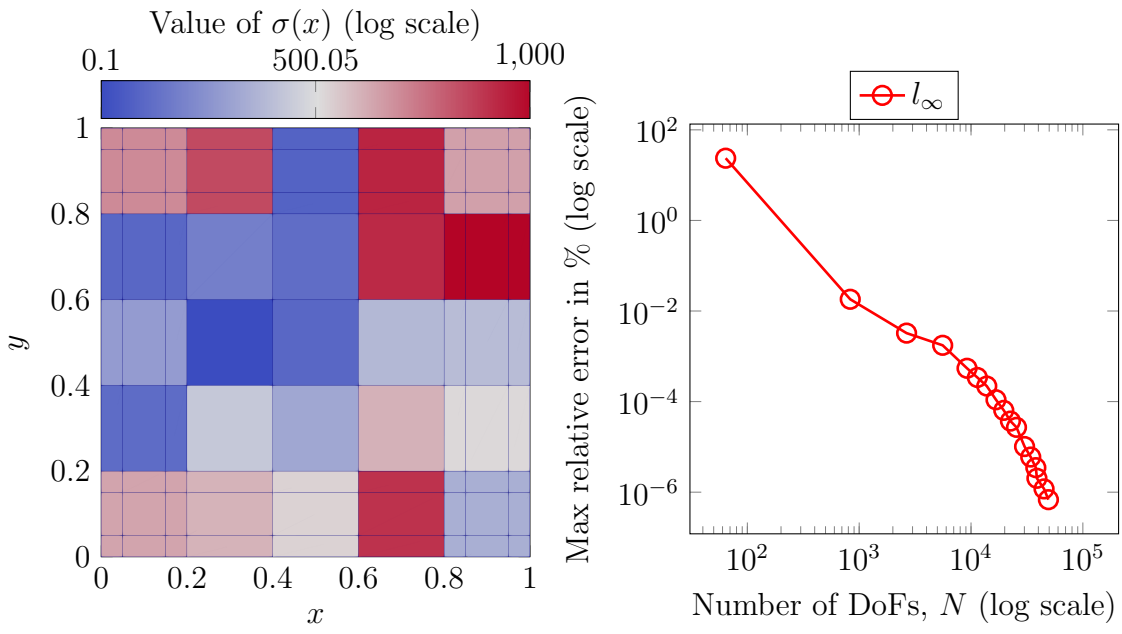

(c) Values for the materials in the domain.

(d) Evolution of $e_{\text{rel}}^{\max}$ in the process.

Figure 7.19.: *hp*-adapted meshes for our 1-sample grid-based domain example.

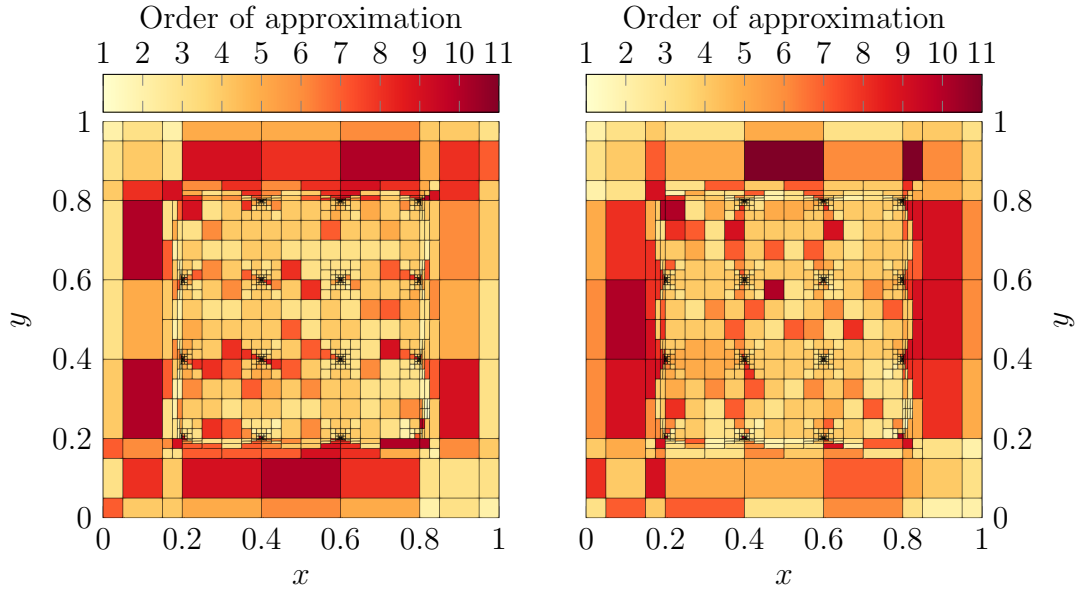

(a) Final *hp*-adapted mesh with polynomial orders p in the x-direction.

(b) Final *hp*-adapted mesh with polynomial orders p in the y-direction.

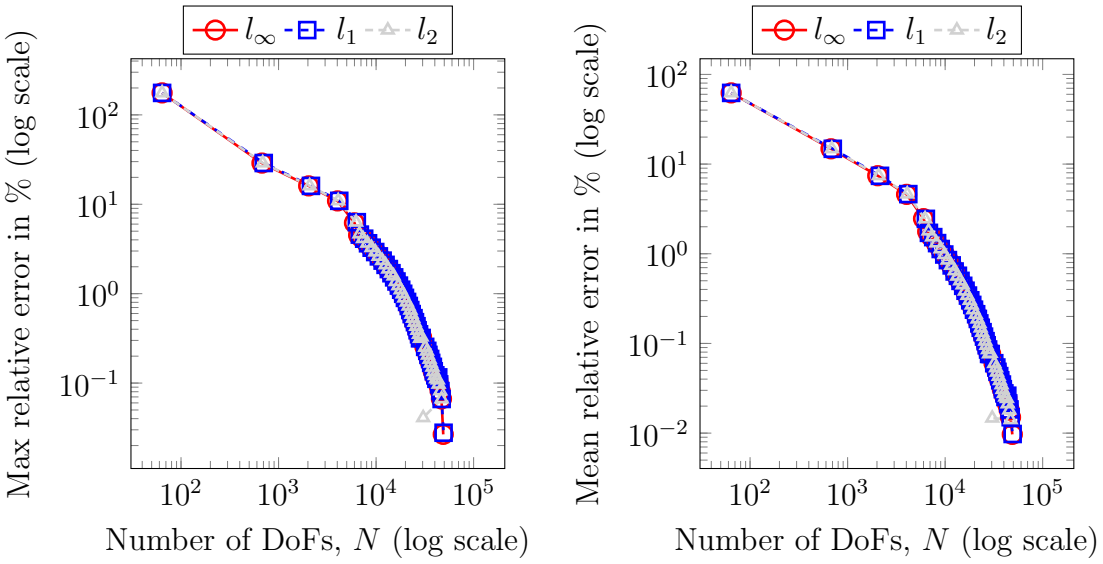

(c) Evolution of $e_{\text{rel}}^{\text{max}}$ in the process.

(d) Evolution of $e_{\text{rel}}^{\text{mean}}$ in the process.

Figure 7.20.: *hp*-adapted meshes for our 5-sample grid-based domain example.

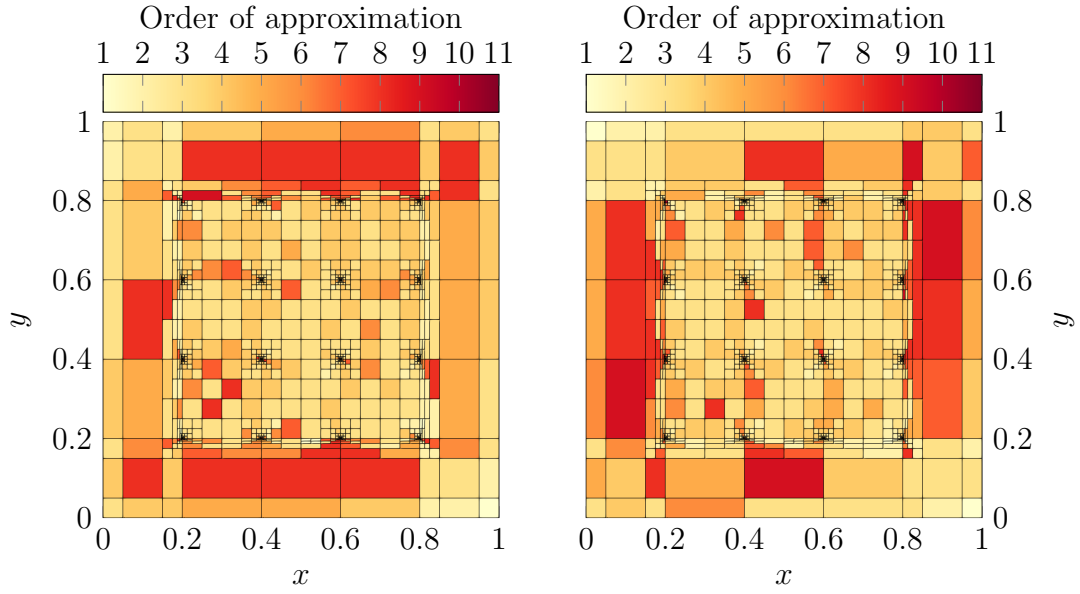

(a) Final *hp*-adapted mesh with polynomial orders p in the x-direction.

(b) Final *hp*-adapted mesh with polynomial orders p in the y-direction.

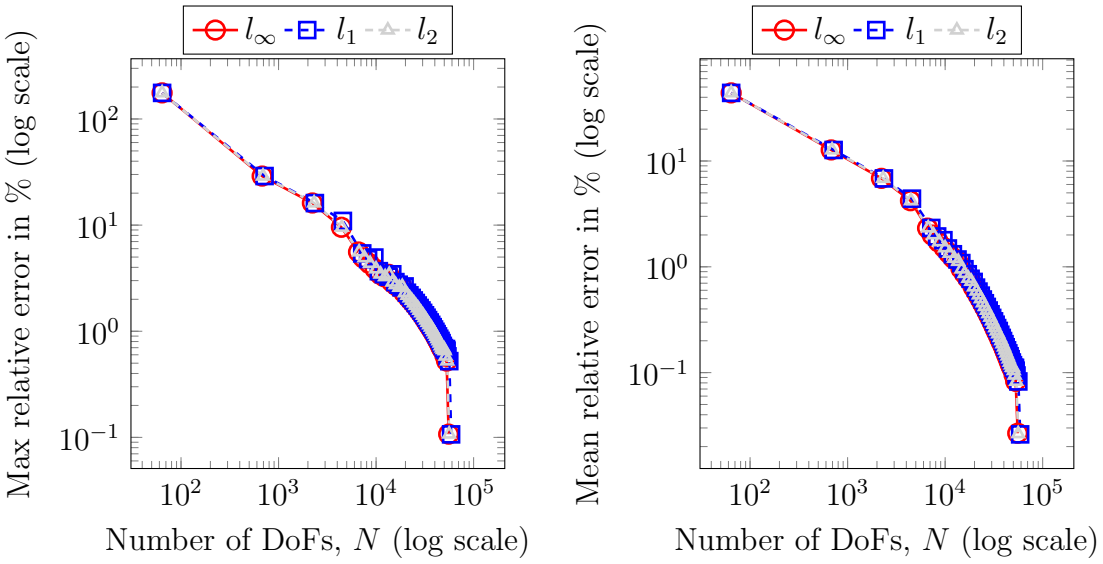

(c) Evolution of $e_{\text{rel}}^{\text{max}}$ in the process.

(d) Evolution of $e_{\text{rel}}^{\text{mean}}$ in the process.

Figure 7.21.: *hp*-adapted meshes for our 10-sample grid-based domain example.

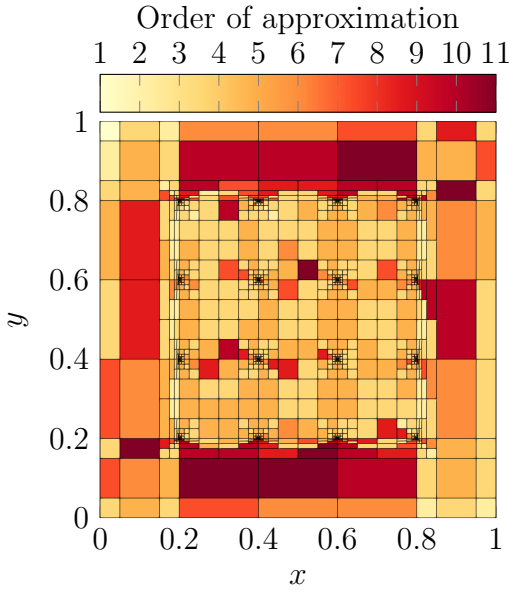

(a) Final *hp*-adapted mesh with polynomial orders p in the x-direction.

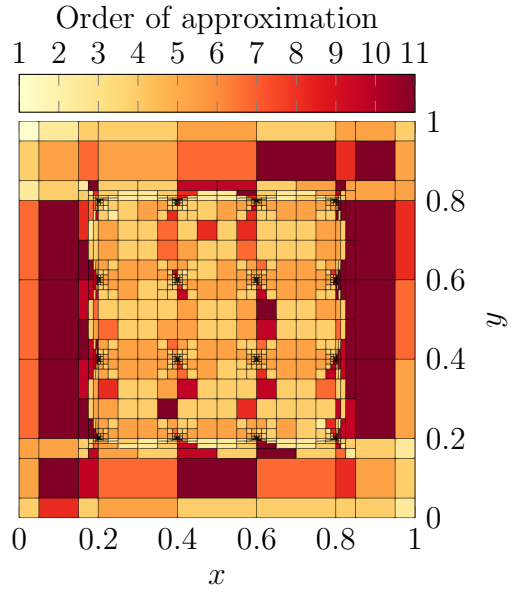

(b) Final *hp*-adapted mesh with polynomial orders p in the y-direction.

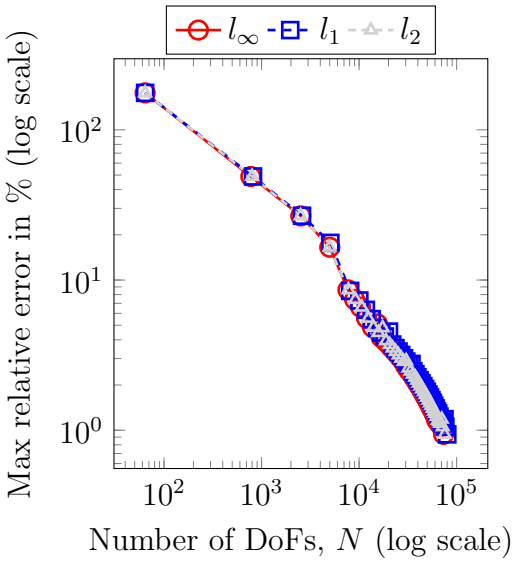

(c) Evolution of $e_{\text{rel}}^{\text{max}}$ in the process.

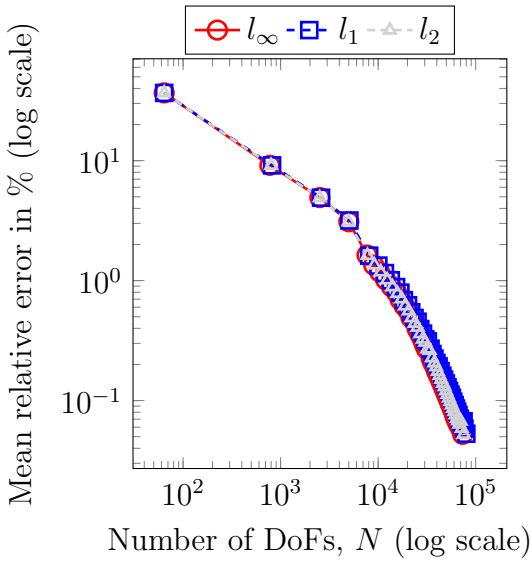

(d) Evolution of $e_{\text{rel}}^{\text{mean}}$ in the process.

Figure 7.22.: *hp*-adapted meshes for our 50-sample grid-based domain example.

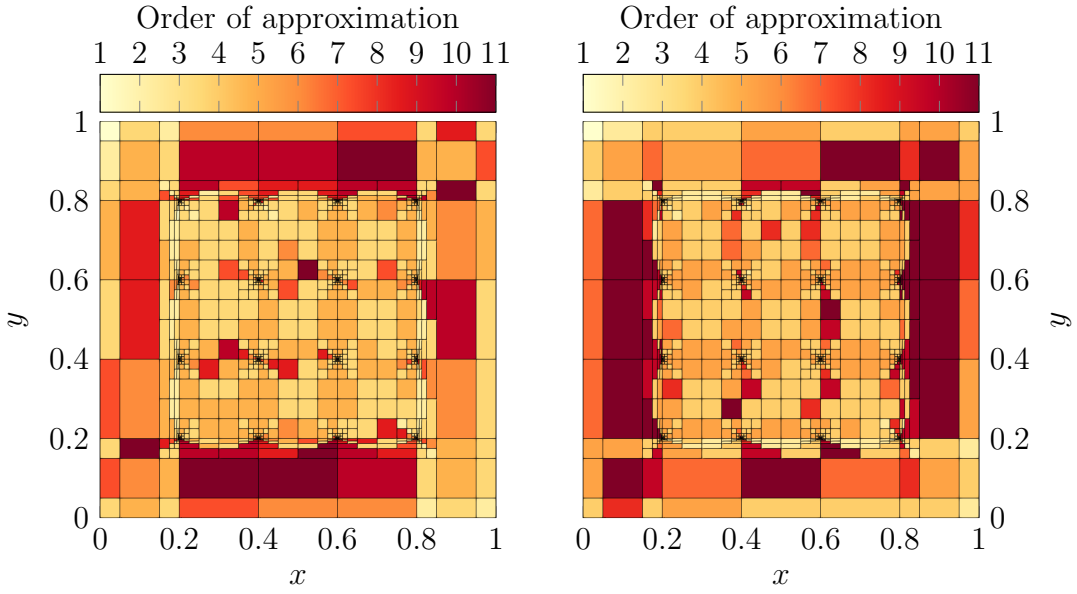

(a) Final *hp*-adapted mesh with polynomial orders p in the x-direction.

(b) Final *hp*-adapted mesh with polynomial orders p in the y-direction.

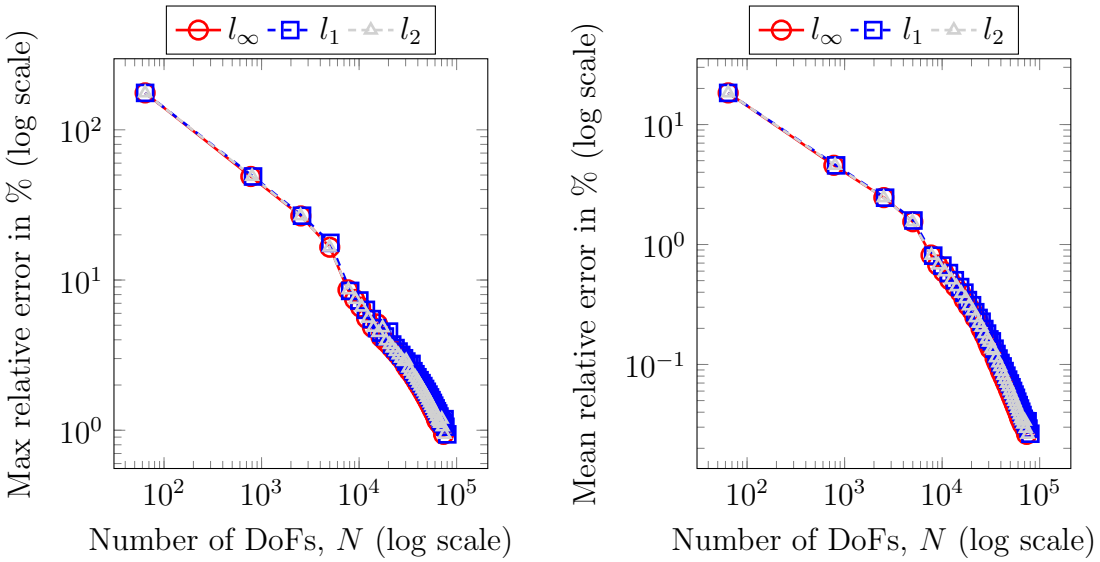

(c) Evolution of $e_{\text{rel}}^{\text{max}}$ in the process.

(d) Evolution of $e_{\text{rel}}^{\text{mean}}$ in the process.

Figure 7.23.: *hp*-adapted meshes for our 100-sample grid-based domain example.

7.3.3.7. Grid-based domain Poisson: accuracy

Figure 7.24 displays a series of box plots corresponding to different adaptive grids. The x-axis denotes the number of samples (S_{A}) used during the MAGO process to formulate the final *hp* grid. We stop every MAGO adaptation once the maximum relative error ($e_{\mathrm{rel}}^{\mathrm{max}}$) is reduced to under 1.0%. Every number over each upper whisker represents the nDoF in each *hp* grid with the maximum relative error reduced to under 1.0%. The general trend suggests that as the number of training samples for the adaptive process increases, the maximum relative error in the QoI tends to decrease. The spread of relative errors becomes greater with more training samples. However, the median error values do not change dramatically after fifty training samples, suggesting decreasing returns in error reduction with additional samples.

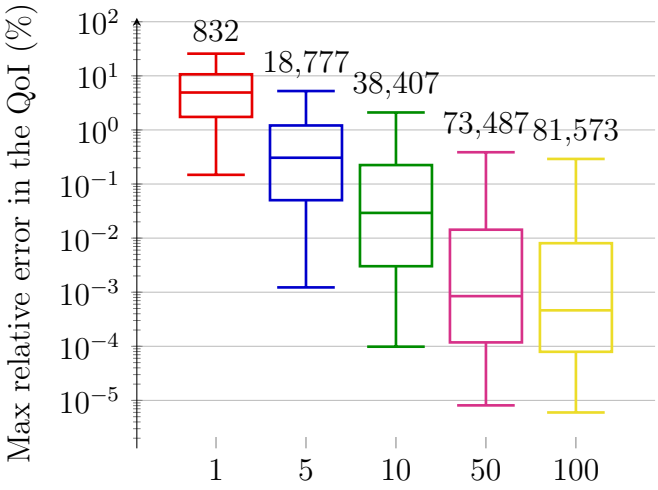

Figure 7.24.: Box plots for **different adaptive grids** with a threshold maximum relative error set at 1.0%

7.3.3.8. Grid-based domain Poisson: computational costs

In Tables 7.5 and 7.6, we approximate the computational expenses in terms of FLOPs associated with database generation using the SAGO and MAGO approaches. We compute C^{SAGO} using Equation (7.27). The maximum relative error is constrained to be under 1.0%.

While solving problems using the SAGO approach appears to be cost-effective, it is essential to acknowledge a limitation, as $C^{\mathrm{SAGO}} < C^{\mathrm{MAGO}}$.

Number of DoF	C^{SAGO}			
	S_{G}			
$N_{\mathrm{f}}^{\mathrm{sago}}$	10^5	10^7	10^9	10^{11}
28428	$6.4888 \cdot 10^{11}$	$6.4888 \cdot 10^{13}$	$6.4888 \cdot 10^{15}$	$6.4888 \cdot 10^{17}$

Table 7.5.: The computational cost based on the factorization cost of generating the database using the SAGO strategy.

	Number of DoF		C^{MAGO}			
			S_{G}			
A	$N_{\mathrm{c}}^{\mathrm{mago}}$	$N_{\mathrm{f}}^{\mathrm{mago}}$	10^5	10^7	10^9	10^{11}
5	18777	186161	$2.5770 \cdot 10^{11}$	$2.5730 \cdot 10^{13}$	$2.5730 \cdot 10^{15}$	$2.5730 \cdot 10^{17}$
10	38407	428635	$7.5550 \cdot 10^{11}$	$7.5272 \cdot 10^{13}$	$7.5269 \cdot 10^{15}$	$7.5269 \cdot 10^{17}$
50	73487	769965	$2.0259 \cdot 10^{12}$	$1.9925 \cdot 10^{14}$	$1.9921 \cdot 10^{16}$	$1.9921 \cdot 10^{18}$
100	81573	831627	$2.4056 \cdot 10^{12}$	$2.3306 \cdot 10^{14}$	$2.3298 \cdot 10^{16}$	$2.3298 \cdot 10^{18}$

Table 7.6.: The computational cost based on the factorization cost of generating the database using the MAGO strategy.

Part III.

Main achievements, conclusions and future work

8. Main Achievements

8.1. Peer-reviewed Publications

2023 F. V. Caro, V. Darrigrand, J. Alvarez-Aramberri, and D. Pardo. *A Multi-Adaptive-Goal-Oriented Strategy to Generate Massive Databases of Parametric PDEs.* To be submitted to *Computer Methods in Applied Mechanics and Engineering* in October 2023.

2022 F. V. Caro, V. Darrigrand, J. Alvarez-Aramberri, E. Alberdi, and D. Pardo. *A painless multi-level automatic goal-oriented hp-adaptive coarsening strategy for elliptic and non-elliptic problems. Computer Methods in Applied Mechanics and Engineering*, 401:115641, 2022. Impact Factor: 7.2, Quartile: Q1, Scimago Ranking.
`https://doi.org/10.1016/j.cma.2022.115641`

2022 F. V. Caro, V. Darrigrand, J. Alvarez-Aramberri, E. A. Celaya, and D. Pardo. *1D Painless Multi-level Automatic Goal-Oriented h and p Adaptive Strategies Using a Pseudo-Dual Operator.* In *Computational Science – ICCS 2022*, pages 347–357, 2022.
`https://doi.org/10.1007/978-3-031-08754-7_43`

8.2. International Conferences

2023 **F. V. Caro**, V. Darrigrand, J. Alvarez-Aramberri, and D. Pardo. *Generation of Massive Databases for Deep Learning Inversion Using A Goal-Oriented hp-Adaptive Strategy.*
XI International Conference on Adaptive Modeling and Simulation, Gothenburg, Sweden, [June 19-21, 2023].

2022 **F. V. Caro**, V. Darrigrand, J. Alvarez-Aramberri, E. Alberdi, and D. Pardo. *A Painless Automatic hp-Adaptive Coarsening Strategy For Non-SPD problems: A Goal-Oriented Approach.*
15th World Congress on Computational Mechanics and 8th Asian Pacific Congress on Computational Mechanics, Yokohama, Japan, [July 31 - August 5, 2022].

2022 **F. V. Caro**, V. Darrigrand, J. Alvarez-Aramberri, E. Alberdi, and D. Pardo. *1D Painless Multi-Level Automatic Goal-Oriented h and p Adaptive Strategies using a Pseudo-Dual Operator.*
22nd International Conference on Computational Science, London, United Kingdom, [June 21-23, 2022].

2022 **F. V. Caro**, V. Darrigrand, J. Alvarez-Aramberri, E. Alberdi, and D. Pardo. *Goal-Oriented hp-Adaptive Finite Element Methods: A Painless Multilevel Automatic Coarsening Strategy For Non-SPD Problems.*
8th European Congress on Computational Methods in Applied Sciences and Engineering, Oslo, Norway, [June 5-9, 2022].

2021 **F. V. Caro**, V. Darrigrand, E. Alberdi, and D. Pardo. *A Painless Goal-Oriented hp-Adaptive Strategy for Indefinite Problems.*
16th U.S. National Congress on Computational Mechanics, Chicago, U.S.A, [July 25-29, 2021].

2021 **F. V. Caro**, V. Darrigrand, E. Alberdi, and D. Pardo. *Goal-Oriented hp-Adaptive Finite Element Methods: A Painless Multi-level Automatic Coarsening Strategy.*
10th International Conference on Adaptive Modeling and Simulation, Gothenburg, Sweden, [June 21-23, 2021]. `https://doi.org/10.23967/admos.2021.044`.

2021 F. V. Caro, V. Darrigrand, **E. Alberdi**, and D. Pardo. *Painless Multi-level Automatic Goal-Oriented hp-Adaptive Coarsening Strategy.*
XVI Congreso de Matemática Aplicada, Gijón, Spain, [June 14-18, 2021].

8.3. Seminars

2022 **F. V. Caro**, V. Darrigrand, J. Alvarez-Aramberri, E. Alberdi, and D. Pardo. *A Boundary Value Problem: A Painless Multi-Level hp-Adaptive Case.*
Centro Universitario de Ciencias Exactas e Ingenierías, Universidad de Guadalajara, Guadalajara, México, [March 9, 2022].

2021 **F. V. Caro**, V. Darrigrand, E. Alberdi, and D. Pardo. *A Painless Multi-level Automatic Goal-Oriented hp-Adaptive Coarsening Strategy.*
Red interuniversitaria de Ciencias-RIdeC, Lima, Perú, [July 13, 2021].

8.4. Research Stays

2023 AGH University of Science and Technology, Krakow (Poland)
Supervisor: Maciej Paszynski
Date: 2 February 2023 - 31 March 2023 (58 days)

2021 CNRS-IRIT-ENSEEIHT, Toulouse (France)
Supervisor: Vincent Darrigrand
Date: 24 September 2021 - 25 November 2021 (61 days)

2020 CNRS-IRIT-ENSEEIHT, Toulouse (France)
Supervisor: Vincent Darrigrand
Date: 1 November 2020 - 4 December 2020 (34 days)

8.5. Implemented software

In this dissertation, I used the FEM library from the MathMode group[1]. The group initially designed this library to address elliptic problems using an energy-based-adaptive *hp*-strategy with H^1-conforming discretizations. The library, written in Fortran90, supports solving problems in 1D, 2D (using quadrilateral elements), and 3D (using hexahedral elements).

I contributed to the software in two significant ways. First, I expanded the energy-based-adaptive *hp*-strategy to a Goal-Oriented (GO) *hp*-adaptive algorithm that now handles both elliptic and non-elliptic problems. In this effort, I collaborated with Dr. Vincent Darrigrand and Dr. Julen Alvarez-Aramberri to introduce an upper bound of the error representation expressed through an inner product depending on the problem's bilinear form. Furthermore, we collaborated to enhance the adaptive *hp*-strategy to fit the Multi-Adaptive Goal-Oriented (MAGO) framework for solving parametric Partial Differential Equations (PDEs). Our method seeks to produce reliable synthetic data or measurements, which experts can utilize for solving Inverse Problems (IPs) or training Neural Networks (NNs). We implemented this using piecewise-constant materials that align with the discretization. Instead of computing integrals for each sample, which would be time-consuming, we precomputed and saved the integrals for a unitary sample only once, optimizing the stiffness matrix computation process.

[1] `https://www.mathmode.science/home`

9. Conclusions and Future Work

9.1. Conclusions

This dissertation mainly focuses on expanding an energy-based *hp*-adaptive algorithm previously limited to elliptic problems to both elliptic and non-elliptic problems under a Goal-Oriented (GO) framework.

Chapter 4 proposes *h*- and *p*-Goal-Oriented Adaptive (GOA) strategies suitable for both elliptic and potentially non-elliptic problems. These strategies use hierarchical basis functions to handle the *hanging nodes*, first performing a global and uniform refinement and then a coarsening step to remove certain basis functions. To determine which basis functions to remove, we employ an unconventional symmetric and positive definite bilinear form that quantifies the error in the Quantity of Interest (QoI). We test these algorithms on 1D Helmholtz and convection-diffusion problems by applying the Laplace operator's *pseudo-dual* problem. The numerical results show a linear convergence rate for the h scenarios and a quasi-exponential rate for the p scenarios.

Chapter 5 introduces an automatic adaptive mesh-generation strategy alternating between refinement and quasi-optimal *hp*-unrefinement procedures. Identifying which basis functions to remove efficiently presents a challenge. To address this, we extend a coarsening strategy previously tailored for energy-norm adaptivity to address non-elliptic problems and GOA strategies. Precisely, we consider the relevance of each basis function to the solution using an inner product associated with the problem's bilinear form. Based on these evaluations, each coarsening step eliminates certain basis functions. The algorithm's design simplifies implementation using hierarchical data structures that avoid the conventional 1-irregularity rule, which usually deals with hanging nodes. Our numerical results, which include 2D problems such as Poisson, Helmholtz, and convection-dominated equations, validate the algorithm's robustness and fast convergence. The resulting algorithm is easy to implement, and due to its robustness and rapid convergence, it shows potential for easy adaptation to industrial scenarios. Chapter 6 highlights the strengths of our algorithm, showcasing its performance on a 3D heterogeneous Helmholtz equation-based problem.

In Chapter 7, we introduce the Multi-Adaptive Goal-Oriented (MAGO) strategy to address the computational costs and dataset requirements associated with

accurately training a Deep Neural Network (DNN) to mimic the forward solver. Building upon our previously developed GOA approach for non-parametric Partial Differential Equations (PDEs), MAGO demonstrates promising results in efficiently generating a single *hp*-mesh. This optimized mesh ensures accurate computation of the QoI for multiple samples within a single GOA process. By combining the individual errors from all samples using l_1, l_2, and l_∞ norms, the MAGO approach provides sufficiently accurate solutions for all scenarios, including wave propagation examples with both *h*-refinements towards material discontinuities and strong *p*-refinements. The accuracy assessment of MAGO 's adaptivity through box plots indicates that a more significant number of samples involved in the adaptive process (S_A) leads to improved *hp*-grid results. Consequently, the statistical properties associated with the maximum relative error decrease as S_A increases. The results underscore the robustness, speed, and computational efficiency of MAGO as an alternative for generating reliable databases while ensuring high accuracy. Furthermore, the computational costs in terms of Floating Point Operations (FLOPs) of the Single-Adaptive Goal-Oriented (SAGO) and MAGO strategies, based on factorization, are detailed in Tables 7.1 and 7.2, respectively. Notably, the MAGO approach demonstrates its effectiveness in problem-solving within this context, as evidenced by $C^{\mathrm{MAGO}} < C^{\mathrm{SAGO}}$. This observation underscores that the MAGO approach attains a higher level of accuracy while simultaneously reducing costs, rendering it a particularly suitable choice for addressing challenging problems.

9.2. Future Work

In this dissertation, we identify potential paths for future research. One significant avenue is the extension of algorithms to address multi-physics problems, notably $H(\mathrm{curl})$ and $H(\mathrm{div})$. Enhanced parallelization and factorization techniques can reduce future computational resource requirements. Moreover, it is crucial to validate the efficacy of our algorithms in real-world scenarios such as Magnetotellurics, Controlled Sources, and Logging While Drilling.

Furthermore, our approach to generating expansive databases, explicitly designed for DNN training, can be improved. By integrating our strategy with Machine Learning (ML) methodologies, we can expedite and improve the DNN training processes. An in-depth analysis of the impact of the nature and distribution of various random samples on Deep Learning (DL) inversion could provide critical insights for optimization.

Bibliography

[1] B. A. Szabó. Mesh design for the p-version of the finite element method. *Computer Methods in Applied Mechanics and Engineering*, 55(1):181–197, 1986. (cited in page(s) 3)

[2] M. Ainsworth and J. T. Oden. A procedure for a posteriori error estimation for $h-p$ finite element methods. *Computer Methods in Applied Mechanics and Engineering*, 101(1):73–96, 1992. (cited in page(s) 3)

[3] M. Ainsworth and J. T. Oden. A unified approach to a posteriori error estimation using element residual methods. *Numerische Mathematik*, 65(1):23–50, 1993. (cited in page(s) 3)

[4] M. Ainsworth and J. T. Oden. A posteriori error estimation in finite element analysis. *Computer Methods in Applied Mechanics and Engineering*, 142(1):1–88, 1997. (cited in page(s) 3, 8)

[5] M. Ainsworth and B. Senior. An adaptive refinement strategy for *hp*-finite element computations. *Applied Numerical Mathematics*, 26(1):165–178, 1998. (cited in page(s) 3)

[6] J. Alvarez-Aramberri and D. Pardo. Dimensionally adaptive *hp*-finite element simulation and inversion of 2D magnetotelluric measurements. *Journal of Computational Science*, 18:95–105, 2017. (cited in page(s) 57)

[7] J. Alvarez-Aramberri, D. Pardo, and H. Barucq. Inversion of Magnetotelluric Measurements Using Multigoal Oriented *hp*-adaptivity. *Procedia Computer Science*, 18:1564–1573, 2013. 2013 International Conference on Computational Science. (cited in page(s) 3)

[8] J. Alvarez-Aramberri, D. Pardo, and H. Barucq. A secondary field based *hp*-Finite Element Method for the simulation of magnetotelluric measurements. *Journal of Computational Science*, 11:137–144, 2015. (cited in page(s) 3)

[9] H. Antil, R. Khatri, R. Löhner, and D. Verma. Fractional deep neural network via constrained optimization. *Machine Learning: Science and Technology*, 2(1):015003, dec 2020. (cited in page(s) 57)

[10] P. F. Antonietti, S. Giani, and P. Houston. *hp*-Version Composite Discontinuous Galerkin Methods for Elliptic Problems on Complicated Domains. *SIAM Journal on Scientific Computing*, 35(3):A1417–A1439, 2013. (cited in page(s) 4)

[11] M. Araya-Polo, T. Dahlke, C. Frogner, C. Zhang, T. Poggio, and D. Hohl. Automated fault detection without seismic processing. *The Leading Edge*, 36(3):208–214, 2017. (cited in page(s) 57)

[12] R. C. Aster, B. Borchers, and C. H. Thurber. *Parameter Estimation and Inverse Problems*. Elsevier, 2019. (cited in page(s) 57)

[13] I. Babuška. Courant element: Before and after. Technical Report BN-1154, University of Maryland, College Park, MD, 1993. (cited in page(s) 2)

[14] I. Babuška and M. R. Dorr. Error estimates for the combined h and p versions of the finite element method. *Numerische Mathematik*, 37:257–277, 1981. (cited in page(s) 2)

[15] I. Babuška and W. C. Rheinboldt. *A-posteriori* error estimates for the finite element method. *International Journal for Numerical Methods in Engineering*, 12(10):1597–1615, 1978. (cited in page(s) 2)

[16] I. Babuška and W. C. Rheinboldt. Error Estimates for Adaptive Finite Element Computations. *SIAM Journal on Numerical Analysis*, 15(4):736–754, 1978. (cited in page(s) 2)

[17] I. Babuška and W. C. Rheinboldt. Adaptive approaches and reliability estimations in finite element analysis. *Computer Methods in Applied Mechanics and Engineering*, 17-18:519–540, 1979. (cited in page(s) 2)

[18] I. Babuška and T. Strouboulis. *The finite element method and its reliability*. Oxford university press, 2001. (cited in page(s) 2)

[19] I. Babuška, B. A. Szabo, and I. N. Katz. The p-Version of the Finite Element Method. *SIAM Journal on Numerical Analysis*, 18(3):515–545, 1981. (cited in page(s) 2)

[20] S. A. Bakr, D. Pardo, and T. Mannseth. Domain decomposition Fourier finite element method for the simulation of 3D marine CSEM measurements. *Journal of Computational Physics*, 255:456–470, 2013. (cited in page(s) 57)

[21] W. Bangerth, C. Burstedde, T. Heister, and M. Kronbichler. Algorithms and data structures for massively parallel generic adaptive finite element codes. *ACM Trans. Math. Softw.*, 38(2), jan 2012. (cited in page(s) 52)

[22] W. Bangerth and R. Rannacher. *Adaptive Finite Element Methods for Differential Equations*. Birkhäuser, 2003. (cited in page(s) 3)

[23] R. E. Bank. PLTMG User's Guide, Edition 5.0. Technical report, Department of Mathematics, University of California at San Diego, 1988. (cited in page(s) 3)

[24] R. E. Bank, A. H. Sherman, and H. Weiser. Refinement algorithms and data structures for regular local mesh refinement. In R. Stepleman, editor, *Scientific Computing*, pages 3–17, Amsterdam, 1983. IMACS North-Holland. (cited in page(s) 3)

[25] K.-J. Bathe. *Finite Element Procedures*. Klaus-Jürgen Bathe, 2006. (cited in page(s) 1)

[26] R. Becker and R. Rannacher. *Weighted A Posteriori Error Control in FE Methods*. IWR, 1996. (cited in page(s) 5, 8)

[27] T. Belytschko, W. K. Liu, B. Moran, and K. Elkhodary. *Nonlinear finite elements for continua and structures*. John Wiley & Sons, 2014. (cited in page(s) 1)

[28] J. Berg and K. Nyström. A unified deep artificial neural network approach to partial differential equations in complex geometries. *Neurocomputing*, 317:28–41, 2018. (cited in page(s) 57)

[29] P. Binev. Instance optimality for *hp*-type approximation. *Oberwolfach Reports*, 39(1):14–16, 2013. (cited in page(s) 4, 13, 62)

[30] P. Binev. Tree approximation for hp-adaptivity. *SIAM Journal on Numerical Analysis*, 56(6):3346–3357, 2018. (cited in page(s) 5)

[31] N. Bize-Forest, L. Lima, V. Baines, A. Boyd, F. Abbots, and A. Barnett. Using machine-learning for depositional facies prediction in a complex carbonate reservoir. *Soc. Petrophys. Well-Log Analysts*, pages 1–11, 2018. (cited in page(s) 57)

[32] B. Bougher. Machine learning applications to geophysical data analysis. Master's thesis, The University of British Columbia, 2016. (cited in page(s) 57)

[33] S. C. Brenner, L. R. Scott, and L. R. Scott. *The Mathematical Theory of Finite Element Methods*. Springer New York, NY, 2008. (cited in page(s) 1)

[34] I. Brevis, I. Muga, and K. G. van der Zee. A machine-learning minimal-residual (ML-MRes) framework for goal-oriented finite element discretizations. *Computers & Mathematics with Applications*, 95:186–199, 2021. Recent Advances in Least-Squares and Discontinuous Petrov–Galerkin Finite Element Methods. (cited in page(s) 57)

[35] I. Brevis, I. Muga, and K. G. van der Zee. Neural control of discrete weak formulations: Galerkin, least squares & minimal-residual methods with quasi-optimal weights. *Computer Methods in Applied Mechanics and Engineering*, 402:115716, 2022. A Special Issue in Honor of the Lifetime Achievements of J. Tinsley Oden. (cited in page(s) 57)

[36] M. Bürg and W. Dörfler. Convergence of an adaptive *hp* finite element strategy in higher space-dimensions. *Applied Numerical Mathematics*, 61(11):1132–1146, 2011. (cited in page(s) 5)

[37] V. M. Calo, D. Pardo, and M. R. Paszyński. Goal-Oriented Self-Adaptive *hp* Finite Element Simulation of 3D DC Borehole Resistivity Simulations. *Procedia Computer Science*, 4:1485–1495, 2011. Proceedings of the International Conference on Computational Science, ICCS 2011. (cited in page(s) 3)

[38] A. Cangiani, Z. Dong, E. H. Georgoulis, and P. Houston. *hp*-Version discontinuous Galerkin methods for advection-diffusion-reaction problems on polytopic meshes. *ESAIM: Mathematical Modelling and Numerical Analysis*, 50(3):699–725, 2016. (cited in page(s) 4)

[39] A. Cangiani, E. H. Georgoulis, and P. Houston. hp-version discontinuous Galerkin methods on polygonal and polyhedral meshes. *Mathematical Models and Methods in Applied Sciences*, 24(10):2009–2041, 2014. (cited in page(s) 4)

[40] C. Canuto, R. H. Nochetto, R. Stevenson, and M. Verani. Convergence and optimality of **hp**-AFEM. *Numerische Mathematik*, 135:1073–1119, 2017. (cited in page(s) 4, 5, 13, 62)

[41] C. Canuto, R. H. Nochetto, R. Stevenson, and M. Verani. On *p*-robust saturation for *hp*-AFEM. *Computers & Mathematics with Applications*, 73(9):2004–2022, 2017. (cited in page(s) 5)

[42] P. Carnevali, R. B. Morris, Y. Tsuji, and G. Taylor. New basis functions and computational procedures for p-version finite element analysis. *International Journal for Numerical Methods in Engineering*, 36(22):3759–3779, 1993. (cited in page(s) 2)

[43] F. V. Caro, V. Darrigrand, J. Alvarez-Aramberri, E. Alberdi, and D. Pardo. A painless multi-level automatic goal-oriented *hp*-adaptive coarsening strategy for elliptic and non-elliptic problems. *Computer Methods in Applied Mechanics and Engineering*, 401:115641, 2022. (cited in page(s) 8, 58, 61, 73, 90)

[44] F. V. Caro, V. Darrigrand, J. Alvarez-Aramberri, E. A. Celaya, and D. Pardo. 1D Painless Multi-Level Automatic Goal-Oriented h and p Adaptive Strategies Using a Pseudo-Dual Operator. In D. Groen, C. de Mulatier, M. Paszyński, V. V. Krzhizhanovskaya, J. J. Dongarra, and P. M. A. Sloot, editors, *Computational Science – ICCS 2022*, pages 347–357, Cham, 2022. Springer International Publishing. (cited in page(s) 8, 22, 58, 73, 90)

[45] L. Chamoin and P. Ladevèze. Bounds on history-dependent or independent local quantities in viscoelasticity problems solved by approximate methods. *International Journal for Numerical Methods in Engineering*, 71(12):1387–1411, 2007. (cited in page(s) 6)

[46] P. G. Ciarlet. Basic error estimates for elliptic problems. In *Finite Element Methods (Part 1)*, volume 2 of *Handbook of Numerical Analysis*, pages 17–351. Elsevier, 1991. (cited in page(s) 5)

[47] P. G. Ciarlet. *The Finite Element Method for Elliptic Problems*. Society for Industrial and Applied Mathematics, 2002. (cited in page(s) 1, 5)

[48] R. W. Clough. On the importance of higher modes of vibration in the earthquake response of a tall building. *Bulletin of the Seismological Society of America*, 45(4):289–301, 1955. (cited in page(s) 1)

[49] R. W. Clough. The Finite Element Method in Plane Stress Analysis. In *Proceedings of the 2nd ASCE Conference on Electric Computation*, 1960. (cited in page(s) 1)

[50] R. W. Clough. Early history of the finite element method from the view point of a pioneer. *International Journal for Numerical Methods in Engineering*, 60(1):283–287, 2004. (cited in page(s) 3)

[51] R. W. Clough and E. L. Wilson. Stress analysis of a gravity dam by the finite element method. In *Proceedings of the Symposium on the Use of Computers in Civil Engineering*, 1962. (cited in page(s) 1)

[52] N. Collier, L. Dalcin, D. Pardo, and V. M. Calo. The Cost of Continuity: Performance of Iterative Solvers on Isogeometric Finite Elements. *SIAM*

Journal on Scientific Computing, 35(2):A767–A784, 2013. (cited in page(s) 66)

[53] N. Collier, D. Pardo, L. Dalcin, M. Paszynski, and V. Calo. The cost of continuity: A study of the performance of isogeometric finite elements using direct solvers. *Computer Methods in Applied Mechanics and Engineering*, 213-216:353–361, 2012. (cited in page(s) 66)

[54] S. Congreve and P. Houston. Two-grid hp-DGFEM for second order quasi-linear elliptic PDEs based on an incomplete Newton iteration. In *Recent Advances in Scientific Computing and Applications*, volume 586 of *Contemporary Mathematics*, pages 135–142, Providence, RI, 2013. American Mathematical Society. (cited in page(s) 4)

[55] J. A. Cottrell, T. J. Hughes, and Y. Bazilevs. *Isogeometric analysis: toward integration of CAD and FEA*. John Wiley & Sons, 2009. (cited in page(s) 40, 42)

[56] R. Courant. Variational methods for the solution of problems of equilibrium and vibration. *Bulletin of the American Mathematical Society*, 49(1):1–43, 1943. (cited in page(s) iv, vi, 1)

[57] W. Dahmen, A. Kunoth, and J. Vorloeper. Convergence of Adaptive Wavelet Methods for Goal-Oriented Error Estimation. In A. B. de Castro, D. Gómez, P. Quintela, and P. Salgado, editors, *Numerical Mathematics and Advanced Applications*, pages 39–61, Berlin, Heidelberg, 2006. Springer Berlin Heidelberg. (cited in page(s) 5)

[58] P. Daniel, A. Ern, I. Smears, and M. Vohralík. An adaptive *hp*-refinement strategy with computable guaranteed bound on the error reduction factor. *Computers & Mathematics with Applications*, 76(5):967–983, 2018. (cited in page(s) 5)

[59] V. Darrigrand, D. Pardo, T. Chaumont-Frelet, I. Gómez-Revuelto, and L. E. Garcia-Castillo. A painless automatic *hp*-adaptive strategy for elliptic problems. *Finite Elements in Analysis and Design*, 178:103424, 2020. (cited in page(s) 4, 5, 7, 11, 12, 13, 16, 17, 22, 30, 61)

[60] V. Darrigrand, D. Pardo, and I. Muga. Goal-oriented adaptivity using unconventional error representations for the 1D Helmholtz equation. *Computers & Mathematics with Applications*, 69(9):964–979, 2015. (cited in page(s) 6, 7, 21)

[61] V. Darrigrand, A. Rodríguez-Rozas, I. Muga, D. Pardo, A. Romkes, and S. Prudhomme. Goal-oriented adaptivity using unconventional error representations for the multidimensional Helmholtz equation. *International Journal for Numerical Methods in Engineering*, 113(1):22–42, 2018. (cited in page(s) 6, 7)

[62] L. Demkowicz. *Computing with hp-ADAPTIVE FINITE ELEMENTS. Vol. 1. One and Two Dimensional Elliptic and Maxwell Problems.* Chapman and Hall/CRC., 2006. (cited in page(s) 3, 4, 5, 15, 20, 21)

[63] L. Demkowicz, J. Gopalakrishnan, and A. H. Niemi. A class of discontinuous Petrov–Galerkin methods. Part III: Adaptivity. *Applied Numerical Mathematics*, 62(4):396–427, 2012. Third Chilean Workshop on Numerical Analysis of Partial Differential Equations (WONAPDE 2010). (cited in page(s) 4)

[64] L. Demkowicz, J. Kurtz, D. Pardo, M. Paszyński, W. Rachowicz, and A. Zdunek. *Computing with hp-ADAPTIVE FINITE ELEMENTS: Volume II Frontiers: Three Dimensional Elliptic and Maxwell Problems with Applications (1st ed.).* Chapman and Hall/CRC., 2008. (cited in page(s) 3, 11, 15, 20, 21)

[65] L. Demkowicz, J. Oden, W. Rachowicz, and O. Hardy. Toward a universal h-p adaptive finite element strategy, part 1. Constrained approximation and data structure. *Computer Methods in Applied Mechanics and Engineering*, 77(1):79–112, 1989. (cited in page(s) 20)

[66] L. Demkowicz, W. Rachowicz, and P. Devloo. A Fully Automatic *hp*-Adaptivity. *Journal of Scientific Computing*, 17:117–142, 2002. (cited in page(s) 3, 4, 8, 11, 21)

[67] P. Deuflhard, P. Leinen, and H. Yserentant. Concepts of an adaptive hierarchical finite element code. *IMPACT of Computing in Science and Engineering*, 1(1):3–35, 1989. (cited in page(s) 3)

[68] P. Di Stolfo, A. Schröder, N. Zander, and S. Kollmannsberger. An easy treatment of hanging nodes in *hp*-finite elements. *Finite Elements in Analysis and Design*, 121:101–117, 2016. (cited in page(s) 4)

[69] J. Donea and A. Huerta. *Finite Element Methods for Flow Problems.* John Wiley & Sons, 2003. (cited in page(s) 1)

[70] W. Dörfler. A convergent adaptive algorithm for poisson's equation. *SIAM Journal on Numerical Analysis*, 33(3):1106–1124, 1996. (cited in page(s) 5)

[71] M. R. Dorr. The approximation theory for the p-version of the finite element method. *SIAM Journal on Numerical Analysis*, 21(6):1180–1207, 1984. (cited in page(s) 2)

[72] T. Dunne. An Eulerian approach to fluid–structure interaction and goal-oriented mesh adaptation. *International Journal for Numerical Methods in Fluids*, 51(9-10):1017–1039, 2006. (cited in page(s) 6)

[73] A. Düster, E. Rank, and B. A. Szabó. The *p*-Version of the Finite Element and Finite Cell Methods. *Encyclopedia of Computational Mechanics Second Edition*, pages 1–35, 2017. (cited in page(s) 3)

[74] W. E, J. Han, and A. Jentzen. Deep Learning-Based Numerical Methods for High-Dimensional Parabolic Partial Differential Equations and Backward Stochastic Differential Equations. *Communications in Mathematics and Statistics*, 5(4):349–380, 2017. (cited in page(s) 57)

[75] B. Erdmann, R. Roitzsch, and F. A. Bornemann. *KASKADE: numerical experiments*. Number TR 91-1 in Technical Report. Konrad-Zuse-Zentrum für Informationstechnik Berlin, 1991. (cited in page(s) 3)

[76] M. Feischl, D. Praetorius, and K. G. van der Zee. An Abstract Analysis of Optimal Goal-Oriented Adaptivity. *SIAM Journal on Numerical Analysis*, 54(3):1423–1448, 2016. (cited in page(s) 6)

[77] S. Franz and T. Linß. Superconvergence analysis of the Galerkin FEM for a singularly perturbed convection–diffusion problem with characteristic layers. *Numerical Methods for Partial Differential Equations*, 24(1):144–164, 2008. (cited in page(s) 39)

[78] S. Franz and G. Matthies. Local projection stabilisation on S-type meshes for convection–diffusion problems with characteristic layers. *Computing*, 87(3):135–167, 2010. (cited in page(s) 39)

[79] S. Franz and H.-G. Roos. Error estimation in a balanced norm for a convection-diffusion problem with two different boundary layers. *Calcolo*, 51(3):423–440, 2014. (cited in page(s) 39)

[80] L. E. Garcia-Castillo, D. Pardo, and L. F. Demkowicz. Energy-norm-based and goal-oriented automatic *hp* adaptivity for electromagnetics: Application to waveguide discontinuities. *IEEE Transactions on Microwave Theory and Techniques*, 56(12):3039–3049, 2008. (cited in page(s) 3)

[81] L. E. García-Castillo, D. Pardo, I. Gómez-Revuelto, and L. F. Demkowicz. A two-dimensional self-adaptive *hp* finite element method for the characterization of waveguide discontinuities. Part I: Energy-norm based automatic *hp*-adaptivity. *Computer Methods in Applied Mechanics and Engineering*, 196(49):4823–4852, 2007. (cited in page(s) 3)

[82] S. Giani and E. Hall. An a-posteriori error estimate for *hp*-adaptive DG methods for elliptic eigenvalue problems on anisotropically refined meshes. *Computing*, 95(1):319–341, 05 2013. (cited in page(s) 4)

[83] S. Giani, D. Schötzau, and L. Zhu. An a-posteriori error estimate for *hp*-adaptive DG methods for convection–diffusion problems on anisotropically refined meshes. *Computers & Mathematics with Applications*, 67(4):869–887, 2014. High-order Finite Element Approximation for Partial Differential Equations. (cited in page(s) 4)

[84] I. Gomez-Revuelto, L. E. García-Castillo, S. Llorente-Romano, and D. Pardo. A three-dimensional self-adaptive *hp* finite element method for the characterization of waveguide discontinuities. *Computer Methods in Applied Mechanics and Engineering*, 249-252:62–74, 2012. Higher Order Finite Element and Isogeometric Methods. (cited in page(s) 3)

[85] I. Goodfellow, Y. Bengio, and A. Courville. *Deep Learning*. MIT Press, 2016. (cited in page(s) 57)

[86] T. Grätsch and K.-J. Bathe. Goal-oriented error estimation in the analysis of fluid flows with structural interactions. *Computer Methods in Applied Mechanics and Engineering*, 195(41):5673–5684, 2006. John H. Argyris Memorial Issue. Part II. (cited in page(s) 6)

[87] B. Guo and I. Babuška. The $h-p$ version of the finite element method. Part 1: The basic approximation results. *Computational Mechanics*, 1(1):21–41, 1986. (cited in page(s) 2)

[88] B. Guo and I. Babuška. The $h-p$ version of the finite element method. Part 2: General results and applications. *Computational Mechanics*, 1(3):203–220, 1986. (cited in page(s) 2)

[89] J. Han, A. Jentzen, and W. E. Solving high-dimensional partial differential equations using deep learning. *Proceedings of the National Academy of Sciences*, 115(34):8505–8510, 2018. (cited in page(s) 57)

[90] A. Hashemian, D. Garcia, J. A. Rivera, and D. Pardo. Massive database generation for 2.5D borehole electromagnetic measurements using refined

isogeometric analysis. *Computers & Geosciences*, 155:104808, 2021. (cited in page(s) 8)

[91] M. Holst and S. Pollock. Convergence of Goal-Oriented Adaptive Finite Element Methods for Nonsymmetric Problems. *Numerical Methods for Partial Differential Equations*, 32(2):479–509, 2016. (cited in page(s) 6)

[92] M. Holst, S. Pollock, and Y. Zhu. Convergence of goal-oriented adaptive finite element methods for semilinear problems. *Computing and Visualization in Science*, 17(1):43–63, 2015. ID: Holst2015. (cited in page(s) 6)

[93] P. Houston, C. Schwab, and E. Süli. Discontinuous *hp*-Finite Element Methods for Advection-Diffusion-Reaction Problems. *SIAM Journal on Numerical Analysis*, 39(6):2133–2163, 2002. (cited in page(s) 4)

[94] T. Hughes. *The Finite Element Method: Linear Static and Dynamic Finite Element Analysis*. Dover Publications, Inc., 2000. (cited in page(s) 1)

[95] U. Iturrarán-Viveros, A. M. Muñoz-García, O. Castillo-Reyes, and K. Shukla. Machine Learning as a Seismic Prior Velocity Model Building Method for Full-Waveform Inversion: A Case Study from Colombia. *Pure and Applied Geophysics*, 178(2):423–448, 2021. (cited in page(s) 57)

[96] C. Jhurani and L. Demkowicz. Multiscale modeling using goal-oriented adaptivity and numerical homogenization. Part I: Mathematical formulation and numerical results. *Computer Methods in Applied Mechanics and Engineering*, 213-216:399–417, 2012. (cited in page(s) 6)

[97] C. Jhurani and L. Demkowicz. Multiscale modeling using goal-oriented adaptivity and numerical homogenization. Part II: Algorithms for the Moore–Penrose pseudoinverse. *Computer Methods in Applied Mechanics and Engineering*, 213-216:418–426, 2012. (cited in page(s) 6)

[98] C. Johnson. *Numerical Solution of Partial Differential Equations by the Finite Element Method*. Dover Publications, 2012. (cited in page(s) 1)

[99] J. N. Jomo, N. Zander, M. Elhaddad, A. Özcan, S. Kollmannsberger, R.-P. Mundani, and E. Rank. Parallelization of the multi-level *hp*-adaptive finite cell method. *Computers & Mathematics with Applications*, 74(1):126–142, 2017. 5th European Seminar on Computing ESCO 2016. (cited in page(s) 52)

[100] M. Jungiewicz and A. Smywiński-Pohl. Towards textual data augmentation for neural networks: synonyms and maximum loss. *Computer Science*, 20(1):57–83, 2019. (cited in page(s) 57)

[101] G. E. Karniadakis and S. J. Sherwin. *Spectral/hp Element Methods for Computational Fluid Dynamics*. Numerical Mathematics and Scientific Computation. Oxford University Press, 2nd edition, 2013. (cited in page(s) 3)

[102] E. Kharazmi and G. E. Karniadakis. Variational Physics-Informed Neural Networks for Solving Partial Differential Equations. *arXiv preprint arXiv:1912.00873*, 2019. (cited in page(s) 57)

[103] Y. Khoo, J. Lu, and L. Ying. Solving parametric PDE problems with artificial neural networks. *European Journal of Applied Mathematics*, 32(3):421–435, 2021. (cited in page(s) 57)

[104] P. Kopp, V. Calo, E. Rank, and S. Kollmannsberger. Space-time *hp*-finite elements for heat evolution in laser powder bed fusion additive manufacturing. *Engineering with Computers*, 38:4879–4893, 2022. (cited in page(s) 4)

[105] P. Kopp, E. Rank, V. M. Calo, and S. Kollmannsberger. Efficient multi-level *hp*-finite elements in arbitrary dimensions. *Computer Methods in Applied Mechanics and Engineering*, 401:115575, 2022. (cited in page(s) 4)

[106] D. La Torre, H. Kunze, F. Mendivil, M. Ruiz Galan, and R. Zaki. Inverse Problems: Theory and Application to Science and Engineering 2015. *Mathematical Problems in Engineering*, 2015:796094, 2015. (cited in page(s) 57)

[107] P. Ladevèze. Upper error bounds on calculated outputs of interest for linear and nonlinear structural problems. *Comptes Rendus Mécanique*, 334(7):399–407, 2006. (cited in page(s) 6)

[108] P. Ladevèze. Strict upper error bounds on computed outputs of interest in computational structural mechanics. *Computational Mechanics*, 42(2):271–286, 2008. TY - JOUR. (cited in page(s) 6)

[109] S. Larsson and V. Thomée. *Partial Differential Equations with Numerical Methods*, volume 45. Springer Berlin, Heidelberg, 2003. (cited in page(s) 1)

[110] D. J. Lary, A. H. Alavi, A. H. Gandomi, and A. L. Walker. Machine learning in geosciences and remote sensing. *Geoscience Frontiers*, 7(1):3–10, 2016. Special Issue: Progress of Machine Learning in Geosciences. (cited in page(s) 57)

[111] Y. LeCun, Y. Bengio, and G. Hinton. Deep learning. *Nature*, 521(7553):436–444, 2015. (cited in page(s) 57)

[112] W. K. Liu, S. Li, and H. S. Park. Eighty Years of the Finite Element Method: Birth, Evolution, and Future. *Archives of Computational Methods in Engineering*, 29(6):4431–4453, 2022. (cited in page(s) 57)

[113] L. Lu, X. Meng, Z. Mao, and G. E. Karniadakis. DeepXDE: A Deep Learning Library for Solving Differential Equations. *SIAM Review*, 63(1):208–228, 2021. (cited in page(s) 57)

[114] Y. Maday, A. T. Patera, and J. Peraire. A general formulation for a posteriori bounds for output functionals of partial differential equations; application to the eigenvalue problem. *C. R. Acad. Sci. Paris Sér. I Math.*, 328(9):823–828, 1999. (cited in page(s) 5)

[115] C. Mesztenyi, A. Miller, and W. Szymczak. FEARS: Details of Mathematical Formulation Univac 1100. Technical Report BN-994, University of Maryland, College Park, 1982. (cited in page(s) 3)

[116] C. Mesztenyi and W. C. Rheinboldt. NFEARS: A Nonlinear Adaptive Finite Element Solver. Technical Report ICMA-87-113, Department of Mathematics and Statistics, University of Pittsburgh, 1987. (cited in page(s) 3)

[117] T. Mitchell. *Machine Learning*. McGraw-Hill International Edit, McGraw Hill Higher Education, 1st edition, 1997. (cited in page(s) 57)

[118] W. F. Mitchell and M. A. McClain. A Comparison of *hp*-adaptive Strategies for Elliptic Partial Differential Equations. *ACM Trans. Math. Softw.*, 41(1), oct 2014. (cited in page(s) 4)

[119] M. S. Mommer and R. Stevenson. A Goal-Oriented Adaptive Finite Element Method with Convergence Rates. *SIAM Journal on Numerical Analysis*, 47(2):861–886, 2009. (cited in page(s) 5)

[120] K.-S. Moon, E. von Schwerin, A. Szepessy, and R. Tempone. Convergence Rates for an Adaptive Dual Weighted Residual Finite Element Algorithm. *BIT Numerical Mathematics*, 46(2):367–407, 2006. (cited in page(s) 5)

[121] P. Morin, R. H. Nochetto, and K. G. Siebert. Convergence of adaptive finite element methods. *SIAM Review*, 44(4):631–658, 2002. (cited in page(s) 5)

[122] C. D. Mote Jr. Global-local finite element. *International Journal for Numerical Methods in Engineering*, 3(4):565–574, 1971. (cited in page(s) 11)

[123] J. Muñoz-Matute, E. Alberdi, D. Pardo, and V. M. Calo. Time-domain goal-oriented adaptivity using pseudo-dual error representations. *Computer*

Methods in Applied Mechanics and Engineering, 325:395–415, 2017. (cited in page(s) 7)

[124] A. K. Noor. Global-local methodologies and their application to nonlinear analysis. *Finite Elements in Analysis and Design*, 2(4):333–346, 1986. (cited in page(s) 11)

[125] J. T. Oden. *Historical Comments on Finite Elements*, page 152–166. Association for Computing Machinery, New York, NY, USA, 1990. (cited in page(s) 1)

[126] J. T. Oden. Finite elements: An introduction. In P. G. Ciarlet and J. L. Lions, editors, *Handbook of Numerical Analysis*, volume 2, pages 3–15. North–Holland, Amsterdam, 1991. (cited in page(s) 2)

[127] J. T. Oden and L. Demkowicz. *Applied Functional Analysis*. CRC press, 2017. (cited in page(s) 1)

[128] J. T. Oden and A. Patra. A parallel adaptive strategy for hp finite element computations. *Computer Methods in Applied Mechanics and Engineering*, 121(1):449–470, 1995. (cited in page(s) 3)

[129] J. T. Oden and S. Prudhomme. New approaches to error estimation and adaptivity for the stokes and oseen equations. *International Journal for Numerical Methods in Fluids*, 31(1):3–15, 1999. (cited in page(s) 5)

[130] J. T. Oden and S. Prudhomme. Goal-oriented error estimation and adaptivity for the finite element method. *Computers & Mathematics with Applications*, 41(5):735–756, 2001. (cited in page(s) 5, 18, 20)

[131] J. T. Oden, S. Prudhomme, and P. Bauman. On the extension of goal-oriented error estimation and hierarchical modeling to discrete lattice models. *Computer Methods in Applied Mechanics and Engineering*, 194(34):3668–3688, 2005. (cited in page(s) 6)

[132] J. T. Oden and K. S. Vemaganti. Estimation of Local Modeling Error and Goal-Oriented Adaptive Modeling of Heterogeneous Materials: I. Error Estimates and Adaptive Algorithms. *Journal of Computational Physics*, 164(1):22–47, 2000. (cited in page(s) 6)

[133] P. Oswald. On function spaces related to finite element approximation theory. *Z. Anal. Anwend.*, 9(1):43–64, 1990. (cited in page(s) 2)

[134] J. S. Ovall. Asymptotically exact functional error estimators based on superconvergent gradient recovery. *Numerische Mathematik*, 102(3):543–558, 2006. (cited in page(s) 5)

[135] J. Panetier, P. Ladevèze, and L. Chamoin. Strict and effective bounds in goal-oriented error estimation applied to fracture mechanics problems solved with XFEM. *International Journal for Numerical Methods in Engineering*, 81(6):671–700, 2010. (cited in page(s) 6)

[136] G. Pang, L. Lu, and G. E. Karniadakis. fPINNs: Fractional Physics-Informed Neural Networks. *SIAM Journal on Scientific Computing*, 41(4):A2603–A2626, 2019. (cited in page(s) 57)

[137] M. Paraschivoiu and A. T. Patera. A hierarchical duality approach to bounds for the outputs of partial differential equations. *Computer Methods in Applied Mechanics and Engineering*, 158(3):389–407, 1998. (cited in page(s) 5)

[138] M. Paraschivoiu, J. Peraire, and A. T. Patera. A posteriori finite element bounds for linear-functional outputs of elliptic partial differential equations. *Computer Methods in Applied Mechanics and Engineering*, 150(1):289–312, 1997. Symposium on Advances in Computational Mechanics. (cited in page(s) 5)

[139] D. Pardo. *Integration of HP-Adaptivity with a Two Grid Solver: Applications to Electromagnetics*. PhD thesis, The University of Texas at Austin, 2004. (cited in page(s) 3)

[140] D. Pardo. Multigoal-oriented adaptivity for *hp*-finite element methods. *Procedia Computer Science*, 1(1):1953–1961, 2010. ICCS 2010. (cited in page(s) 3)

[141] D. Pardo, L. Demkowicz, C. Torres-Verdín, and C. Michler. PML Enhanced with a Self-Adaptive Goal-Oriented *hp*-Finite Element Method: Simulation of Through-Casing Borehole Resistivity Measurements. *SIAM Journal on Scientific Computing*, 30(6):2948–2964, 2008. (cited in page(s) 3)

[142] D. Pardo, L. Demkowicz, C. Torres-Verdín, and M. Paszynski. Two-Dimensional High-Accuracy Simulation of Resistivity Logging-While-Drilling (LWD) Measurements Using a Self-Adaptive Goal-Oriented *hp* Finite Element Method. *SIAM Journal on Applied Mathematics*, 66(6):2085–2106, 2006. (cited in page(s) 6)

[143] D. Pardo, L. Demkowicz, C. Torres-Verdín, and M. Paszynski. A self-adaptive goal-oriented *hp*-finite element method with electromagnetic applications. Part II: Electrodynamics. *Computer Methods in Applied Mechanics and Engineering*, 196(37):3585–3597, 2007. Special Issue Honoring the 80th Birthday of Professor Ivo Babuška. (cited in page(s) 6)

[144] D. Pardo, L. Demkowicz, C. Torres-Verdín, and L. Tabarovsky. A goal-oriented hp-adaptive finite element method with electromagnetic applications. Part I: electrostatics. *International Journal for Numerical Methods in Engineering*, 65(8):1269–1309, 2006. (cited in page(s) 6)

[145] D. Pardo, L. E. García-Castillo, L. F. Demkowicz, and C. Torres-Verdín. A two-dimensional self-adaptive *hp* finite element method for the characterization of waveguide discontinuities. Part II: Goal-oriented *hp*-adaptivity. *Computer Methods in Applied Mechanics and Engineering*, 196(49):4811–4822, 2007. (cited in page(s) 3)

[146] D. Pardo, M. Paszynski, N. Collier, J. Alvarez, L. Dalcin, and V. M. Calo. A survey on direct solvers for Galerkin methods. *SeMA Journal*, 57(1):107–134, 2012. (cited in page(s) 66)

[147] M. Paszyński, L. Demkowicz, and D. Pardo. Verification of goal-oriented HP-adaptivity. *Computers & Mathematics with Applications*, 50(8):1395–1404, 2005. (cited in page(s) 3)

[148] M. Paszyński, L. Demkowicz, and D. Pardo. Verification of goal-oriented hp-adaptivity. *Computers & Mathematics with Applications*, 50(8):1395–1404, 2005. (cited in page(s) 6)

[149] M. Paszyński, D. Pardo, and V. Calo. Parallel simulations of 3d DC borehole resistivity measurements with goal-oriented self-adaptive hp finite element method. *Journal of the Serbian Society for Computational Mechanics/Vol*, 6(2):1–18, 2012. (cited in page(s) 3)

[150] M. Paszyński and L. Demkowicz. Parallel, fully automatic *hp*-adaptive 3D finite element package. *Engineering with Computers*, 22(3):255–276, 12 2006. (cited in page(s) 52)

[151] M. Paszyński, R. Grzeszczuk, D. Pardo, and L. Demkowicz. Deep Learning Driven Self-adaptive Hp Finite Element Method. In *International Conference on Computational Science*, pages 114–121. Springer, 2021. (cited in page(s) 57)

[152] J. Peraire and A. T. Patera. Bounds for linear-functional outputs of coercive partial differential equations: local indicators and adaptive refinement. In M. Papadrakakis, A. Samartin, L. Eca, and Y. Tsompanakis, editors, *Advances in Adaptive Computational Methods in Mechanics*, volume 47 of *Studies in Applied Mechanics*, pages 199–216. Elsevier Science BV, Amsterdam, 1998. (cited in page(s) 5)

[153] J. Peraire and A. T. Patera. Asymptotic a posteriori finite element bounds for the outputs of noncoercive problems: the helmholtz and burgers equations. *Computer Methods in Applied Mechanics and Engineering*, 171(1):77–86, 1999. (cited in page(s) 5)

[154] S. Petrides and L. F. Demkowicz. An adaptive DPG method for high frequency time-harmonic wave propagation problems. *Computers & Mathematics with Applications*, 74(8):1999–2017, 2017. (cited in page(s) 4)

[155] S. Pollock. *Convergence of Goal-Oriented Adaptive Finite Element Methods*. PhD thesis, University of California, San Diego, 2012. (cited in page(s) 6)

[156] S. Prudhomme and J. T. Oden. On goal-oriented error estimation for elliptic problems: application to the control of pointwise errors. *Computer Methods in Applied Mechanics and Engineering*, 176(1):313–331, 1999. (cited in page(s) 5, 18, 20)

[157] S. Prudhomme and J. T. Oden. Computable error estimators and adaptive techniques for fluid flow problems. In *Error Estimation and Adaptive Discretization Methods in Computational Fluid Dynamics*, volume 25 of *Lecture Notes in Computational Science and Engineering*, page 207. Springer, Berlin, 2003. (cited in page(s) 5)

[158] V. Puzyrev. Deep learning electromagnetic inversion with convolutional neural networks. *Geophysical Journal International*, 218(2):817–832, 05 2019. (cited in page(s) 57)

[159] V. Puzyrev and A. Swidinsky. Inversion of 1D frequency- and time-domain electromagnetic data with convolutional neural networks. *Computers & Geosciences*, 149:104681, 2021. (cited in page(s) 57)

[160] W. Rachowicz and L. Demkowicz. An *hp*-adaptive finite element method for electromagnetics: Part 1: Data structure and constrained approximation. *Computer Methods in Applied Mechanics and Engineering*, 187(1):307–335, 2000. (cited in page(s) 11)

[161] W. Rachowicz, D. Pardo, and L. Demkowicz. Fully automatic *hp*-adaptivity in three dimensions. *Computer Methods in Applied Mechanics and Engineering*, 195(37):4816–4842, 2006. John H. Argyris Memorial Issue. Part I. (cited in page(s) 5)

[162] R. Rannacher and F.-T. Suttmeier. A feed-back approach to error control in finite element methods: application to linear elasticity. *Computational Mechanics*, 19(5):434–446, 1997. (cited in page(s) 5)

[163] R. Rannacher and F.-T. Suttmeier. A posteriori error control in finite element methods via duality techniques: Application to perfect plasticity. *Computational Mechanics*, 21(2):123–133, 1998. (cited in page(s) 5, 8)

[164] B. D. Reddy. *Introductory Functional Analysis: With Applications to Boundary Value Problems and Finite Elements*. Springer New York, NY, 2013. (cited in page(s) 1)

[165] J. N. Reddy. *Introduction to the Finite Element Method*. McGraw-Hill Education, 2019. (cited in page(s) 1)

[166] J. A. Rivera, J. M. Taylor, Ángel J. Omella, and D. Pardo. On quadrature rules for solving Partial Differential Equations using Neural Networks. *Computer Methods in Applied Mechanics and Engineering*, 393:114710, 2022. (cited in page(s) 57)

[167] R. Roitzsch. *KASKADE Programmer's Manual*. Konrad-Zuse-Zentrum, Berlin, 1989. (cited in page(s) 3)

[168] A. Romkes and J. T. Oden. Adaptive modeling of wave propagation in heterogeneous elastic solids. *Computer Methods in Applied Mechanics and Engineering*, 193(6):539–559, 2004. (cited in page(s) 21)

[169] A. Romkes, J. T. Oden, and K. Vemaganti. Multi-scale goal-oriented adaptive modeling of random heterogeneous materials. *Mechanics of Materials*, 38(8):859–872, 2006. Advances in Disordered Materials. (cited in page(s) 6)

[170] L. Ruthotto and E. Haber. Deep Neural Networks Motivated by Partial Differential Equations. *Journal of Mathematical Imaging and Vision*, 62(3):352–364, 2020. (cited in page(s) 57)

[171] E. Samaniego, C. Anitescu, S. Goswami, V. Nguyen-Thanh, H. Guo, K. Hamdia, X. Zhuang, and T. Rabczuk. An energy approach to the solution of partial differential equations in computational mechanics via

machine learning: Concepts, implementation and applications. *Computer Methods in Applied Mechanics and Engineering*, 362:112790, 2020. (cited in page(s) 57)

[172] J. Sarrate, J. Peraire, and A. T. Patera. A posteriori finite element error bounds for non-linear outputs of the helmholtz equation. *International Journal for Numerical Methods in Fluids*, 31(1):17–36, 1999. (cited in page(s) 5)

[173] J. Schöberl. NETGEN: An advancing front 2D/3D-mesh generator based on abstract rules. *Computing and Visualization in Science*, 1(1):41–52, 1997. (cited in page(s) 3)

[174] M. Shahriari, D. Pardo, A. Picon, A. Galdran, J. Del Ser, and C. Torres-Verdín. A deep learning approach to the inversion of borehole resistivity measurements. *Computational Geosciences*, 24(3):971–994, 2020. (cited in page(s) 57)

[175] M. Shahriari, D. Pardo, J. A. Rivera, C. Torres-Verdín, A. Picon, J. Del Ser, S. Ossandón, and V. M. Calo. Error control and loss functions for the deep learning inversion of borehole resistivity measurements. *International Journal for Numerical Methods in Engineering*, 122(6):1629–1657, 2021. (cited in page(s) 57)

[176] M. Shahriari, S. Rojas, D. Pardo, A. Rodríguez-Rozas, S. A. Bakr, V. M. Calo, and I. Muga. A Numerical 1.5D Method for the Rapid Simulation of Geophysical Resistivity Measurements. *Geosciences*, 8(6), 2018. (cited in page(s) 57)

[177] C. Shorten and T. M. Khoshgoftaar. A survey on Image Data Augmentation for Deep Learning. *Journal of Big Data*, 6(1):1–48, 2019. (cited in page(s) 57)

[178] P. Šolín and L. Demkowicz. Goal-oriented *hp*-adaptivity for elliptic problems. *Computer Methods in Applied Mechanics and Engineering*, 193(6):449–468, 2004. (cited in page(s) 6)

[179] P. Šolin, K. Segeth, and I. Dolezel. *Higher-Order Finite Element Methods*. Chapman and Hall/CRC., 2003. (cited in page(s) 4, 11)

[180] M. Stynes and L. Tobiska. The SDFEM for a Convection-Diffusion Problem with a Boundary Layer: Optimal Error Analysis and Enhancement of Accuracy. *SIAM Journal on Numerical Analysis*, 41(5):1620–1642, 2003. (cited in page(s) 39)

[181] B. A. Szabó. Implementation of a finite element software system with H and P extension capabilities. *Finite Elements in Analysis and Design*, 2(1):177–194, 1986. Special Issue on Unification of Finite Element Software Systems Proceedings of the 8th UFEM Symposium. (cited in page(s) 3)

[182] B. A. Szabó. The *p*- and *h*-*p* versions of the finite element method in solid mechanics. *Computer Methods in Applied Mechanics and Engineering*, 80(1):185–195, 1990. (cited in page(s) 3)

[183] B. A. Szabó and I. Babuška. *Finite Element Analysis: Method, Verification and Validation*. John Wiley & Sons, 2021. (cited in page(s) 2)

[184] A. Szymczak, A. Paszyńska, M. Paszyński, and D. Pardo. Preventing deadlock during anisotropic 2D mesh adaptation in *hp*-adaptive FEM. *Journal of Computational Science*, 4(3):170–179, 2013. Agent-Based Simulations, Adaptive Algorithms, ICCS 2011 Workshop. (cited in page(s) 4)

[185] T. Służalec, R. Grzeszczuk, S. Rojas, W. Dzwinel, and M. Paszyński. Quasi-optimal *hp*-finite element refinements towards singularities via deep neural network prediction. *Computers & Mathematics with Applications*, 142:157–174, 2023. (cited in page(s) 57)

[186] J. W. Tukey et al. *Exploratory data analysis*, volume 2. Reading, MA, 1977. (cited in page(s) 79)

[187] M. J. Turner, R. W. Clough, H. C. Martin, and L. Topp. Stiffness and deflection analysis of complex structures. *Journal of the Aeronautical Sciences*, 23(9):805–823, 1956. (cited in page(s) 1)

[188] C. Uriarte, D. Pardo, and Ángel Javier Omella. A Finite Element based Deep Learning solver for parametric PDEs. *Computer Methods in Applied Mechanics and Engineering*, 391:114562, 2022. (cited in page(s) 57)

[189] E. Valseth and A. Romkes. Goal-oriented error estimation for the automatic variationally stable FE method for convection-dominated diffusion problems. *Computers & Mathematics with Applications*, 80(12):3027–3043, 2020. (cited in page(s) 6)

[190] K. G. van der Zee. *Goal-adaptive discretization of fluid–structure interaction*. PhD thesis, Delft University of Technology, 2009. (cited in page(s) 6)

[191] K. G. van der Zee, J. Tinsley Oden, S. Prudhomme, and A. Hawkins-Daarud. Goal-oriented error estimation for Cahn–Hilliard models of binary

phase transition. *Numerical Methods for Partial Differential Equations*, 27(1):160–196, 2011. (cited in page(s) 7)

[192] K. G. van der Zee, E. H. van Brummelen, I. Akkerman, and R. de Borst. Goal-oriented error estimation and adaptivity for fluid–structure interaction using exact linearized adjoints. *Computer Methods in Applied Mechanics and Engineering*, 200(37):2738–2757, 2011. Special Issue on Modeling Error Estimation and Adaptive Modeling. (cited in page(s) 7)

[193] K. G. van der Zee, E. H. van Brummelen, and R. de Borst. Goal-oriented error estimation for stokes flow interacting with a flexible channel. *International Journal for Numerical Methods in Fluids*, 56(8):1551–1557, 2008. (cited in page(s) 7)

[194] K. G. van der Zee, E. H. van Brummelen, and R. de Borst. Goal-Oriented Error Estimation and Adaptivity for Free-Boundary Problems: The Domain-Map Linearization Approach. *SIAM Journal on Scientific Computing*, 32(2):1064–1092, 2010. (cited in page(s) 7)

[195] K. G. van der Zee, E. H. van Brummelen, and R. de Borst. Goal-Oriented Error Estimation and Adaptivity for Free-boundary Problems: The Shape-Linearization Approach. *SIAM Journal on Scientific Computing*, 32(2):1093–1118, 2010. (cited in page(s) 7)

[196] K. G. van der Zee and C. V. Verhoosel. Isogeometric analysis-based goal-oriented error estimation for free-boundary problems. *Finite Elements in Analysis and Design*, 47(6):600–609, 2011. The Twenty-Second Annual Robert J. Melosh Competition. (cited in page(s) 7)

[197] K. S. Vemaganti and J. T. Oden. Estimation of local modeling error and goal-oriented adaptive modeling of heterogeneous materials: Part II: a computational environment for adaptive modeling of heterogeneous elastic solids. *Computer Methods in Applied Mechanics and Engineering*, 190(46):6089–6124, 2001. (cited in page(s) 6)

[198] F. Verdugo and P. Díez. Computable bounds of functional outputs in linear visco-elastodynamics. *Computer Methods in Applied Mechanics and Engineering*, 245-246:313–330, 2012. (cited in page(s) 6)

[199] R. Verfürth. Robust A Posteriori Error Estimates for Stationary Convection-Diffusion Equations. *SIAM Journal on Numerical Analysis*, 43(4):1766–1782, 2005. (cited in page(s) 39)

[200] J. Waeytens, L. Chamoin, and P. Ladevèze. Guaranteed error bounds on pointwise quantities of interest for transient viscodynamics problems. *Computational Mechanics*, 49(3):291–307, 2012. (cited in page(s) 6)

[201] K. Wu and D. Xiu. Data-driven deep learning of partial differential equations in modal space. *Journal of Computational Physics*, 408:109307, 2020. (cited in page(s) 57)

[202] H. Xu, C. D. Cantwell, C. Monteserin, C. Eskilsson, A. P. Engsig-Karup, and S. J. Sherwin. Spectral/*hp* element methods: Recent developments, applications, and perspectives. *Journal of Hydrodynamics*, 30(1):1–22, 2018. (cited in page(s) 3)

[203] F. Yaman, V. G. Yakhno, and R. Potthast. Recent Theory and Applications on Inverse Problems. *Mathematical Problems in Engineering*, 2013:303154, 2013. (cited in page(s) 57)

[204] H. Yserentant. On the multi-level splitting of finite element spaces. *Numerische Mathematik*, 49(4):379–412, 1986. (cited in page(s) 3)

[205] S. Yu and J. Ma. Deep Learning for Geophysics: Current and Future Trends. *Reviews of Geophysics*, 59(3):e2021RG000742, 2021. e2021RG000742 2021RG000742. (cited in page(s) 57)

[206] Y. Yu, R. M. Kirby, and G. E. Karniadakis. *Spectral Element and hp Methods*, pages 1–43. John Wiley & Sons, Ltd, 2017. (cited in page(s) 3)

[207] N. Zander, T. Bog, M. Elhaddad, F. Frischmann, S. Kollmannsberger, and E. Rank. The multi-level *hp*-method for three-dimensional problems: Dynamically changing high-order mesh refinement with arbitrary hanging nodes. *Computer Methods in Applied Mechanics and Engineering*, 310:252–277, 2016. (cited in page(s) 4, 8, 20)

[208] N. Zander, T. Bog, S. Kollmannsberger, D. Schillinger, and E. Rank. Multi-level *hp*-adaptivity: high-order mesh adaptivity without the difficulties of constraining hanging nodes. *Computational Mechanics*, 5:499–517, 2015. (cited in page(s) 4, 8, 11, 20)

[209] N. Zander, H. Bériot, C. Hoff, P. Kodl, and L. Demkowicz. Anisotropic multi-level *hp*-refinement for quadrilateral and triangular meshes. *Finite Elements in Analysis and Design*, 203:103700, 2022. (cited in page(s) 8, 12)

[210] N. D. Zander. *Multi-level hp-FEM: dynamically changing high-order mesh refinement with arbitrary hanging nodes*. Dissertation, Technische Universität München, München, 2017. (cited in page(s) 4, 8, 11, 12, 20)

[211] O. C. Zienkiewicz and R. L. Taylor. *The Finite Element Method for Solid and Structural Mechanics*. Elsevier, 2005. (cited in page(s) 1)

[212] O. C. Zienkiewicz, R. L. Taylor, and D. D. Fox. *The Finite Element Method: Volume 1 - Basic Formulations and Linear Problems*. Butterworth-Heinemann, 2000. (cited in page(s) 1)

[213] O. C. Zienkiewicz, R. L. Taylor, and J. Z. Zhu. *The Finite Element Method: Volume 2 - Solid Mechanics*. Butterworth-Heinemann, 2000. (cited in page(s) 1)

[214] O. C. Zienkiewicz, R. L. Taylor, and J. Z. Zhu. *The Finite Element Method: Volume 3 - Fluid Dynamics*. Butterworth-Heinemann, 2000. (cited in page(s) 1)

[215] G. W. Zumbusch. *Simultaneous h-p Adaptation in Multilevel Finite Elements*. PhD thesis, Konrad–Zuse–Zentrum für Informationstechnik Berlin (ZIB), Heilbronner Str. 10, D–10711 Berlin–Wilmersdorf, Germany, 1995. (cited in page(s) 3)